UCTEA Turkish Chamber of Civil Engineers
TMMOB İnşaat Mühendisleri Odası

Turkish Journal of Civil Engineering

formerly
Teknik Dergi

Volume 34
Issue 6
November 2023

Turkish Journal of Civil Engineering (formerly Teknik Dergi) Publication Principles

Turkish Journal of Civil Engineering (TJCE), a non-profit, open access scientific and technical periodical of UCTEA Chamber of Civil Engineers, publishes papers reporting original research work and major projects of interest in the area of civil engineering. TJCE annually publishes six issues and is open to papers in English and Turkish. It should be noted that TJCE (formerly, Teknik Dergi/ Technical Journal of Turkish Chamber of Civil Engineers) is being published regularly for more than 30 years since 1990. Main publication principles of TJCE are summarized below:

1. Articles reporting original scientific research and those reflecting interesting engineering applications are accepted for publication. To be classified as original, the work should either produce new scientific knowledge or add a genuinely new dimension to the existing knowledge or develop a totally new method or substantially improve an existing method.
2. Articles reporting preliminary results of scientific studies and those which do not qualify as full articles but provide useful information for the reader can be considered for publication as technical notes.
3. Discussions received from the readers of the published articles within three months from publication are reviewed by the Editorial Board and then published together with the closing remarks of the author.
4. Manuscripts submitted for publication are evaluated by two or three reviewers unknown to the authors. In the light of their reports, final decision to accept or decline is taken by the Editorial Board. General policy of the Board is to get the insufficient manuscripts improved in line with the reviewers' proposals. Articles that fail to reach the desired level are declined. Reasons behind decisions are not declared.
5. A signed statement is taken from the authors, declaring that the article has not been published as a "journal article or book chapter". In case the Editorial Board is in the opinion that the article has already been published elsewhere with minor changes or suspects plagiarism or a similar violation of ethics, then not only that article, but none of the articles of the same authors are published.
6. Papers reporting works presented as conference papers and developed further may be considered for publication. The conference it was presented to is given as a footnote in the first page.
7. Additionally, a document signed by all authors, transferring the copyright to UCTEA Chamber of Civil Engineers is submitted together with the manuscript.

UCTEA Turkish Chamber of Civil Engineers
TMMOB İnşaat Mühendisleri Odası

Turkish Journal of Civil Engineering

(formerly Teknik Dergi)

Volume 34 Issue 6 November 2023

UCTEA Turkish Chamber of Civil Engineers
TMMOB İnşaat Mühendisleri Odası
Necatibey St. No: 57, Kızılay 06440 Ankara, Turkey
Tel: +90.312.294 30 00 - Faks: +90.312.294 30 88
E-mail: imo@imo.org.tr - www.imo.org.tr

Publisher *(Sahibi)*:
Taner YÜZGEÇ
On behalf of UCTEA Turkish Chamber of Civil Engineers

Administrative Officer *(Yazı İşleri Müdürü)*:
Özer AKKUŞ

Volume 34 - Issue 6 - November 2023 *(Cilt 34 - Sayı 6 - Kasım 2023)*
Published bi-monthly. Local periodical. *(İki ayda bir yayınlanır, yerel süreli yayın)*
Date of Print: November 1, 2023 *(Baskı Tarihi: 1 Kasım 2023)*
Number of copies: 800 *(800 adet basılmıştır)*

ISSN: 2822-6836

Turkish Journal of Civil Engineering (formerly Teknik Dergi) is indexed by

- Science Citation Index Expanded
- Scopus
- Journal Citation Reports / Science Edition
- Engineering Index
- Concrete Abstracts (American Concrete Institute)
- National Technical Information Service (US NTIS)
- CITIS
- Ulrich's International Periodical's Directory
- Google Scholar
- TR Index

Turkish Journal of Civil Engineering (formerly Teknik Dergi) is a peer reviewed open access periodical publishing papers of original research and interesting practice cases. It addresses both the research community and the practicing engineers.

Printed by *(Baskı)*:
Ziraat Gurup Matbaacılık Ambalaj San. Tic. A.Ş.
Bahçekapı Mah. 2534 Sok. No: 18 Şaşmaz, Etimesgut / Ankara
Tel: 0.312.384 73 44 - Faks: 0.312.384 73 46

Reviewers:

This list is renewed each year and includes reviewers who served in the last two years of publication.

Şükran AÇIKEL
Merve AÇIKGENÇ ULAŞ
Perviz AHMEDZADE
Bülent AKBAŞ
Şeref Doğuşcan AKBAŞ
Rıfat AKBIYIKLI
Özge AKBOĞA KALE
Sarven AKCELYAN
Burcu AKÇAY ALDANMAZ
Cihan Taylan AKDAĞ
Cem AKGÜNER
Çağlar AKKAYA
Fevziye AKÖZ
Erkan AKPINAR
Muhammet Vefa AKPINAR
Atakan AKSOY
Hafzullah AKSOY
Tülay AKSU ÖZKUL
Uğurhan AKYÜZ
Sadık ALASHAN
Cenk ALHAN
Ayşe Burcu ALTAN SAKARYA
Sinan ALTIN
Adlen ALTUNBAŞ
Ahmet Can ALTUNIŞIK
Yalçın ALVER
Bahadır ALYAVUZ
Özgür ANIL
Necati ARAS
Davit ARDİTİ
Yalın ARICI
Deniz ARTAN İLTER
Ali Osman ATAHAN
Hakan Nuri ATAHAN
Ali Osman ATEŞ
Bekir Özer AY
Gökçe AYDIN
Metin AYDOĞDU
Hakan AYGÖREN
Mustafa Tamer AYVAZ
Ülker Güner BACANLI
İhsan Engin BAL
Selim BARADAN
Eray BARAN
Özgür Uğraş BARAN
Türkay BARAN
Bekir Oğuz BARTIN
Mustafa Gökçe BAYDOĞAN
Cüneyt BAYKAL
Niyazi Özgür BEZGİN
Senem BİLİR MAHÇİÇEK
Gökçen BOMBAR
Burak BOYACI
İlknur BOZBEY
Ali BOZER
Zafer BOZKUŞ
Erdem CANBAY
Zekai CELEP
Cihan CENGİZ
Halim CEYLAN
Hüseyin CEYLAN
Ömer CİVALEK
Joao Ramoa CORREIA
Ayşe COŞKUN BEYAN
Ali Fırat ÇABALAR
Barlas Özden ÇAĞLAYAN
Melih ÇALAMAK
Gülben ÇALIŞ
Umut ÇALIŞKAN
Süheyla Pelin ÇALIŞKANELLİ
Mehmet Alper ÇANKAYA
Dilay ÇELEBİ
Tevfik Kutay ÇELEBİOĞLU
Ahmet Ozan ÇELİK
Oğuz Cem ÇELİK
Semet ÇELİK
Hilmi Berk ÇELİKOĞLU
Kemal Önder ÇETİN
Mahmut ÇETİN
Mecit ÇETİN
Erdal ÇOKÇA
Semra ÇOMU
İsmail DABANLI
Ömer DABANLI
Atilla DAMCI
Yakup DARAMA
Osama M.F. DAWOUD
Tayfun DEDE
Abdullah DEMİR
Cem DEMİR
Emre DEMİR
Uğur DEMİR (İTÜ)
Uğur DEMİR (İYTE)
Munise Didem DEMİRBAŞ
Ender DEMİREL
Mehmet Cüneyd DEMİREL
Seyyit Ümit DİKMEN
Ali Ersin DİNÇER
İsmail DURANYILDIZ
Selim DÜNDAR
Nurhan ECEMİŞ ZEREN
Volkan Ş. EDİGER
Özgür EKİNCİOĞLU
Murat Altuğ ERBERİK
Ali ERCAN
Sinan Turhan ERDOĞAN
Şakir ERDOĞDU
Ramazan Cüneyt ERENOĞLU
Esin ERGEN PEHLEVAN
Gökmen ERGÜN
Bülent ERKMEN
Barış ERKUŞ
Yusuf Çağtay ERŞAN
Kağan ERYÜRÜK
Tuğba ESKİŞAR TEFÇİ
Burak FELEKOĞLU
Mahmut FIRAT
Okan FISTIKOĞLU
Onur GEDİK
Abdullah GEDİKLİ
Ahmet Talha GEZGİN
Sadık Can GİRGİN
Zehra Canan GİRGİN
Ilgın GÖKAŞAR
Serdar GÖKTEPE
Rahmi GÜÇLÜ
Ali GÜL
Fazlı Erol GÜLER
Ilgın GÜLER
Hamza GÜLLÜ
Gürkan GÜNAY
Taylan GÜNAY
Murat GÜNAYDIN
Samet GÜNER
Oğuz GÜNEŞ
Mehmet Şükrü GÜNEY
Tuba GÜRBÜZ BÜYÜKKAYIKÇI
Aslı Pelin GÜRGÜN
Soner HALDENBİLEN
Murat HAMDERİ
Ingo A. HANSEN
Umut HASGÜL
Bo-Tao HUANG
Zeynep IŞIK
Sabriye Banu İKİZLER
Erol İSKENDER
Medine İSPİR ARSLAN
Recep İYİSAN
Nihat KABAY
Mehmet Sedat KABDAŞLI
Mehmet Rifat KAHYAOĞLU
Özkan KALE
Volkan KALPAKÇI
Elif Çağda KANDEMİR
Tanay KARADEMİR
Hüseyin Faruk KARADOĞAN
Ümit KARADOĞAN
Mustafa Erkan KARAGÜLER
Halil KARAHAN
Zülküf KAYA
Oğuz KAYABAŞI
Hasan Ahmed KAZMEE
Mustafa Kubilay KELEŞOĞLU
Elçin KENTEL
Hadi KHANBABAZADEH
Havvanur KILIÇ
Ufuk KIRBAŞ
Veysel Şadan Özgür KIRCA
Cem KIRLANGIÇOĞLU
Güven KIYMAZ
Gökhan KİRKİL
Esat Selim KOCAMAN
Kasım KOÇAK
Salih KOÇAK
Niyazi Uğur KOÇKAL
Baha Vural KÖK
Mete KÖKEN
Hasan KURTARAN
Murat KURUOĞLU
Akif KUTLU
Abdullah KÜRKÇÜ
Hilmi LUŞ
Kasım MERMERTAŞ
Mahmoud MIARI
Yetiş Şazi MURAT
Öcal NECMİOĞLU
Fuad OKAY
Umut OKKAN
Derviş Volkan OKUR
Mehmet Hakkı OMURTAG
Sezan ORAK
Engin ORAKDÖĞEN
Akın ÖNALP
Bihrat ÖNÖZ
Ali Hakan ÖREN
Ceyhun ÖZÇELİK
Yiğit ÖZÇELİK
Gökhan ÖZDEMİR
Murat ÖZEN
Pelin ÖZENER
Hasan ÖZER
Hakkı Oral ÖZHAN
Mehmet Fatih ÖZKAL
Zeynep Huri ÖZKUL BİRGÖREN
Ahmet ÖZTOPAL
Sadık ÖZTOPRAK
Turan ÖZTURAN
Mustafa ÖZUYSAL
Tolga Yılmaz ÖZÜDOĞRU
Atilla ÖZÜTOK
Nilüfer ÖZYURT ZİHNİOĞLU
Ahmet Onur PEHLİVAN
Seval PINARBAŞI ÇUHADAROĞLU
Elişan Filiz PİROĞLU
Selman SAĞLAM
Mehmet SALTAN
Metin SARIGÖL
Altuğ SAYGILI
Serdar SELAMET
Osman SİVRİKAYA
Behzad SOLTANBEIGI
Serdar SOYÖZ
Rifat SÖNMEZ
Tayfun Altuğ SÖYLEV
Erol ŞADOĞLU
Olcay ŞAHİN
Yuşa ŞAHİN
Zekai ŞEN
Burak ŞENGÖZ
Karin ŞEŞETYAN
Ali Ünal ŞORMAN
Gülüm TANIRCAN
Serhan TANYEL
Kerem TAŞTAN
Gökmen TAYFUR
Rasim TEMÜR
Serdal TERZİ
Berrak TEYMUR
Hüseyin Onur TEZCAN
Mesut TIĞDEMİR
Salih TİLEYLİOĞLU
Vedat TOĞAN
Onur Behzat TOKDEMİR
İrem Dikmen Toker TOKER
Ali TOPAL
Cem TOPKAYA
Kamile TOSUN FELEKOĞLU
Erkan TÖRE
Ülgen Mert TUĞSAL
Gürsoy TURAN
Ö. Tuğrul TURAN
Cüneyt TÜZÜN
Eren UÇKAN
Latif Onur UĞUR
Ergin ULUTAŞ
Dilay UNCU
Tayfun UYGUNOĞLU
Volkan Emre UZ
İbrahim Mert UZUN
Deniz ÜLGEN
Mehmet Barış Can ÜLKER
Yurdanur ÜNAL
Cüneyt VATANSEVER
Syed Tanvir WASTI
Ahmet YAKUT
Erkut YALÇIN
Mehmet Cem YALÇIN
Aslı YALÇIN DAYIOĞLU
Mustafa Sinan YARDIM
Mert Yücel YARDIMCI
Anıl YAZICI
Gökhan YAZICI
Halit YAZICI
Mehmet YETMEZ
Tahsin Alper YIKICI
İrem Zeynep YILDIRIM
Mehmet YILDIRIMOĞLU
Abdülazim YILDIZ
Mustafa Tolga YILMAZ
Berivan YILMAZER POLAT
İsmail YÜCEL
Yeliz YÜKSELEN AKSOY
Shaban Isamel Albrka Ali ZANGENA
Abdullah Can ZÜLFİKAR

Turkish Journal of Civil Engineering (formerly Teknik Dergi)

Volume 34 Issue 6 November 2023

CONTENTS

Turkish Journal of Civil Engineering, 2023, 1-28, Paper 749, ***Research Article***

Hazard Curves for Reliability Assessment of Strip Footings on Spatially Varying Cohesive Soils

Ahmet Can MERT[1*]
Gökhan YAZICI[2]
Hadi KHANBABAZADEH[3]

ABSTRACT

The present study aimed to create a series of hazard curves against maximum total settlement and angular rotation of strip footings for probabilistic shallow foundation design on clays. Random field finite element method (RFEM) was adopted with elasto-plastic clay-like soil behavior, deformation modulus (E_d) and shear strength parameters (c and ϕ) were employed as random field inputs. Parameters were defined and assigned to the analysis models with varying correlation lengths (θ_h, θ_v). Models have been iteratively solved one thousand times, and output distributions of maximum settlement and angular rotations were recorded. Probability density functions (PDF) were fitted to the outputs, and probability of failure (P_f) for footing deformation limits was subsequently estimated. Proposed hazard curves for two anisotropy and three variability categories were developed employing the estimated P_fs. The method proposed has been validated using an independent database of in-situ results, and a worked example was provided to illustrate the implementation of the process. The key contribution of the research is to form hazard curves for shallow foundations considering elasto-plastic soil behavior with the impact of all influencing parameters, respecting the limit values for foundation deformation in the design codes. The proposed technique offers a probabilistic evaluation of strip footings with spatial variation of clayey soils and a valid method for the reliability-based design of foundations in the serviceability limit state.

Keywords: Random field finite element method, strip footings, soil-foundation-structure interaction, reliability-based design, serviceability limit state, cohesive soils.

Note:
- This paper was received on November 14, 2022 and accepted for publication by the Editorial Board on August 4, 2023.
- Discussions on this paper will be accepted by January 31, 2024.
- https://doi.org/10.18400/tjce.1340360

1 Bahcehesir University, Department of Civil Engineering, Istanbul, Türkiye
ahmetcan.mert@bau.edu.tr - https://orcid.org/0000-0002-2483-1330

2 Istanbul University Cerrahpasa, Department of Civil Engineering, Istanbul, Türkiye
gokhan.yazici@iuc.edu.tr - https://orcid.org/0000-0002-6719-9152

3 Gebze Technical University, Department of Civil Engineering, Kocaeli, Türkiye
hk.babazadeh@gtu.edu.tr - https://orcid.org/0000-0001-9764-7799

* Corresponding author

1. INTRODUCTION

Strip footings are simple yet effective superficial foundation systems, making them one of the initial alternatives to the design process. In most cases, strip footings fail by exceeding the serviceability limits (SLS) before reaching the ultimate limit state (ULS). Accordingly, the SLS governs the design rather than ULS in practice. Hence, many design regulations recommend deformation limits for footing design by SLS. For example, Eurocode 7 suggests a 25 mm maximum settlement for the serviceability limit of strip footings [1]. Regardless of the limit state considered, the primary factor for a sound foundation design is the determination of the soil parameters which accurately represent the site conditions. Any geotechnical solution may have three sources of uncertainties within this context: inherent soil variability, measurement error, and transformation uncertainty [2,3]. Measurement error and transformation uncertainty can be minimized by increasing the number of samples and using highly correlated equations. The inherent soil variability, the principal source of uncertainty, must be considered through probabilistic methods. Suitably, engineering codes such as Eurocode and ISO (International Organization for Standardization) accept the Reliability-Based Design (RBD) approach, representing the geotechnical parameter variation as a random variable fitting a probability distribution [4,5]. Reliability index (β) is the primary measure for RBD, and the design regulations recommend a target value β to achieve a reliable foundation design.

One of the practical tools to express the soil spatial variability is random field (RF) theory, which seeks to model complex patterns of variation and interdependence in cases where deterministic treatment is inefficient and conventional statistics are insufficient [6,7]. The first geotechnical application combined the random field theory with the finite element method on a footing settlement analysis using Taylor series expansion, entitled the stochastic finite element method (SFEM)[8]. Since the series expansion requires complex mathematical solutions, a practical alternative named the random field finite element method (RFEM) was developed, which preserves the probability distribution of deformation by iteratively solving random field realizations. The study conducted by Griffiths and Fenton in 2009 revealed that RFEM provides more reliable results than SFEM, especially in higher-order spatial variation [9]. RFEM can be applied to most shallow foundation problems, including the analysis of maximum settlement of strip footing [10–12], differential settlement of two strip footings in plain strain condition [13,14], maximum and differential settlement analysis of spread footings by RFEM in 3D [11,14]. There were further investigations on shallow foundation analysis by RFEM with eccentric and inclined loading cases [15,16]. These studies disclosed the need for soil uncertainty for foundation design, as soil spatial variability substantially affects failure modes and bearing capacity of shallow foundations [17,18]. From this point of view, the design of strip footings by deterministic methods leads to an over- or under-design compared to the RBD of footings. Thus, all related previous studies emphasized the significance of soil spatial variability.

Recent studies investigated the deformations of shallow foundations on elastic soil [19–22]. These works well represented the soil spatial variability, albeit the actual stress-strain behavior of soil can be overlooked due to the elastic conditions. The research on the nonlinear behavior of soil utilized Mohr-Coulomb (MC) failure criterion with Young's Modulus (E) random field for deformation analysis of single strip footing [10,23] and differential settlement analysis of two neighboring strip footings [13]. However, the studies solved the

problem with a single random variable. Another study considered the nonlinear soil behavior by MC failure criterion and employed Poisson's ratio ν as a random field in addition to Young's Modulus E [15]. A study by the first author performed RFEM in a 2D strip footing problem with CPT-based RF of soil deformation modulus (E_d), considering MC failure criterion [24]. Regardless of the number of parameters employed, footing deformation researches used rigidity and excluded the shear strength parameters. On the other hand, the undrained shear strength parameter was deemed in the bearing capacity investigations for shallow foundations on clay, and the deformation behavior was excluded [25–27]. The current investigation defines soil strength and stiffness parameters as random fields for the reliability evaluation of strip footings on clay utilizing RFEM. The finite element analysis in the study considered the elasto-plastic clay-like soil behavior, deformation modulus and shear strength parameters (c and ϕ) were employed as random field inputs. The present work aims to create a sequence of hazard curves against maximum settlement and angular rotation for probabilistic shallow foundation design on clays. The current literature contains a related study on hazard curves for bearing capacity with the Tresca failure criterion [28]. However, the study covered ULS solution with a single shear strength parameter, and there was no previous study on hazard curves against footing deformations. The key contribution of the latter study is to develop a design framework for the reliability assessment of shallow foundations on spatially varying clay obeying the deformation limits in design codes. The proposed procedure will offer a valid method for RBD footings with SLS and probabilistic evaluation of strip footings taking soil spatial variability into account.

2. RANDOM FIELD FINITE ELEMENT METHOD (RFEM)

The controlling parameters of strip footing deformations on cohesive soils are the deformation modulus of soil E_d and the shear strength parameters c and ϕ. Defining these random field inputs is the initial step in developing the method. Once the random variable fits a probability distribution, the field is then determined by the correlation function, which depends on the variation distance of the random parameter in the field called correlation length θ. Markov correlation function in Eq.1 was adopted for 2D Gaussian random field case [7]:

$$\rho(\tau) = \exp\left(-\frac{|\tau|}{\theta_h} - \frac{|\tau|}{\theta_v}\right) \quad (1)$$

where τ is the distance between two random variables in the field, θ_h and θ_v are the horizontal and vertical correlation lengths, respectively.

2.1. Random Field Discretization and Meshing

The discretization of RF facilitated the assignment of a random variable in a random field mesh element. The continuous Gaussian random field function $f(\mathbf{x})$ became a set of $\hat{f}(x) = \{f_i\}$ by discretization. Non-Gaussian random variables were transformed into an equivalent Gaussian field since the discretization of the field employed linear transformation, which remained Gaussian after the process. In the latter research, the series expansion technique (SE) was employed for the random field discretization. The early studies on SE method

discretized the random field by spectral decomposition of Karhunen-Loeve (KL) series expansion [29,30]. The random field is represented as infinite series with standard normal variate ζ_i, eigenvalues λ_i, and eigenfunctions $g_i(\mathbf{x})$ of the correlation structure given in Eq.2:

$$f(\mathbf{x}) = \mu(\mathbf{x}) + \sigma \sum_{i=1}^{\infty} \xi_i \sqrt{\lambda_i} g_i(\mathbf{x}) \tag{2}$$

The eigenvalue problem is calculated using the integral solution of Eq.3:

$$\int_{\Omega} \rho(\mathbf{x},\mathbf{x}') g_i(\mathbf{x}') d\mathbf{x}' = \lambda_i g_i(\mathbf{x}) \tag{3}$$

In this way, a finite random variable of ζ_i represents the random field, and the discretized form of the field function with the r term is given in Eq.4. The truncation is applied with minor errors once the decay of the eigenvalues of expansion is described [31]. The truncation error was negligible since the terms having the highest eigenvalue were used.

$$\hat{f}(\mathbf{x}) = \mu(\mathbf{x}) + \sigma(\mathbf{x}) \sum_{i=1}^{r} \xi_i \sqrt{\lambda_i} g_i(\mathbf{x}) \tag{4}$$

There were developments in the approximation to the integral solution of the eigenvalue problem instead of directly solving Eq.3. One of the studies transformed the integral problem into a matrix eigenvalue problem by discrete integration rule [32]. Other approaches for the solution of Eq.3, such as Galerkin-type approximation [33] and wavelet-Galerkin scheme [34]. The present study discretized the random field by KL series expansion, and the eigenvalue problem was solved in MATLAB by transforming Eq.3 into a matrix form.

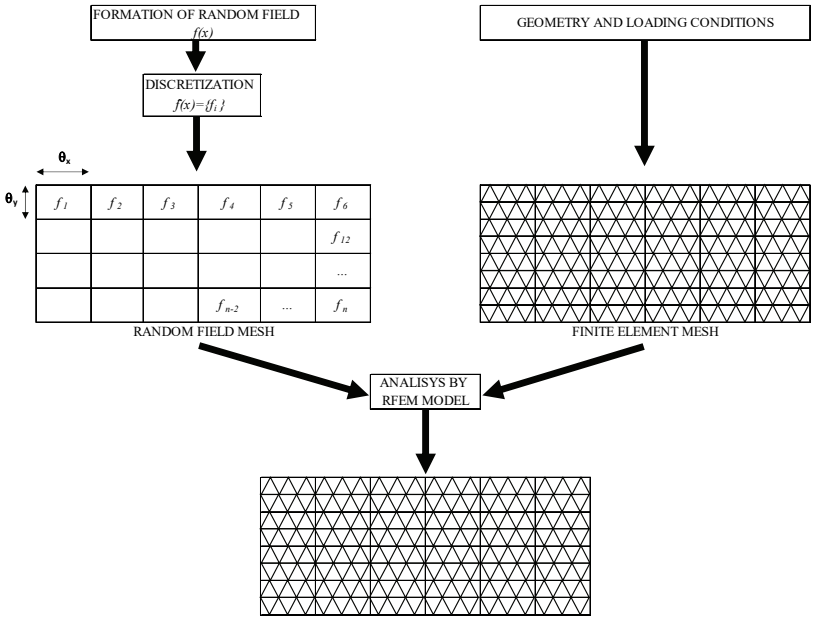

Fig. 1 - RFEM Meshing steps

Two separate meshes were recommended in the random field-based FEM analyses [35]. Theoretically, FEM and random field meshes are independent since their size selection criteria differ. FEM mesh size is selected by considering the model loading conditions and geometry. However, the random field mesh depends on the correlation length of the random parameter, and the random field mesh is more significant than the FEM mesh in RFEM. Fig. 1 illustrates the use of two meshes in RFEM solutions.

The current investigation followed the practical rule found in the literature. The random field mesh sizes are coarser than the FEM mesh sizes after the geometry, loading, and correlation length conditions are fulfilled [36]. The ratio of the random field mesh sizes to the varying correlation lengths was set to 1.

3. RFEM MODELLING OF SHALLOW STRIP FOOTING

The probabilistic results of the RFEM model for strip footing subjected to a vertical line load were investigated. The line load was determined as P=250kN/m, corresponding to the SLS characteristic settlement limit of 25 mm. Analyses were performed in finite element software ANSYS 2021 R2, and all the formulations of FEM and material models were taken from the theory reference of the code [37]. The overall equilibrium for the elastic static structural analysis is as follows:

$$[\mathrm{K}]\{u\} = \{F\} \tag{5}$$

where [K] is the total stiffness matrix (which is the sum of element stiffness matrices [K_e] over the N number of finite elements), {u} is the nodal displacement vector, and {F} is the load vector in Eq.5. The random field of (E_d) generated the probabilistic [K] matrix, which consists of the field realizations. The total stiffness matrix was then re-defined in the form of Eq.6 since the random field was defined by KL series expansion with r term and mean values of stiffness matrix [K_0]:

$$[K] = [K_0] + \sum_{i=1}^{r} [K_i]\xi_i \tag{6}$$

In that way, a probabilistic displacement vector {u} was obtained in RFEM. The influence of cohesive soil behavior was considered (models entitled CLAY henceforth), and the linear elastic-perfectly plastic Mohr-Coulomb model was employed so that c and ϕ constitute the yield surface. Since the shear strength parameters were random fields in the latter study, the stress vector {σ} in the fundamental stress-strain equation (Eq.7) also became probabilistic:

$$\{\sigma\} = [\mathrm{D}]\{\varepsilon^{el}\} = [D]\{\varepsilon - \varepsilon^{pl}\} \tag{7}$$

where [D] is the elasticity matrix, ε, ε^{el} and ε^{pl} are total, elastic, and plastic strain vectors, respectively. A representative model is demonstrated in Fig. 2; the drained condition of the soil was considered, and the groundwater level was assumed to be below the investigation depth of the soil layer. Soil and footing bodies were modeled using a 3D 10-Node tetrahedral structural solid (SOLID187). Concrete material properties were assigned to the footing solid.

Contact surfaces were defined between the footing and soil bodies: 3D 8-node surface-to-surface contact element (CONTA174) was associated with a 3D target segment (TARGE170) using shared geometric characteristics as the underlying element. The software allows the stiffness variation at the contact point as if there were springs with different stiffness values than the contact body stiffness at these points. The input of stiffness ratio is called FKN in the code, and the value of 0.67 was adopted by remaining within the typical interval of rigidity and strength ratio for soil-structure contacts [38].

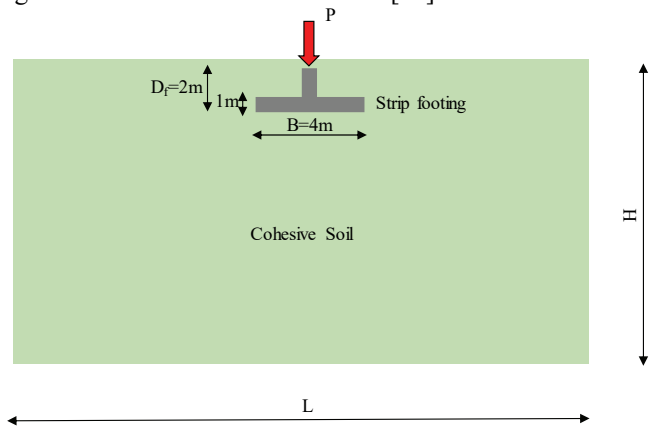

Fig. 2 - RFEM model of strip footing

3.1. Dimensions and Boundary Conditions

Dimensions of the soil body were formed so that the deformation contours were not affected by the boundaries (Fig. 3). RFEM model was created using 3D solid elements with 1-meter thickness, and the boundary restraints provided the plane strain conditions. The model base was fixed, deformations in the x and z axes were constrained on the sides, and the z-axis was constrained on the front and back. Model limits (H and L), dimensions of strip footing (B, t, D_f), loads (P), and physical properties of soil are kept deterministic. Poisson's ratio (ν) of

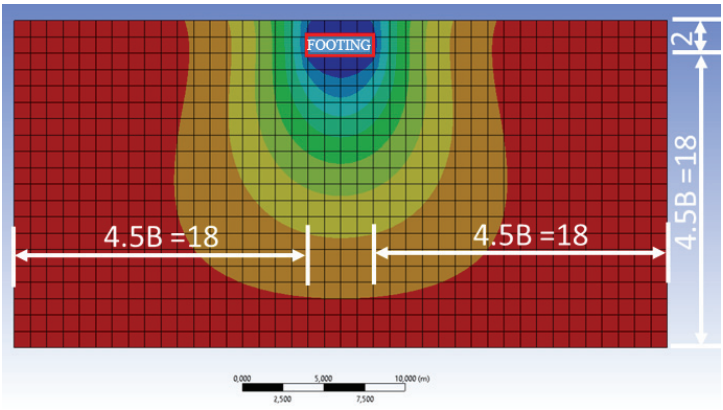

Fig. 3 - RFEM Model dimensions

soil was constant as a typical value of 0.35 for cohesive soils since the influence of ν variation in RFEM can be negligible [39].

3.2. Random Variables and Deformation Limits

Mean values of spatially varying inputs were selected as typical values in the literature [38,40]. The values are presented in three variability categories according to the coefficient of variations (COV): LOW, MID, and HIGH (Table 1).

Table 1 - Random variables in the model

Mean Values (μ)			
μ_E=15 MPa	**$\mu_{c'}$=5 kPa**	**$\mu_{\phi'}$=20°**	**Variability**
COV=0.60 (2-83 MPa)	COV=0.30 (2-13 kPa)	COV=0.10 (14-28°)	LOW
COV=0.70 (2-103 MPa)	COV=0.40 (1-17 kPa)	COV=0.15 (12-33°)	MID
COV=0.80 (1-126 MPa)	COV=0.50 (1-22 kPa)	COV=0.20 (10-38°)	HIGH

All the parameter limits remained within the ranges suggested in practice. Correlation lengths are given dimensionless ratio (Θ_h) in the horizontal direction in terms of B and the vertical-to-horizontal ratio in the vertical direction. The accepted values are given in Table 2, and the correlation length intervals remained within the limits recommended in the literature [41,42].

Table 2 - Correlation lengths in the analyses

Parameter	**Value**
$\Theta_h=\theta_h$ / B	0.25 0.50 1.00 2.50 5.00 10.00 (θ_h=1-40m)
θ_h / θ_v	2.00 10.00 (θ_v=0.1-20.0m)

Proposed hazard curves for maximum settlement and angular rotation of strip footing have been established according to the characteristic hazard limits found in the literature [43,44]: Safe Limit, Minor Damage, Medium Damage, and Major Damage (Table 3).

Table 3 - Deformation limits for hazard curves

Criteria		**Limit**
Total Max. Settlement (mm)	Safe Limit	25
	Medium Damage	35
	Major Damage	50
Angular Rotation (δ/B)	Minor Damage	1/1000
	Safe Limit	1/500
	Major Damage	1/250

3.3. Generation of RF Inputs

RF soil parameters were defined using an open-source MATLAB function called "randomfield" [45]. The function generates Gaussian random field realizations, given the RF mesh and correlation structure. RF inputs were assumed to fit a log-normal distribution to eliminate the negative values in the realizations. Mean (μ) and standard deviation (σ) were transformed into equivalent normal distribution forms to define Gaussian RF:

$$\sigma_{\ln} = \sqrt{\ln(1 + COV^2)} \qquad \mu_{\ln} = \ln(\mu) - 0.5\sigma_{\ln}^2 \tag{8}$$

RFEM models were constructed with the correlation lengths given in Table 2, and equivalent normal distribution parameters of each model were calculated using Eq.8 with the mean values and COVs. An exemplary process of RF realizations of the CLAY1 model for LOW variability has been elucidated. Standard Gaussian RF with μ=0 and σ=1 (g_i) was initially generated with the geometry and correlation info, and g_i was subsequently transformed into F_i field utilizing Eq.9:

$$F_i = \exp(\mu_{\ln} + \sigma_{\ln}.g_i) \tag{9}$$

Realizations of the E_d field were calculated as follows: $F_i = \exp(2.5543 + 0.5545.g_i)$. The process was iterated for RFs of shear strength inputs c and ϕ such that each RFEM model contained nine random fields for three main inputs and three variability categories. Representative realizations of each parameter for CLAY1 model LOW variability were given in Fig. 4. The parameter fluctuations along depth and in the horizontal direction depicted the intrinsic soil uncertainty owing to geological conditions such as stratification, faulting, soil deposition, over-consolidation, or desiccation.

3.4. Analysis Framework

The RFEM analysis algorithm in the study started by generating RFs for soil stiffness and shear strength parameters using MATLAB. The function automatically discretized RFs by the KL series expansion method. CLAY models were established in FEM software, and the soil body was divided into tiny rectangular prisms according to the values of θ_h and θ_v. Each value in the RF realizations of the inputs was assigned to the center of the corresponding random field mesh elements. The overall model geometry is listed in Fig. 5. Each model contained c ϕ and E_d RFs simultaneously, and RFEM models were set to analyze one thousand iterations involving all realizations with three variability categories. Thus, each model performed three thousand iterations for all variabilities. The histograms of footing deformations were attained, whereupon the analyses and appropriate probability density functions (PDF) were fitted to the output distributions. PDFs were utilized to estimate the P_fs for the deformation limits. The values of P_f, θ_h and θ_v constructed the proposed hazard curves, and each hazard curve comprised three damage limits for RBD of a shallow foundation according to multiple damage limits. The main framework of the investigation explained is illustrated in Fig. 6.

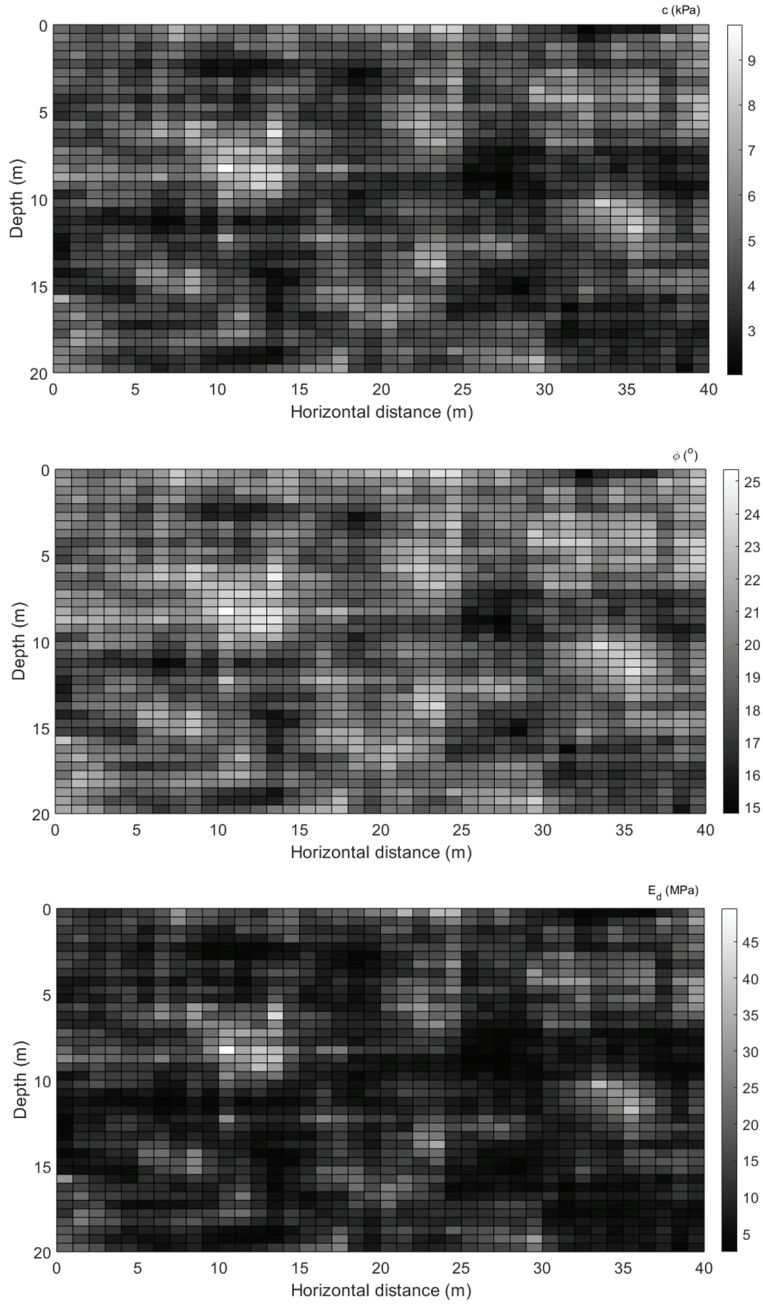

Fig. 4 - Representative realizations of c, ϕ, E_d RFs for CLAY1 model LOW variability category

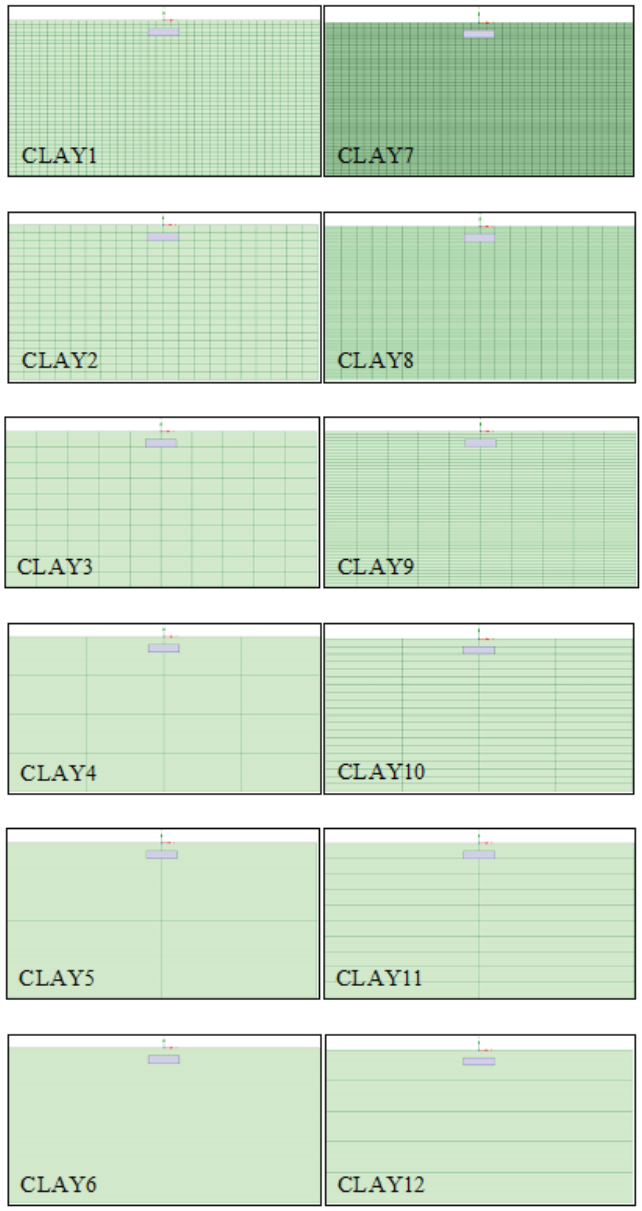

Fig. 5 - RFEM models in ANSYS

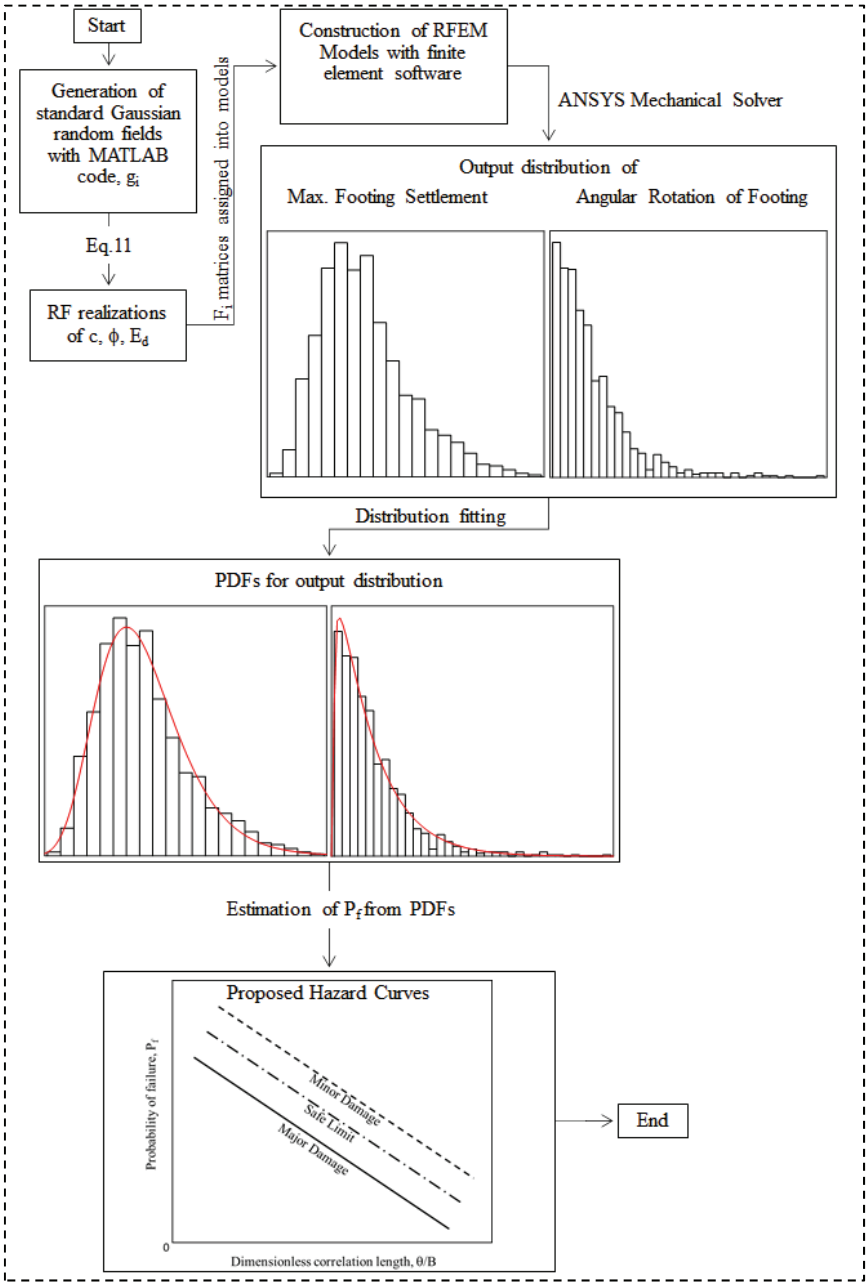

Fig. 6 - Main algorithm for the development of the proposed hazard curves

4. RESULTS

Vertical nodal displacements on the left and right edges of the footing (u_{left}, u_{rigth}) were recorded. The absolute maximum of these nodal displacements represented the total settlement (s_{max}), and the absolute difference between them represented the angular rotation ($\tan\alpha$) depicted in Fig. 7.

Each model performed the iterations, and six output distributions were obtained for all variability categories (three for total settlement and three for angular rotation). Log-normal PDF fitted the total settlement outputs (Fig. 8a), and Gamma distribution fitted the angular rotation results (Fig. 8b).

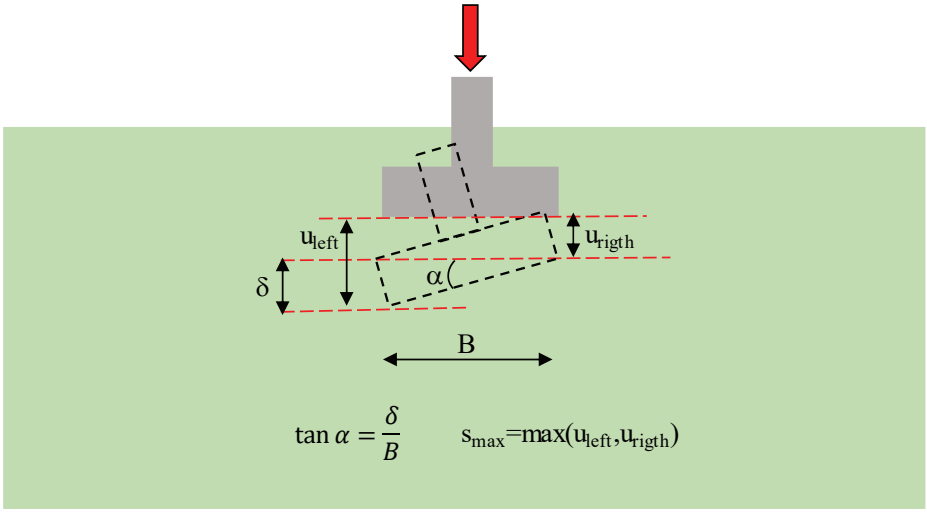

Fig. 7 - Maximum total settlement and angular rotation of the strip footing

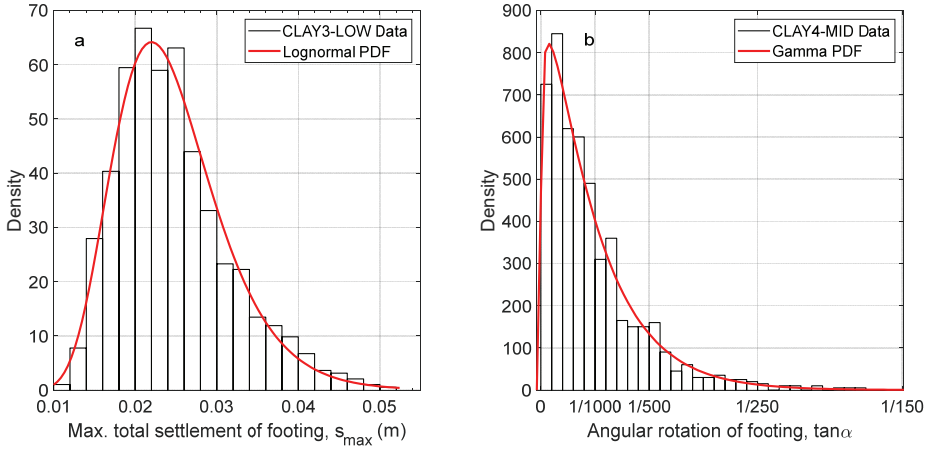

Fig. 8 - Representative PDFs for max. total settlement (a), and angular rotation (b) outputs

4.1. Hazard Curves for Total Maximum Settlement of Strip Footing

The distribution fitter tool was utilized to derive the log-normal cumulative distribution function (CDF) of output PDFs allowing P_f to be estimated directly. All values were reported within a 95% confidence interval, and a sample CDF was presented in Fig. 9. The multiple θ_h/θ_v ratios allowed the anisotropic soil behavior to be considered along with three variability categories. Fig. 10 depicts six proposed total settlement hazard curves for the variability and anisotropy categories. Each color in the graphs embodies different hazard limits, and dashed lines are the confidence bounds of the corresponding hazard curve. Hazard curves illustrated minor deviations in failure probabilities beyond Θ_h=1.0~2.5 relative to changes up to this critical interval. Since the larger the soil volume under the foundation up to a critical value in footing size, the greater the impact of the soil spatial variation.

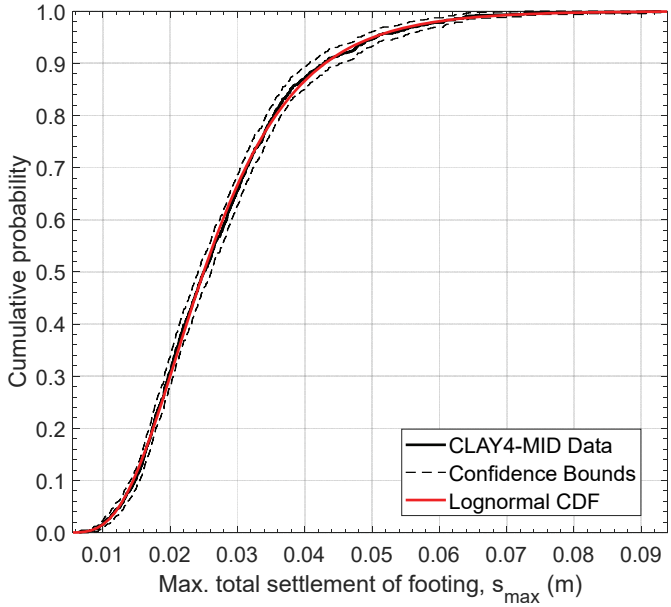

Fig. 9 - Representative CDF for total settlement

4.2. Hazard Curves for Angular Rotation of Strip Footing

The analogy explained in section 4.1 was followed, and Gamma CDF outputs with the 95% confidence level were constructed. The horizontal axis in the CDF plot has been given in fractions obeying the common notation of rotational limits in practice (Fig. 11). Proposed six hazard curves for angular rotation of strip footing was given in Fig. 12.

All the angular rotation plots showed a peak at Θ_h=5, and beyond this value the curves dropped off dramatically near zero, meaning there was no angular rotation in the foundation. In other words, the impact of soil spatial variation in the horizontal direction was critical up

to five times the footing size. Beyond this limit, the soil layer below the footing behaved uniformly regarding soil variability, and no angular rotation occurred.

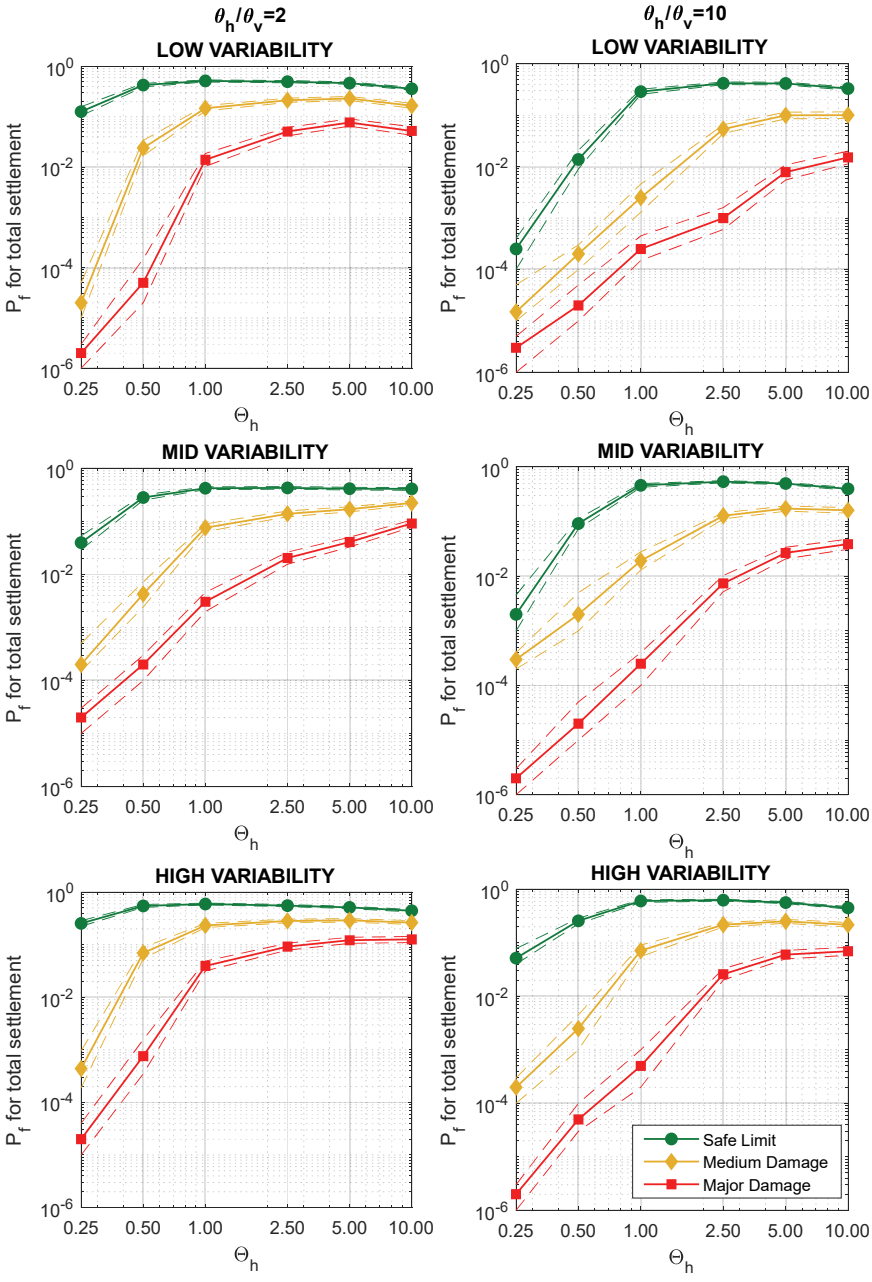

Fig. 10 - Proposed hazard curves for maximum total settlement of strip footing

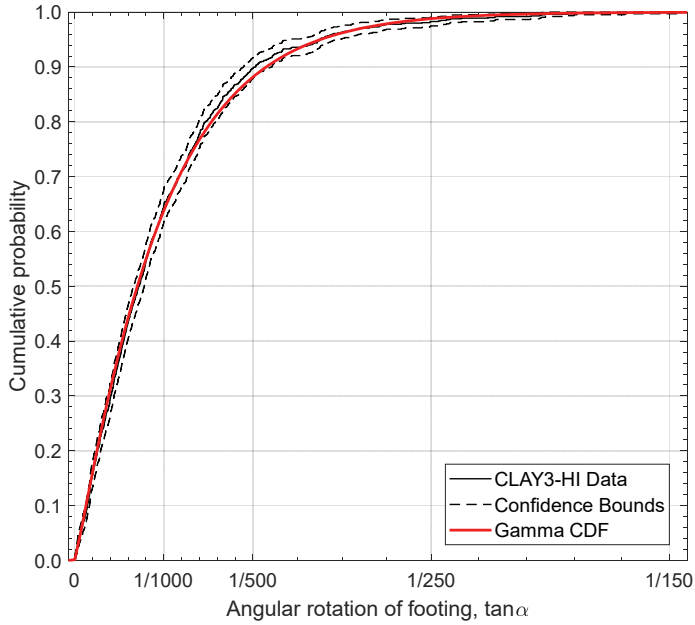

Fig. 11 - Representative CDF for angular rotation output

4.3. Verifications

The effect of mesh scenarios on the deformation behavior of the shallow footing model was examined. Triangular meshes were first generated on a test model with uniform element size, and the settlement of the foundation for this case was recorded. Refined mesh around the footing body was then applied, and the results of this case were also recorded. Load-deformation curves for refined and uniform meshes were compared, and it was confirmed that changing the mesh settings did not influence the deformation behavior.

The RF generation method in the present study was adapted to a reference study on RFEM evaluation of shallow footing. The reference model contained a random field of elasticity modulus for soil [20]. Fig. 13 demonstrates a representative realization of E from the reference work with a mean and standard deviation of 40 MPa and uniform RF with θ=3m.

RF from the prior study was re-generated utilizing the technique of the current research with relatively close ranges to the verification reference. Two representative realizations were given, confirming the validation of the RF generation method used (Fig. 14).

The RF generation function automatically truncated the KL expansion, eliminating the need for a truncation error estimate. For instance, 1600 eigenvalues were employed to generate the 40x40 RF model. The decay of eigenvalues of a representative RF generation demonstrated that the function efficiently truncates the expansion (Fig. 15). All RF generations were controlled utilizing the decay of eigenvalues and the decline was shown to converge to zero, confirming the slight truncation error [31].

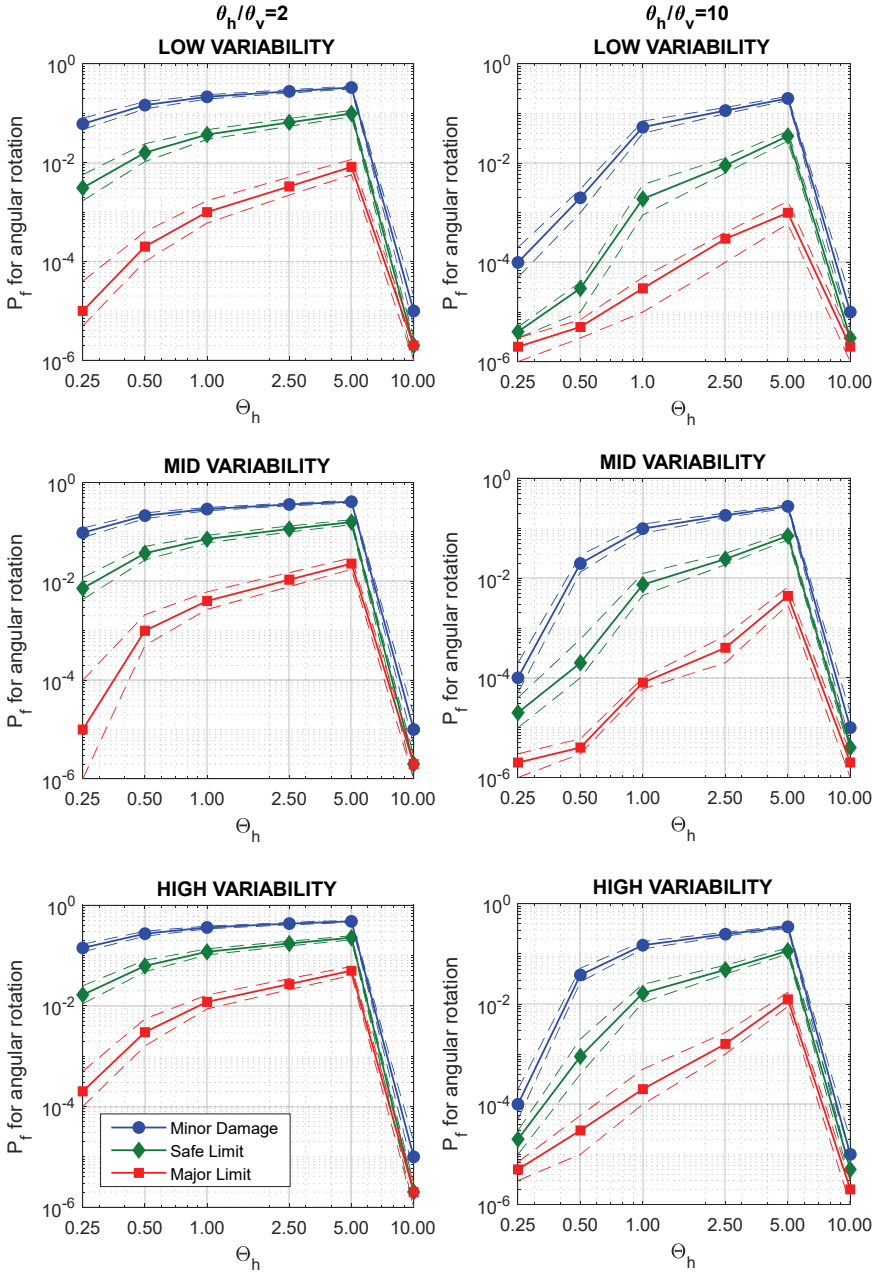

Fig. 12 - Proposed hazard curves for absolute angular rotation of strip footing

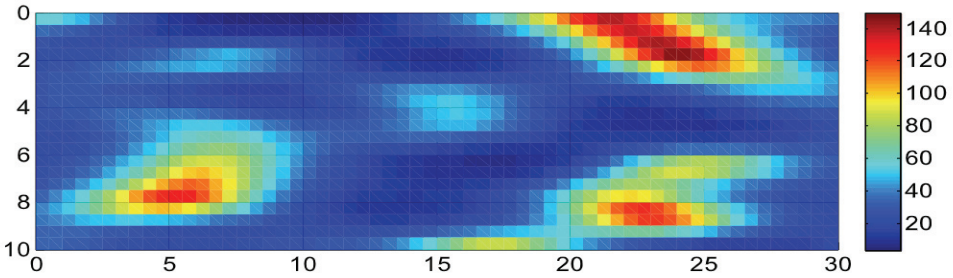

Fig. 13 - Representative realization from verification reference [20]

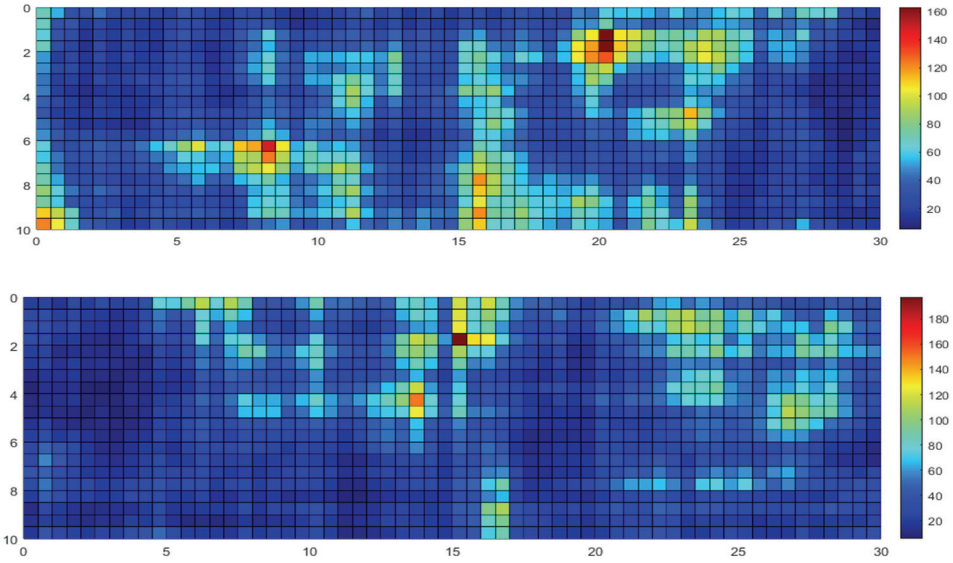

Fig. 14 - Realizations by the method in the present work with the parameters of reference study

The verification reference was also used for the analysis steps confirmation of the current investigation. RFEM attained the total footing settlement with five thousand realizations according to the reference model. Fig. 16 delineates the comparison of reference and calculated output PDFs, and it was found that the outputs of the method were close to the findings of the reference study. Thus, the main framework in the present study has been verified.

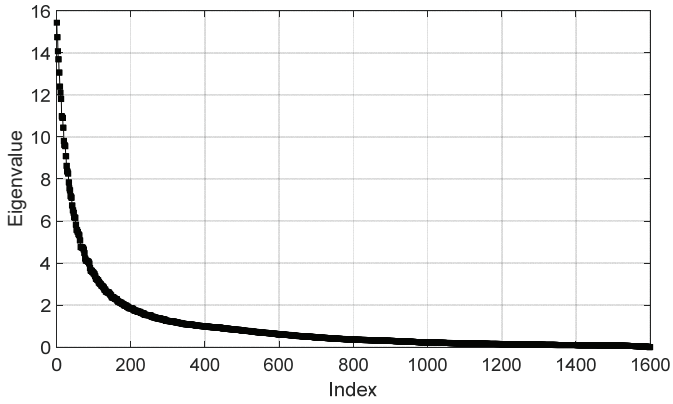

Fig. 15 - The decay in eigenvalue for a representative RF generation

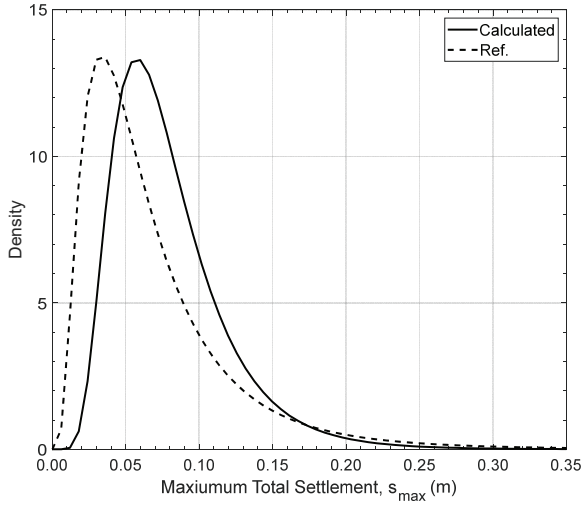

Fig. 16 - Output PDFs calculated by the present method and adopted from the reference study

4.4. Validation of Proposed Hazard Curves

Proposed hazard curves enable the evaluation of shallow foundations utilizing RBD criteria following the soil horizontal and vertical spatial variation in a studied region. Since this type of guidance must be validated before use, a calibration model was produced in the current work analogous to the RFEM models. An actual database was employed to generate RF inputs of the validation model, and the outputs were compared with the proposed hazard curves. An open-source CPT database (304dB) from the International Society of Soil Mechanics and Geotechnical Engineering (ISSMGE) Technical Committee for Risk

Assessment TC304 was used in the validation study. The database entitled TX-CPTU was used to evaluate the proposed hazard curves. The corresponding database contains 9 CPT soundings on stiff over-consolidated CL/CH clays from a region in Baytown, TX, USA. The horizontal spacing of each test point varies between 7.6 to 28.7 m, and the testing depths vary between 3.7 to 15.3m. Extensive research in the region reported that the mean value of correlation length was 0.849m in the vertical direction and 5.830m in the horizontal direction [46]. Thus, θ_v=0.800m and θ_h=5.800m were assumed in the RFEM validation model. The statistical values of RF inputs (E_d, c, and ϕ) were calculated by CPT correlations [47–49], and RFs were generated from 9 CPT in the database. Statistical information of the validation model was summarized in Table 4, and the low variability category was set for the region according to the input COVs.

Table 4 - RF input statistics from the TX-CPTU database

Parameter		**Average**	**Minimum**	**Maximum**
E_d (kPa)	μ	47089	39480	57560
	σ	13967	10260	16607
	COV (%)	29.8	24.1	39.3
c' (kPa)	μ	5.0	3.6	5.8
	σ	4.2	2.8	7.0
	COV (%)	84.2	60.4	131.2
ϕ' (°)	μ	35.8	32.4	38.2
	σ	5.5	4.1	7.0
	COV (%)	15.4	12.4	18.2

The validation model was iteratively solved in FEM code for one thousand realizations, and outputs of total settlement and angular rotation of the strip footing were recorded. Failure probabilities were consequently estimated for the results using the hazard limits. According to the correlation lengths of the validation database, θ_h/B=5.8/4= 1.45 and θ_h/θ_v=5.8/0.8= 7.25 were found. Therefore, the comparison was performed employing the low variability hazard curve with θ_h/θ_v=10 for total settlement and angular rotation. The results were scattered on the corresponding hazard curves, and all resulting points were within the confidence bounds of the curves confirming that the use of proposed hazard curves is valid for RBD of shallow footings on cohesive soils (Fig. 17).

4.5. Worked Example

Many international regulations include the reliability-based design of shallow foundations; for example, ISO has published a standard for the reliability of structures that accepts the probabilistic methods to achieve target reliability [5]. The standard accepts first-order reliability methods (FORM) or full probabilistic methods such as RFEM. Implementation of

the proposed procedure in this context is demonstrated using a worked example of a steel-framed industrial structure supported by 3m wide strip footings sitting on cohesive soil at 1.5m depth. The geometrical detail of the example structure is illustrated in Fig. 18.

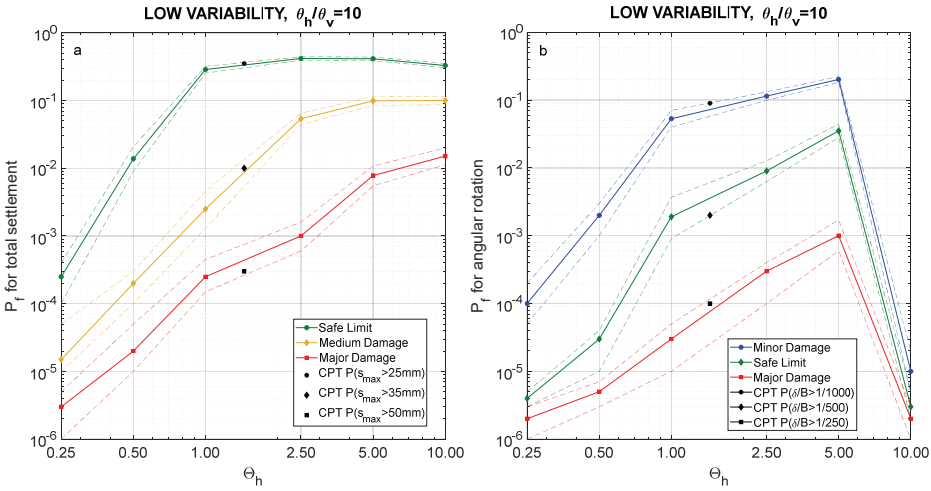

Fig. 17 - Validation of hazard curves with CPT database

A vertical load combination was applied, and the imposed loads for a typical industrial structure were adopted. The exemplary combination of dead load (DL) and live load (LL) was assumed as follows: DD+LL=5+7.5 kN/m2. The results of one frame were considered, and the calculations were given per frame (plane strain condition). It was presumed that a sufficient quantity of soil samples had been collected for the reliability assessment. Soil properties were taken as the mean values from Table 2; μ_E =15MPa, $\mu_{c'}$=5kPa, μ_ϕ=20°, and COVs 0.70, 0.40, 0.15, respectively; confirming the medium variability condition. In addition, soil spatial variability evaluation was assumed to be performed, and θ_h =3.00m θ_v=1.50m was given.

The requirement was to check the existing footing dimensions for the listed parameters. The intermediate structural tolerance to footing settlement was assumed to take the medium damage limits into account. Initially, the analytical (so-called deterministic) solution for SLS calculated the minimum required footing width. Consequently, the soil variation was considered, and computations were performed for the target reliability index (β_{Target}). ISO-2394:2051, in cooperation with JCSS (Joint Committee of Structural Safety), recommends a target reliability index (with associated failure probability) for a one-year reference period with irreversible SLS of β=1.70($P_f \approx 5.10^{-2}$)[50]. The hazard curve for θ_h/θ_v=3.00/1.50=2.00 and MID variability category was selected, and P_f was read for $\Theta_h=\theta_h/B$=3/3=1 as 8.10^{-2} (β=1.40<β_{Target}). Since the target reliability was not fulfilled, the footing dimension should be adjusted accordingly. From the corresponding hazard curve, $\Theta_h \approx 0.90$ was read off for the corresponding target $P_f=5.10^{-2}$. Thus, the resized footing dimension was as follows: $\Theta_h=\theta_h/B$,

0.90=3.00/B => B=3.33m. FORM also computed the footing dimension for β_{Target}, and the summary results of comparison with the proposed method are listed in
Table *5*. The comparison disclosed that the prior footing size was insufficient. Furthermore, it was also noted that the analytic solution does not meet the reliability assessment requirements. Therefore, the aid of a probabilistic technique was essential, particularly in the case of high fluctuation in soil properties.

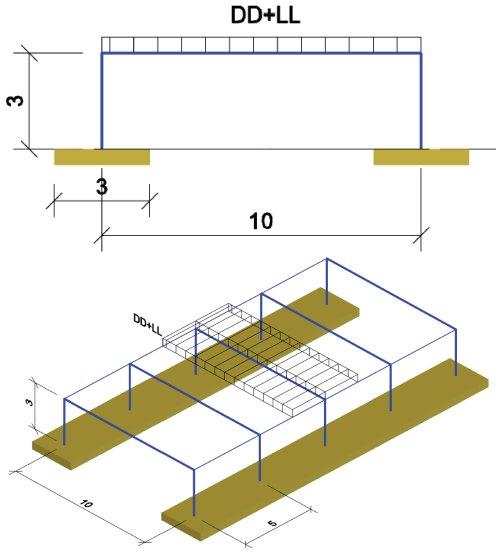

Fig. 18 - Structural geometry of the worked example

Table 5 - Comparison of footing dimensioning by different methods

		Analytical	**Probabilistic Methods**	
	Given	Required by SLS	FORM	Proposed Hazard Curves
Footing Dimension, B (m)	3.00	3.15	3.36	3.33

FORM and the proposed method gave analogous results, but the technique only considered variation in soil properties, not spatial variability. On the other hand, the proposed framework highlighted the necessity of evaluating the spatial variability for RBD of the strip footings by SLS. Table 6 exhibits the differentiation of FORM and the presented method results for footing sizes when considering the spatial variation of soil. The results of the proposed hazard curves indicated that if spatial variability is overlooked in a reliability assessment, the dimensioning could be over- or under-designed depending on the rate of ground uncertainty. The proposed procedure of the latter research has efficiently described this case.

Table 6 - Comparison of dimensioning results for different spatial variability cases

θ_h (m)	θ_v (m)	B_{FORM} (m)	β from hazard curves	$B_{Proposed}$ (m) for β_{Target}=1.70
3.00	1.50	3.36	1.40	3.33
10.00	1.00	3.36	1.00	5.00

5. CONCLUSION

The present work proposed hazard curves for footing deformation of strip foundations on cohesive soils with the variability and anisotropy categories. Hazard curves were constructed considering the variations in soil shear strength and rigidity parameters. The multiple θ_h/θ_v ratios allowed the anisotropic soil behavior to be considered along with three variability categories The necessity of quantifying soil spatial variability for RBD of strip footings on cohesive soils was underlined.

Overall settlement hazard curves exhibited minor deviation in failure probabilities over Θ_h=1.0~2.5 compared to variations up to this critical range. The reason was that the larger the soil volume under the foundation up to a decisive value in size B, the greater the impact of the soil spatial variation.

All plots for angular rotation showed a peak at Θ_h=5, and beyond this value curves dropped off dramatically near zero, meaning there was no angular rotation in the footing. In other words, the influence of spatial variation of soil in the horizontal direction was critical up to five times the footing size. Beyond this limit, the soil layer below the foundation behaved uniformly regarding soil variability, and no angular rotation occurred.

Proposed hazard curves for shallow foundations were introduced to the literature, considering both elasto-plastic soil behavior with the Mohr-Coulomb failure criterion and the impact of all influencing parameters that comply with the deformation limits in the foundation regulations. The proposed technique provided a probabilistic study of strip foundations considering the spatial variation of clayey soils and a valid procedure for RBD with SLS.

Declaration of Competing Interest

The authors declare that they have no known competing financial interests or personal relationships that could have appeared to influence the work reported in this paper.

Acknowledgments

The authors would like to thank the members of the TC304 Committee on Engineering Practice of Risk Assessment & Management of the ISSMGE for developing the database 304dB used in this study and making it available for scientific inquiry. We also wish to thank Armin D. Stuedlein for contributing this database to the TC304 compendium of databases. A part of the study was conducted under the support of the scientific research project within the doctoral study of the corresponding author at Istanbul Kultur University (Grant No: BAP2202).

Abbreviations

CDF : cumulative distribution function
COV : coefficient of variation
CPT : cone penetration test
DD : dead load
FE : finite elements
FEM : finite element method
FKN : normal stiffness factor
FORM : first order reliability method
KL : Karhunen-Loeve
LL : live load
MC : Mohr-Coulomb
PDF : probability density function
RBD : reliability-based design
RF : random field
RFEM : random finite element method
SFEM : stochastic finite element method
SLS : serviceability limit state

Symbols

α : rotation angle
β : reliablity index
δ : settlement difference
ε, ε^e, ε^p : total, elastic and plastic strain
ϕ : angle of shearing resistance
λ_i : eigenvalue of random field
μ : mean
ν : Poisson's ratio
Ω : random field domain
ρ : correlation function

σ : standard deviation

$\{\sigma\}$: stress vector

θ, θ_h, θ_v : correlation length, horizontal and vertical correlation length

Θ_h : dimensionless horizontal correlation length

τ : distance between two random variables

$\xi_i(\theta)$: standard normal variate

B : footing width

c : soil cohesion

D : elasticity matrix

D_f : depth of embedment

E, E_d : modulus of elasticity, deformation modulus of soil

{F} : load vector

F_i : random field matrix

f_i : random field realization

$g_i(\mathbf{x})$: eigenfunction of random field

[K] : rigidity matix

P_f : probability of failure

s_{max} : maximum total settlement

t : footing thickness

{u} : displacement vector

x : random variable vector

x_i : random variable

References

[1] EN-1997-1, Eurocode 7: Geotechnical design- Part 1: General Rules, CEN European Committee for Standardization, Brussels, 2004.

[2] K.K. Phoon, F.H. Kulhawy, Characterization of geotechnical variability, Can. Geotech. J. 36 (1999) 612–624. https://doi.org/10.1139/t99-038.

[3] K.K. Phoon, F.H. Kulhawy, Evaluation of geotechnical property variability, Can. Geotech. J. 36 (1999) 625–639. https://doi.org/10.1139/t99-039.

[4] EN-1990:2002, Eurocode. Basis of Structural Design, CEN European Committee for Standardization, Brussels, 2002.

[5] ISO-2394:2015, General Principles on Reliability of Structures., International Organization for Standardization, Geneva, 2015.

[6] E.H. Vanmarcke, Probabilistic Modeling of Soil Profiles, ASCE J Geotech Eng Div. 103 (1977) 1227–1246. https://doi.org/10.1016/0148-9062(78)90012-8.

[7] E.H. Vanmarcke, Random Fields: Analysis and Synthesis, World Scientific, London&New Jersey, 2010. https://doi.org/https://doi.org/10.1142/5807.

[8] G.B. Beacher, T.S. Ingra, Stochastic Fem in Settlement Predictions, J. Geotech. Eng. Div. 107 (1981) 449–463. https://doi.org/10.1061/ajgeb6.0001119.

[9] D. V. Griffiths, G.A. Fenton, Probabilistic settlement analysis by stochastic and random finite-element methods, J. Geotech. Geoenvironmental Eng. 135 (2009) 1629–1637. https://doi.org/10.1061/(ASCE)GT.1943-5606.0000126.

[10] A. Ahmed, A.H. Soubra, Probabilistic analysis of strip footings resting on a spatially random soil using subset simulation approach, Georisk. 6 (2012) 188–201. https://doi.org/10.1080/17499518.2012.678775.

[11] G.A. Fenton, D. V. Griffiths, Risk Assessment in Geotechnical Engineering, John Wiley & Sons, Inc., Hoboken, NJ, USA, 2008. https://doi.org/10.1002/9780470284704.

[12] G.M. Paice, D. V. Griffiths, G.A. Fenton, Finite element modeling of settlements on spatially random soil, J. Geotech. Eng. 122 (1996) 777–779. https://doi.org/10.1061/(asce)0733-9410(1996)122:9(777).

[13] A. Ahmed, A.H. Soubra, Probabilistic analysis at the serviceability limit state of two neighboring strip footings resting on a spatially random soil, Struct. Saf. 49 (2014) 2–9. https://doi.org/10.1016/j.strusafe.2013.08.001.

[14] G.A. Fenton, D. V. Griffiths, Three-dimensional probabilistic foundation settlement, J. Geotech. Geoenvironmental Eng. 131 (2005) 232–239. https://doi.org/10.1061/(ASCE)1090-0241(2005)131:2(232).

[15] T. Al-Bittar, A.H. Soubra, Probabilistic analysis of strip footings resting on spatially varying soils and subjected to vertical or inclined loads, J. Geotech. Geoenvironmental Eng. 140 (2014). https://doi.org/10.1061/(ASCE)GT.1943-5606.0001046.

[16] J.T. Simões, L.C. Neves, A.N. Antão, N.M.C. Guerra, Reliability assessment of shallow foundations on undrained soils considering soil spatial variability, Comput. Geotech. 119 (2020) 103369. https://doi.org/10.1016/j.compgeo.2019.103369.

[17] D. V. Griffiths, G.A. Fenton, Bearing capacity of spatially random soil: The undrained clay Prandtl problem revisited, Geotechnique. 51 (2001) 351–359. https://doi.org/10.1680/geot.2001.51.4.351.

[18] M.J. Cassidy, M. Uzielli, Y. Tian, Probabilistic combined loading failure envelopes of a strip footing on spatially variable soil, Comput. Geotech. 49 (2013) 191–205. https://doi.org/10.1016/j.compgeo.2012.10.008.

[19] J. Ching, Y.G. Hu, Effective Young's Modulus for a Footing on a Spatially Variable Soil Mass, Geotech. Spec. Publ. (2017) 360–369. https://doi.org/10.1061/9780784480717.034.

[20] Q. Yue, J. Yao, Soil deposit stochastic settlement simulation using an improved autocorrelation model, Probabilistic Eng. Mech. 59 (2020) 103038. https://doi.org/10.1016/j.probengmech.2020.103038.

[21] A.E. Kenarsari, R. Jamshidi Chenari, Probabilistic settlement analysis of shallow foundations on heterogeneous soil stratum with anisotropic correlation structure, Geotech. Spec. Publ. GSP 256 (2015) 1905–1914. https://doi.org/10.1061/9780784479087.174.

[22] A. Johari, A. Sabzi, A. Gholaminejad, Reliability Analysis of Differential Settlement of Strip Footings by Stochastic Response Surface Method, Iran. J. Sci. Technol. - Trans. Civ. Eng. 43 (2019) 37–48. https://doi.org/10.1007/s40996-018-0114-3.

[23] K. Winkelmann, K. Żyliński, A. Korzec, J. Górski, Effectiveness of Random Field Approach in Serviceability Limit State Analysis of Strip Foundation, Geotech. Geol. Eng. 40 (2022) 4705–4720. https://doi.org/10.1007/s10706-022-02179-6.

[24] E. Arel, A.C. Mert, Field simulation of settlement analysis for shallow foundation using cone penetration data, Probabilistic Eng. Mech. 66 (2021) 103169. https://doi.org/10.1016/j.probengmech.2021.103169.

[25] S.K. Jha, Reliability-based analysis of bearing capacity of strip footings considering anisotropic correlation of spatially varying undrained shear strength, Int. J. Geomech. 16 (2016) 1–10. https://doi.org/10.1061/(ASCE)GM.1943-5622.0000638.

[26] Y. Wu, X. Zhou, Y. Gao, S. Shu, Bearing capacity of embedded shallow foundations in spatially random soils with linearly increasing mean undrained shear strength, Comput. Geotech. 122 (2020) 103508. https://doi.org/10.1016/j.compgeo.2020.103508.

[27] C. Mendoza, J.E. Hurtado, The Importance of Geotechnical Random Variability in the Elastoplastic Stress–Strain Behavior of Shallow Foundations Considering the Geological History, Geotech. Geol. Eng. 40 (2022) 3799–3818. https://doi.org/10.1007/s10706-022-02132-7.

[28] R. Popescu, G. Deodatis, A. Nobahar, Effects of random heterogeneity of soil properties on bearing capacity, Probabilistic Eng. Mech. 20 (2005) 324–341. https://doi.org/10.1016/j.probengmech.2005.06.003.

[29] M.A. Lawrence, Basis random variables in finite element analysis, Int. J. Numer. Methods Eng. 24 (1987) 1849–1863. https://doi.org/10.1002/nme.1620241004.

[30] P.D. Spanos, R. Ghanem, Stochastic finite element expansion for random media, J. Eng. Mech. 115 (1989) 1035–1053. https://doi.org/10.1061/(ASCE)0733-9399(1989)115:5(1035).

[31] S.P. Huang, S.T. Quek, K.K. Phoon, Convergence study of the truncated Karhunen-Loeve expansion for simulation of stochastic processes, Int. J. Numer. Methods Eng. 52 (2001) 1029–1043. https://doi.org/10.1002/nme.255.

[32] D. Mirfendereski, On series representation of random fields and their application in stochastic finite element analysis, California, 1990.

[33] R.G. Ghanem, P.D. Spanos, Spectral stochastic finite-element formulation for reliability analysis, J. Eng. Mech. 117 (1991) 2351–2372. https://doi.org/10.1061/(ASCE)0733-9399(1991)117:10(2351).

[34] K.K. Phoon, S.P. Huang, S.T. Quek, Implementation of Karhunen-Loeve expansion for simulation using a wavelet-Galerkin scheme, Probabilistic Eng. Mech. 17 (2002) 293–303. https://doi.org/10.1016/S0266-8920(02)00013-9.

[35] A. Der Kiureghian, J. Bin Ke, The stochastic finite element method in structural reliability, Probabilistic Eng. Mech. 3 (1988) 83–91. https://doi.org/10.1016/0266-8920(88)90019-7.

[36] P.L. Liu, A. Der Kiureghian, Finite element reliability of geometrically nonlinear uncertain structures, J. Eng. Mech. 117 (1991) 1806–1825. https://doi.org/10.1061/(ASCE)0733-9399(1991)117:8(1806).

[37] P. Kohnke, Theory Reference for the Mechanical APDL and Mechanical Applications, Canonsburg, PA, 2009.

[38] J.E. Bowles, Foundation Analysis and Design, McGraw-Hill, 1997. https://books.google.com.tr/books?id=iuBwtgAACAAJ.

[39] G.A. Fenton, D. V. Griffiths, Probabilistic foundation settlement on spatially random soil, J. Geotech. Geoenvironmental Eng. 128 (2002) 381–390. https://doi.org/10.1061/(ASCE)1090-0241(2002)128:5(381).

[40] M. Budhu, Soil Mechanics and Foundations, 3rd Edition, John Wiley & Sons, Incorporated, 2010. https://books.google.com.tr/books?id=ga8bAAAAQBAJ.

[41] F.H. Kulhawy, K.K. Phoon, M. Grigoriu, E.P.R. Institute, C.U.G.E. Group, Reliability-based Design of Foundations for Transmission Line Structures, Prepared for Electric Power Research Institute, 1995. https://books.google.com.tr/books?id=dSpUAAAAYAAJ.

[42] M. Lloret-Cabot, G.A. Fenton, M.A. Hicks, On the estimation of scale of fluctuation in geostatistics, Georisk. 8 (2014) 129–140. https://doi.org/10.1080/17499518.2013.871189.

[43] B.M. Das, Principles of Foundation Engineering, Cengage Learning, 2010. https://books.google.com.tr/books?id=v3Mq9szzE1YC.

[44] D.P. Coduto, Foundation Design: Principles and Practices, Pearson Education, 2015. https://books.google.com.tr/books?id=xa6gBwAAQBAJ.

[45] P.G. Constantine, Random Field Simulation (https://www.mathworks.com/matlabcentral/fileexchange/27613-random-field-simulation), (2020).

[46] A.W. Stuedlein, S.L. Kramer, P. Arduino, R.D. Holtz, Geotechnical Characterization and Random Field Modeling of Desiccated Clay, J. Geotech. Geoenvironmental Eng. 138 (2012) 1301–1313. https://doi.org/10.1061/(asce)gt.1943-5606.0000723.

[47] P.K. Robertson, K.L. Cabal, Guide to Cone Penetration Testing for Geotechnical Engineering, California, 2015.

[48] P.K. Robertson, R.G. Campanella, Interpretation of cone penetration tests. Part II: clay., Can. Geotech. J. 20 (1983) 734–745. https://doi.org/10.1139/t83-079.

[49] K. Senneset, R. Sandven, N. Janbu, Evaluation of soil parameters from piezocone tests, Transp. Res. Rec. (1989) 24–37.

[50] JCSS, Probabilistic Model Code Part 1 - Basis of Design, Joint Committee of Structural Safety, 2001.

Turkish Journal of Civil Engineering, 2023, 29-52, Paper 750, ***Research Article***

Novel Imperfection Method for Post-Buckling Strength of C-Sectioned CFS Members

Ozge Gizem CAGRICI[1]
Rafet AKTEPE[2]
Burcu GULDUR ERKAL[3*]

ABSTRACT

The overall behavior of cold-formed steel (CFS) members is significantly affected from existing geometric imperfections. In this work, a mode shape-based imperfection coefficient computation method is developed to investigate the effects of initial geometric imperfections on member behavior. The point clouds of CFS members are collected and used to extract imperfection distributions and coefficients. The computed coefficients are integrated into the numerical model for analysis. Finally, axial loading tests are conducted to compare the numerical and experimental results. The results obtained using mode shape-based imperfection coefficients are generally closer to the experimental results than the common method used in practice.

Keywords: Cold-formed steel members, geometric imperfection detection, 3D scanning, finite element analysis, effects of initial geometric imperfections, automated deviation detection, column tests.

1. INTRODUCTION

The use of CFS is widespread in low-rise residential and industrial buildings. Especially in recent years, CFS usage has progressed visibly with advancing technology and increased research on this subject. From a usage point of view, CFS has many advantages. CFS has a high strength-to-weight ratio, dimensional stability, does not expand with humidity, etc. Even though CFS construction has several advantages, the members are prone to geometric imperfections during manufacturing, transportation, and installation. These geometric imperfections then significantly affect the individual behavior of CFS members.

Note:
- This paper was received on November 30, 2022 and accepted for publication by the Editorial Board on August 4, 2023.
- Discussions on this paper will be accepted by January 31, 2024.

1.https://doi.org/10.18400/tjce.1212403

1 Hacettepe University, Department of Civil Engineering, Ankara, Türkiye
ozge.cagrici@hacettepe.edu.tr - https://orcid.org/0000-0003-0719-8702

2 Hacettepe University, Department of Civil Engineering, Ankara, Türkiye
rafet.aktepe@hacettepe.edu.tr - https://orcid.org/0000-0003-0436-5683

3 Hacettepe University, Department of Civil Engineering, Ankara, Türkiye
burcuguldur@hacettepe.edu.tr - https://orcid.org/0000-0001-5757-736X

* Corresponding author

Previous research performed on CFS structures showed that the accuracy of the numerical models generated to analyze the behavior of CFS members is directly dependent on the model inputs. In particular, how the geometric imperfections in the CFS members are reflected in the numerical model significantly changes the analysis results. This paper aims to use point clouds collected from CFS members by three-dimensional scanning technology to detect each CFS member's geometric imperfections automatically. The detected geometric imperfections are then represented in terms of mode shapes determined by an eigen-buckling analysis. Finally, the obtained mode shape-based imperfection coefficients are integrated into the numerical model to investigate the effects of geometric imperfection on CFS member behavior. The obtained numerical results are then compared with experimental results.

Several studies in the literature focused only on extracting geometric defects from CFS members. Peterman [1] used a specialized setup to measure imperfections at seven different spots (one specific location at a time) around the cross-section. Seven locations at the cross-sectional level were used by McAnallen, Padilla-Llano [2] to measure imperfection fields. They created a standard method for representing geometric imperfections using these observations as well as measurements from earlier studies. Zhao, Tootkaboni [3] created a test system that comprises a 2D line laser spanning widths up to 240 mm as the first attempt to apply 3D measurements for CFS geometric imperfection distribution extraction. To study the buckling deformation of built-up CFS columns, Salomon, Fratamico [4] used high-resolution optical cameras and computer vision techniques to construct 3D models that included position and time data. High-fidelity measurements of geometric imperfections were carried out by Zhao, Tootkaboni [5], who then used these data to characterize the distributions of geometric imperfections per different simulation techniques. In another investigation, cross-section dimensions and imperfections were determined using laser scan data of CFS members by Zhao, Tootkaboni [6]. Finally, to measure variations in CFS channel sections, Selvaraj and Madhavan [7] employed a 3D non-contact laser scanning technique. For the extraction of geometric imperfections, 27 deviation measurement points at the cross-section level were used. However, the effects of the extracted defects on CFS member behavior were not investigated in these studies.

The following studies, on the other hand, have concentrated both on extracting geometric defects and examining how they affect the behavior of CFS members. In Dubina and Ungureanu [8], several methods were developed to detect geometric imperfections and their integration into the finite element model. They discussed the effects of local and distortional geometric imperfections on buckling strength. Another study was performed to model geometric imperfections using different methods and compared the obtained results with the experimental results [9]. Zeinoddini and Schafer [10] developed a technique that combines modal approaches and spectral representations to extract the distributions of geometric imperfections. Nonlinear collapse analysis was performed using the obtained imperfection distributions. Garifullin and Nackenhorst [11] conducted a nonlinear buckling analysis on C-section columns. The sensitivity of the load-bearing capacity of CFS members to the geometric imperfections was examined. Another numerical study investigated the effect of initial geometric imperfections on the ultimate moment capacity of simply-supported sigma-sectioned CFS beams [12]. Sadovský, Kriváček [13] examined the effects of initial geometric imperfections on CFS members' buckling strength by performing computational modeling. This study aimed to determine the most unfavorable geometric imperfections represented by the eigenmode shapes in the geometric and material-nonlinear finite element analysis (FEA)

of CFS members with imperfections (GMNIA). Zeinoddini and Schafer [14] performed an experimental study to characterize global bow, camber, and twist in CFS- lipped channel members and record the dimensional changes. Martins, Dinis [15] carried out a numerical investigation to observe the influence of local–distortional (L–D) interaction on the ultimate strength of web-stiffened and lipped channel CFS columns. In Li [16], the effects of geometric imperfections on the buckling mode interaction of C-sectioned CFS members were observed. Nonlinear collapse analyses were performed using ABAQUS/CAE [17] to investigate these interactions. Deformations obtained from the analyses were divided into local, distortional, and global deformation modes.

The previous studies mentioned above, although valuable, have limitations in representing the actual geometry of CFS members due to the use of a limited number of data points. To overcome this limitation, it is crucial to develop robust strategies that can extract defects from entire geometric representations. In this paper, an improvement is made by obtaining the geometric imperfections of each CFS member from point clouds captured through a 3D data collection system. These extracted imperfections are then integrated into numerical models to investigate their effects on member behavior. Additionally, axial loading tests are conducted on the previously scanned CFS members to validate the results obtained from the numerical models. Prior research on axial loading tests of CFS members and numerical modeling is also examined to ensure successful tests and the development of efficient numerical models capable of accurately capturing observed behavior [18-22].

The structure of the work presented in this paper is as follows. To begin with, the point clouds that fully reflect the geometries of the scanned objects are obtained. Later, the method developed to obtain geometric imperfections in the members using point clouds automatically is laid out. Then, the obtained geometric imperfections are integrated into the numerical models to investigate the effects of these imperfections on the members' behavior. The finite element analysis performed to observe these effects is carried out in two steps. First, an eigenvalue elastic buckling analysis is performed to establish the buckling modes (eigenmodes). The members' extracted geometric imperfections are then decomposed into the deflected member shapes corresponding to each buckling mode to obtain imperfection coefficients. Second, a general geometrical and material nonlinear static analysis with imperfections (GMNIA) was performed to simulate the structural behavior of CFS members. Parallel to these studies, axial compression tests are carried out on previously scanned members. The experimental results are then compared with the finite element analysis outputs obtained for traditional and point cloud-based geometric imperfection integration strategies.

2. POINT CLOUD DATA COLLECTION

In this work, geometric imperfections on CFS members are extracted automatically from point clouds collected via a 3D data collection system.

2.1. Details of the Available CFS Members

In total, 16 C-sectioned CFS members with varying dimensions and with/without pre-punched slotted web holes are examined in this work. The investigated CFS members are labeled as follows: cross-section type – nominal web height – member length – specimen

with or without holes – sequence number. All the investigated CFS members have a flange width of 45 mm, web height of 90 mm, lip width of 10 mm, and thickness of 1.2 mm. For example, C-90-900-NH-1 represents a first C-sectioned member with a web height of 90 mm, member length of 900 mm, and no holes.

2.2. Scanner used for Point Cloud Collection

A 3D optical scanning system, a Breuckmann 3D scanner (rebranded as SmartScan, HEXAGON [24]) with the highest accuracy of 3 microns, is used to collect point clouds. This scanner offers mono and color scanning with medium to super-high resolutions. The field of view varies from 30 mm to 1.5 meters. Each CFS member is positioned 1 meter away from the scanner during scanning, and the high-resolution option is selected. The scanner is then moved around the member to obtain full coverage. Further detail on the collected point clouds for each investigated CFS member can be found in Guldur Erkal and Cagrici [25].

3. AUTOMATED GEOMETRIC IMPERFECTION DETECTION AND QUANTIFICATION METHOD

The geometric imperfection extraction in this work is performed using the method laid out in Guldur Erkal and Cagrici [25]. This method focuses on conducting an automated cross-section-based geometric imperfection detection and quantification. As a result, representative keypoints at successive cross-sections along the longitudinal axis of the CFS members are extracted and used for geometric imperfection quantification. The geometric imperfections are computed based on common representations given in Figure 1. The automated cross-section-based geometric imperfection detection and quantification results for the investigated CFS members are presented in Guldur Erkal and Cagrici [25].

4. MODE SHAPE-BASED GEOMETRIC IMPERFECTION COEFFICIENT EXTRACTION

The effects of the extracted geometric imperfections on member behavior could be examined by introducing these imperfections into numerical models. Even though there are several ways to perform this (such as mesh alteration or constant imperfection coefficient usage), they either increase the computational cost or underestimate the member strength. Thus, this paper introduces a novel mode shape-based geometric imperfection coefficient computation. This method represents each member's existing geometric imperfections in buckling mode shapes.

In this section, the details of the performed eigen-buckling analysis are given. The appropriate least-squares method specializing in overdetermined equations, which is used to reconstruct the geometric imperfections based on the mode shapes obtained by the performed eigen-buckling analysis, is then laid out.

The mode shapes that form the geometric imperfections can be determined by eigen-buckling analysis. The geometric imperfection representations are obtained by combining the relevant local, distortional, or overall buckling modes of the cross-section or member. They are later used to invoke geometric nonlinearity during further numerical analysis [26]. Thus, the

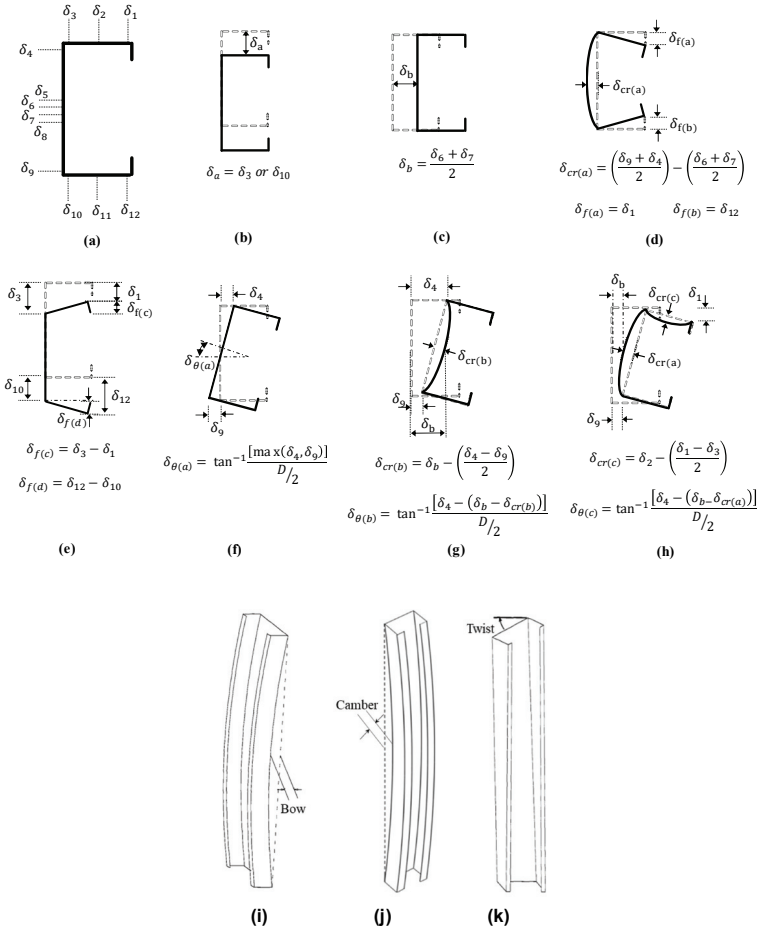

Figure 1 - Local geometric imperfection formulations: (a) keypoint deviations, (b) cross-section shift orthogonal to the flanges, (c) cross-section shift orthogonal to the web, (d) convex crown, (e) flare, (f) twist only, (g) twist with concave crown, and (h) twist with convex crown and concave flange; and global imperfection representations: (i) bow, (j) camber, and (k) twist (revisited from Guldur Erkal and Cagrici [25]).

standard application for taking the imperfection effects into account during numerical analysis is to perform an eigen-buckling analysis and to introduce the imperfections to the numerical model by multiplying the buckling mode shape outputs with specific coefficients. Generally, the first mode is multiplied by 0.1t, t is the thickness of the CFS member, and the consecutive mode shapes are multiplied with decreasing coefficients, i.e., 0.1t for mode shape 1, 0.05t for mode shape 2, and the rest of the coefficients decrease with the same trend. Koiter [27] states imperfection sensitivity may be most efficiently expressed as a function of imperfection magnitudes in the buckling mode shapes. Thus, the maximum imperfections provide a reasonable lower bound strength analysis criterion.

4.1. Eigen-Buckling Analysis

In this study, ABAQUS/CAE [17] is used for both eigen-buckling and GMNIA to simulate the behavior of the C-sectioned CFS columns under axial loading. For eigen-buckling analysis, subspace iteration is chosen as the eigenvalue extraction method. The roundness of corners is not considered in the ABAQUS models. Consequently, residual stresses and cold-work effects are neglected [13, 28-30].

4.1.1. Element Type and Mesh

All C-sectioned CFS columns are modeled by selecting the S4R thin shell element. A convergence study was carried out to determine the suitable mesh size, considering both axial load capacity predictions and computational time. Based on the results of the convergence study, the appropriate mesh size for the elements was determined as 2.5 mm x 2.5 mm (Figure 2).

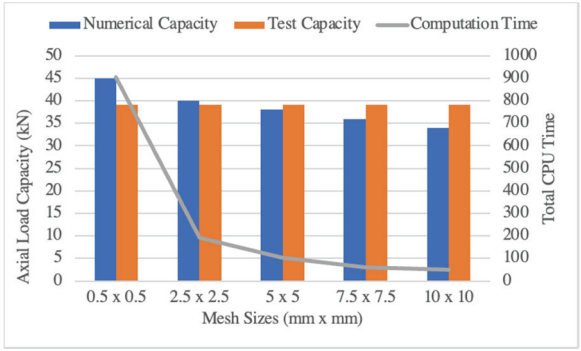

Figure 2 - Comparison of the test capacity with numerical capacities and computational times.

4.1.2. Material Properties

The material properties of the specimens are determined by tensile coupon tests according to the ASTM E8/E8M Standard ASTM-E8/E8M [31]. Three tensile coupons were sampled from the specimens. The obtained engineering stress-strain curves of the tensile coupon tests are given in Figure 3.

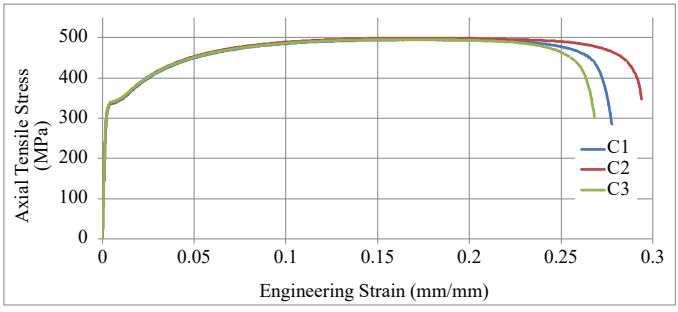

Figure 3 - Engineering stress-strain curves of the test coupons C1, C2, and C3.

The engineering stress (σ_{eng})-engineering strain (ε_{eng}) data obtained from tensile coupon tests need to be converted into true stress (σ_{true})-true strain (ε_{true}) data before being inserted into the numerical models. Equations [1] and [2] are used for the initial conversion. Finally, the obtained true strain is converted into plastic strain ($\varepsilon_{true\ (pl)}$) data with Equation [3] to model material nonlinearity with von Mises yield criterion and isotropic hardening.

$$\sigma_{true} = \sigma_{eng}(1 + \varepsilon_{eng}) \quad (1)$$

$$\varepsilon_{true} = \ln(1 + \varepsilon_{eng}) \quad (2)$$

$$\varepsilon_{true\ (pl)} = \ln(1 + \varepsilon_{eng}) - \frac{\sigma_{true}}{E} \quad (3)$$

4.1.3. Material Modelling

Material nonlinearity of the specimens is modeled with von Mises yield criteria and isotropic hardening. Yield strength of 333 MPa, an ultimate strength of 496 MPa, and a Young's Modulus of 186 MPa, obtained from tensile coupon tests, are used.

4.1.4. Boundary Conditions

All columns are modeled using fixed support conditions. Reference nodes at the centroid of cross-sections are defined at each end. All the nodes at one end of the column located on the surface are tied to the reference node using the 'rigid-body' 'fixed' constraint. All degrees of freedom are restricted at one reference node (bottom end). In contrast, all degrees of freedom are restricted at the opposite end except in the longitudinal direction, where the loading is applied.

4.1.5. Mode Shapes

The first 20 mode shapes of each investigated CFS member are extracted for performing mode shape-based imperfection coefficient extraction. Sample mode shape results for C-90-1100-NH-1 obtained after eigen-buckling analysis is given in Figure 4.

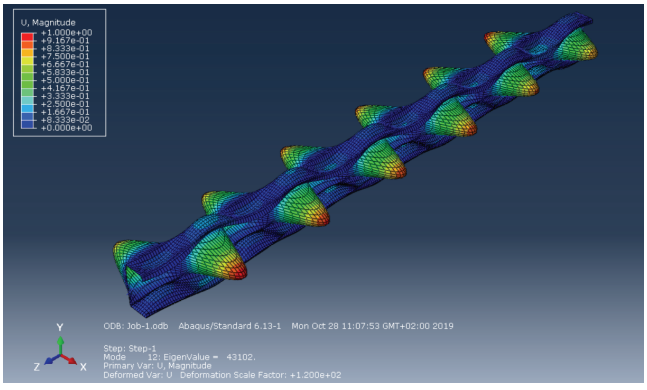

Figure 4 - C-sectioned column, C-90-1100-NH-1 - Mode shape 12

4.2. Overdetermined Equations

The magnitudes of geometric imperfections are already determined using the previously described automated geometric imperfection detection and quantification method. To perform the imperfection quantification, keypoints located at each cross-section cut along the length of each member are extracted (Figure 5a). The finite element mesh is specifically tailored to match the extracted keypoint locations. The same positive and negative directions used for automated geometric imperfection detection and quantification method are used to record mode shape displacements. If the movement is outside the reference cross-section, the displacements are recorded as positive. The displacements are recorded as negative values if the movement is inward. Figure 5b shows both positive displacement directions for different subgroups of 12 keypoints with respect to the reference cross-section of a point cloud sample. Figure 5c shows the matching keypoints (with the point cloud cross-sections) on the ABAQUS model of C-90-1100-NH-1.

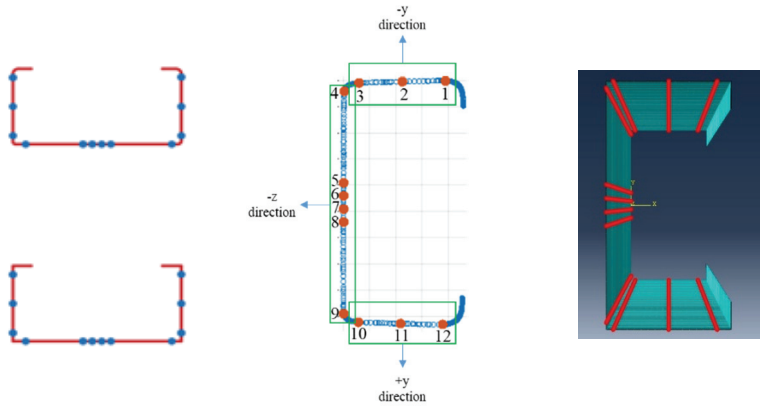

(a) (b) (c)

Figure 5 - (a) Accurate and simplified cross-section representation with keypoints, (b) positive displacement directions for different subgroups of 12 keypoints with respect to the reference cross-section (with keypoint labels), and (b) keypoints on the ABAQUS model of C-90-1100-NH-1.

Once the displacements corresponding to each keypoint for all 20 mode shapes are recorded, the entire set of equations is solved to get the best overall coefficient that takes 12 keypoints at each cross-section cut into account to capture the geometric imperfection on CFS members. Sample geometric imperfection representation for a single keypoint is given in Figure 6(a). It should be noted that the extracted geometric imperfections at each keypoint are later shifted towards the horizontal axis to get a mean value of zero. This step is essential since the mean values of all the displacement recorded for local mode shapes are zero. Thus, if the mode shapes will be used for coefficient determination, the geometric imperfection should be suitable for decomposed representation. Figure 6(a) shows a sample displacement variation of the 12th keypoint along the length of C-90-1100-NH-1. Displacement variations of the 12th keypoint along the length of C-90-1100-NH-1 for the first 20 mode shapes are shown in Figure 6(b).

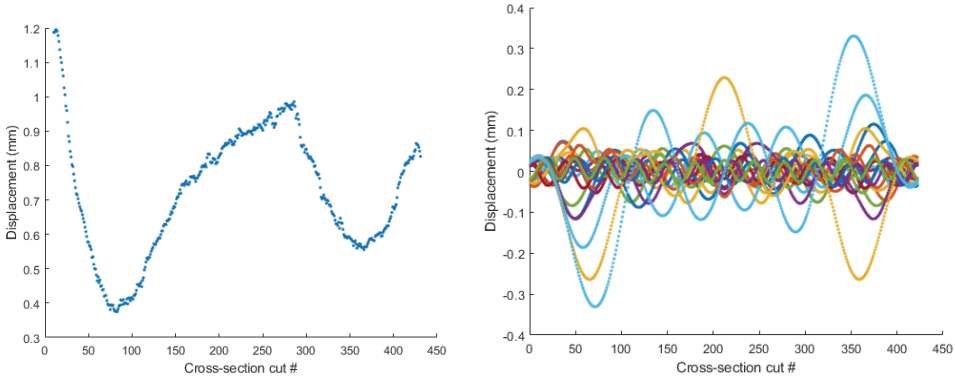

(a) (b)

Figure 6 - Displacement variations of the 12th keypoint along the length of C-90-1100-NH-1 obtained (a) from the member's point cloud and (a) from the analysis model for the first 20 mode shapes.

Consider a system of linear equations (Equation [4]):

$$y = Hx \tag{4}$$

If the total number of equations is greater than the unknowns (***H*** is a tall matrix), then the system is specified as overdetermined. An overdetermined system almost never has a solution. For this research, the sizes of the ***H*** are 4332x20, 4812x20, 5292x20, and 5772x20. There are 361, 401, 441, and 481 strips for 900 mm, 1000 mm, 1100 mm, and 1200 mm long CFS members, respectively. At each cross-section, there are 12 keypoints; thus, the row size is equal to the cross-section cut number (361, 401, 441, 481) times 12. The rows represent back-to-back cross-section cuts for each keypoint, whereas the columns correspond to the displacements extracted for the first 20 mode shapes corresponding to each keypoint. The common least squares solution that can be adapted for this type of problem is given in Equation [5]):

$$\min_x \|y - Hx\|_2^2 \xrightarrow{yields} x = (H^T H)^{-1} H^T y \tag{5}$$

For this study, global imperfections are favored, meaning that the weights of the keypoints primarily associated with global imperfections (keypoints located on the web) are increased. For these cases, it is required to minimize the weighted square error, i.e., $\sum_n w_n r_n^2$ where r is the residual, or error, $r = y - Hx$, and w_n are positive weights**.** This corresponds to minimizing $\left\|W^{1/2}(y - Hx)\right\|_2^2$ where W is the diagonal matrix, $[W]_{n,n} = w_n$. Using Equation [5] leads to Equation [6]:

$$\min_x \left\|W^{1/2}(y - Hx)\right\|_2^2 \xrightarrow{yields} x = (H^T W H)^{-1} H^T W y \tag{6}$$

Figure 7 presents sample MSB coefficient extraction results for the imperfection distribution shown in Figure 6(a). The mode shapes shown in Figure 6(b) are used for this extraction.

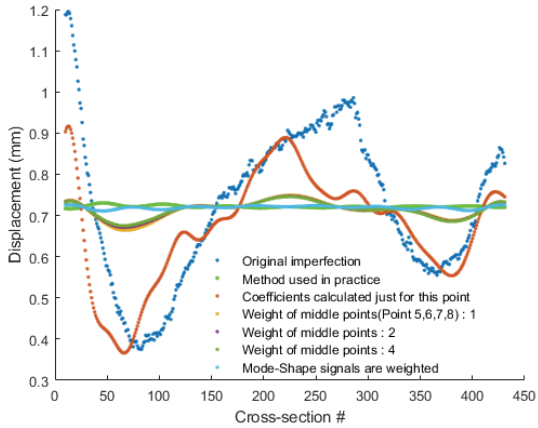

Figure 7 - Sample result for MSB coefficient extraction for C-90-1100-NH-1: Original imperfection, 0.1t multiplication, result with coefficients calculated just for the investigated point, and different weighted coefficient results are displayed.

4.3. Finite Element Analysis

GMNIA is then performed to investigate the effects of MSB geometric imperfection coefficients on member behavior. The determined MSB coefficients are introduced to the model by multiplying these coefficients with corresponding mode shapes obtained from the eigen-buckling analysis, comparable to the approach adopted for the traditional method of geometric imperfection modeling. For this study, the arc-length method (Riks) is chosen for GMNIA. After an eigenvalue buckling analysis, GMNIA is often performed to provide complete information about a structure's collapse [32]. Figure 8 shows the final deformed shape of C-90-1100-NH-1 as a result of GMNIA.

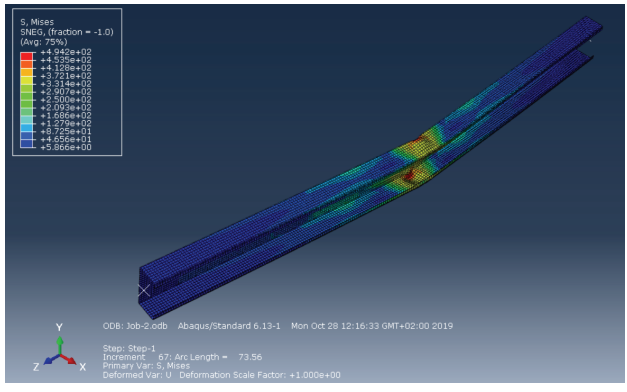

Figure 8 - Final deformed shape result of the GMNIA performed on C-90-1100-NH-1.

5. AXIAL LOADING TESTS OF CFS MEMBERS

Axial loading tests are then performed on the 3D-scanned C-sectioned CFS members. In this section, the utilized test setup and the testing procedure are presented.

5.1. Test Setup

A test setup is specifically designed and built for axial loading of cold-formed steel members. This test device comprises bottom and top steel frames connected by four steel bars, each 50 mm in diameter. The upper frame is formed by connecting two 1950 mm long IPE330 profiles using IPE330 profiles at three locations, at two ends and in the middle. The lower frame is constructed by connecting two 3000 mm long IPE330 profiles at 5 locations. The connections are performed at the ends, in the middle, and close to the locations where the 50 mm diameter bars pass. As the upper frame is mobile, CFS columns with varying lengths were tested (900 – 1200 mm). Further detail on the test setup and related schematics could be found in Guldur Erkal and Cagrici [25].

5.2. Testing Procedure

The described testing frame is capable of applying uniaxial loads up to 30 tons. A hydraulic cylinder (Enerpac RR7513) is attached to the upper frame for axial column tests. Beneath the hydraulic cylinder, a load cell (Esit HSC-V) with a 60-ton capacity is mounted.

The column test setup is equipped with a series of Kyowa DTH 10 mm, 30 mm, and 50 mm linear variable displacement transducers (LVDT) to record the displacements of the specimen throughout the experiments. However, only the average results obtained from three LVDTs (one 10 mm and two 30 mm) attached to the top plate are utilized. During the tests, both the eccentricity between the centerline of the specimens and the load axis, as well as the lateral stability, were actively monitored and effectively addressed.

All 16 CFS members are individually tested. As a sample, the pre- and post-test images of C-90-1000-NH-2 are presented in Figure 9a-b. There are three LVDTs attached to the top plate (loading plate). The top plate LVDT results vs. load cell readings are plotted for C-90-1000-NH-2 in Figure 9c.

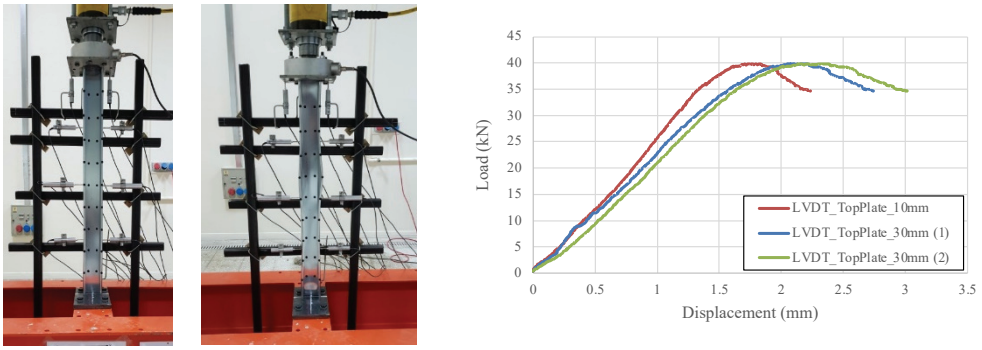

(a) (b) (c)

Figure 9 - Images taken before (a) and (b) after the axial loading test for C-90-1000-NH-2 and the top plate LVDT recordings vs. load plot.

6. RESULTS AND DISCUSSIONS

This section focuses on the results and discussions related to the previous sections. First, to verify the suitability of the collected point clouds for automated geometric imperfection detection and quantification, the point cloud resolutions are displayed. Hand measurements are used to validate the accuracy of the gathered point clouds' dimensions.

The mode shape-based imperfection coefficients of one CFS member are then given. The changes in the imperfection representations caused by different geometric imperfection coefficients are discussed. Finally, the effects of the determined coefficients on CFS member behavior are discussed.

In this study, a desktop suite with an Intel(R) Xeon CPU E5-1650 v3 @ 3.50GHz processor, 48GB RAM, 64-bit operating system, and NVIDIA Quadro K22 graphics card is used to generate the algorithms, run the developed algorithms, and conduct finite element analysis. Finite element analyses are completed by using ABAQUS. All the algorithm development and testing are carried out in MatLab [33] release 2019a. The processing times display variability depending on the length of the member. The average processing time for an individual CFS member, including pre-processing and geometric imperfection extraction, is 300 seconds. Mode-shape-based coefficient extraction is completed in 15 seconds for all 16 C-sectioned CFS members. Last, finite element analysis, including eigen-buckling and GMNIA, takes 15 minutes for each CFS member.

6.1. Point Cloud Resolution

Previous studies have revealed that point cloud precision depends on factors such as point cloud density, registration precision, and angle of incidence [34-37]. A detailed resolution study is performed on all investigated CFS members' point clouds by examining the density of each point cloud. The results showed that the gathered point clouds' resolutions change between 0.018 and 0.033 mm. The average resolution for all members is 0.025 mm. Thus, the collected point clouds are expected to detect geometric imperfections larger than the average resolution value.

In Guldur Erkal and Cagrici [25], the minimum values for local, distortional, and global imperfections collected from previous studies and the related standards computed for 900 – 1200 mm are presented. The obtained resolution values are then compared with the reported minimum values of geometric imperfections in the literature. This comparison demonstrates that the point cloud resolutions are sufficient for geometric imperfection detection and quantification. The captured resolutions are much smaller than the published minimum imperfection values.

6.2. Point Cloud Validation

The measured dimensions of the investigated CFS members are then compared with the dimensions detected by performing point cloud processing. In Guldur Erkal and Cagrici [25], both micrometer-measured and automatically detected dimensions of the CFS members are reported. The comparison between the measured and detected dimensions is also performed to compute the errors.

For both web and flanges of all 16 CFS members, the computed error values are under 2%. The mean error is 1.15% and 1.63% for the web and flanges, respectively, whereas the standard deviations are 0.49% and 0.38% for the web and flanges. The conducted validation investigation confirmed that the gathered point clouds accurately depict the as-is geometry of the actual condition of the investigated CFS members.

6.3. Mode Shape-based Geometric Imperfection Coefficient Extraction Results

In Section 4, the details of the developed mode shape-based geometric imperfection coefficient extraction are presented. Table 1 shows the mode shape-based geometric imperfection coefficients for C-90-900-H-2 given as an example for the first 20 modes. The second column of the table shows the coefficients for which all the keypoints have the same importance and weight in overdetermined equations. The third column shows the coefficients computed where the keypoints on the web, five, six, seven, and eight, receive a weight of two (Figure 5). A weight of four is used for the web keypoints to calculate the coefficients in the fourth column. The coefficients in the fifth column are computed as follows: the coefficients in the first column (no weight case) are multiplied with decreasing values such as 1.0, 0.5, 0.25, and this goes on until the 20th mode.

Table 1 - Mode shape-based geometric imperfection coefficients for C-90-900-H-2 are given for the first 20 modes.

Mode Shape #	No Weight	Middle Points Weight =2	Middle Points Weight =4	Weighted
1	-0.308	-0.299	-0.292	-0.308
2	-0.049	-0.052	-0.052	-0.025
3	0.122	0.152	0.176	0.031
4	0.030	0.024	0.017	0.004
5	0.051	0.045	0.040	0.003
6	-0.049	-0.044	-0.039	-0.002
7	-0.046	-0.039	-0.032	-0.001
8	0.168	0.186	0.201	0.001
9	-0.077	-0.075	-0.071	0.000
10	0.041	0.010	-0.016	0.000
11	0.027	0.045	0.058	0.000
12	0.026	0.029	0.030	0.000
13	0.068	0.063	0.055	0.000
14	-0.060	-0.047	-0.042	0.000
15	-0.080	-0.068	-0.059	0.000
16	-0.085	-0.129	-0.164	0.000
17	0.479	0.490	0.505	0.000
18	-0.016	-0.015	-0.014	0.000
19	0.346	0.390	0.425	0.000
20	0.059	0.045	0.031	0.000

The reconstructed geometric imperfections for 12 keypoints of C-90-900-H-2 with varying MSB coefficients are given in Figure 10. The original imperfections are obtained from the point clouds by performing automated geometric imperfection extraction, plotted with blue dots in each figure. The imperfections reconstructed using the 0.1t multiplication method are labeled 'Method used in practice.' Red dots give the coefficients specifically computed for the investigated keypoint (Case 1). Thus, they represent the closest result to the original imperfection distribution for a selected keypoint. The rest of the plots are reconstructed using the coefficients that account for the entire set of 12 keypoints. These plots represent the cases: no weight (or the weight for each keypoint is one) (Case 2), the weights of middle keypoints (5-8, located on the web) equal to 2 (Case 3), the weights of middle keypoints (5-8, situated on the web) equal to 4 (Case 4), and finally, the coefficients for the mode shapes are multiplied with decreasing values (Case 5) as mentioned before. The keypoint labels are shown in Figure 5.

As seen in Figure 10, the reconstructed imperfection plots obtained by using the method in practice fail to represent the original imperfection in all keypoints. This trend can be observed for the other investigated CFS members as well. Therefore, the GMNIA results obtained using the traditional method generally cannot be considered to represent the actual results for the as-is geometric imperfections on a CFS member. The method in practice is presented with bright green dots in Figure 10.

It should be noted that the reconstruction works better for the point located on the flanges (1-2 and 11-12). However, as the keypoints get closer to the web, the reconstructions fail even for the investigated keypoint (Case 1), i.e., Figure 10e-h. Regardless of the keypoint location, the worst results are obtained either by the method in practice or in Case 5. These two approaches almost always fail to represent the original imperfection distribution. Cases 2, 3, and 4 generally result in similar reconstructions. It could be concluded that changing the weights of web keypoints does not significantly affect the final reconstructed representation, especially in the absence of mode shapes representing global buckling modes. It should be noted that the accuracy of the generated mode shape-based imperfection coefficient extraction method improves with an increasing number of varying mode shape representations. Therefore, other mode shapes could be included in the analysis to enhance generated signal quality and coefficient extraction, or the effect of global buckling modes should be forced into the coefficient extraction process.

Table 2 lists the squared error values for the method in practice and Cases 1-5, along with the total signal energy computed for each CFS member. The total signal energy is computed by summing the squares of the geometric imperfection distributions extracted from the point clouds. It can be seen from the table that the closest result to the original imperfection is always obtained with Case 1, as the computed squared error values are always the lowest. However, Case 1 only represents one location on the cross-section. It does not represent the entire set of 12 keypoints. Thus, Case 1 is not considered in GMNIA. The second-best results are obtained for Case 2, for which the entire collection of keypoints is considered. Case 2-4 give worse results than Case 1, and Case 5 is very similar to the method in practice. Thus, in the GMNIA, only the method in practice and Case 2 are investigated and compared.

Table 2 - Squared error values for method in practice and Cases 1-5.

Specimen	Total Signal Energy	Total Squared Error for Method in Practice	Total Squared Error for Single Point Coef. (Case 1)	Total Squared Error for No Weight (Case 2)	Total Squared Error for Middle Points Weight=2 (Case 3)	Total Squared Error for Middle Points Weight=4 (Case 4)	Total Squared Error for Weighted Coefficients (Case 5)
C-90-900-NH-1	636.40	644.74	549.27	595.83	596.07	596.45	627.15
C-90-900-NH-2	610.23	616.40	527.67	570.05	570.12	570.25	603.84
C-90-900-H-1	774.80	785.24	494.73	680.38	687.58	705.88	754.10
C-90-900-H-2	665.76	676.64	393.32	496.93	498.32	501.64	644.03
C-90-1000-NH-1	1148.17	1155.66	971.42	1081.25	1081.30	1081.36	1130.26
C-90-1000-NH-2	1886.18	1894.71	1671.82	1792.13	1792.32	1792.59	1860.56
C-90-1000-H-1	1133.45	1140.10	844.53	1079.20	1080.57	1083.65	1114.76
C-90-1000-H-2	1716.80	1725.09	1210.94	1638.93	1641.11	1646.18	1690.58
C-90-1100-NH-1	715.35	724.14	643.15	693.95	694.14	694.39	710.71
C-90-1100-NH-2	655.77	662.91	589.16	640.48	640.58	640.71	653.18
C-90-1100-H-1	627.18	632.22	412.38	581.04	583.60	589.44	622.80
C-90-1100-H-2	572.91	576.18	343.78	526.87	531.75	543.07	571.19
C-90-1200-H-1	487.71	492.32	342.25	465.37	467.68	472.75	484.75
C-90-1200-H-2	654.28	659.10	464.95	628.18	630.58	635.84	650.91
C-90-1200-NH-1	828.01	834.85	746.27	819.70	819.81	819.97	825.92
C-90-1200-NH-2	824.58	832.63	755.89	812.54	812.63	812.75	821.26

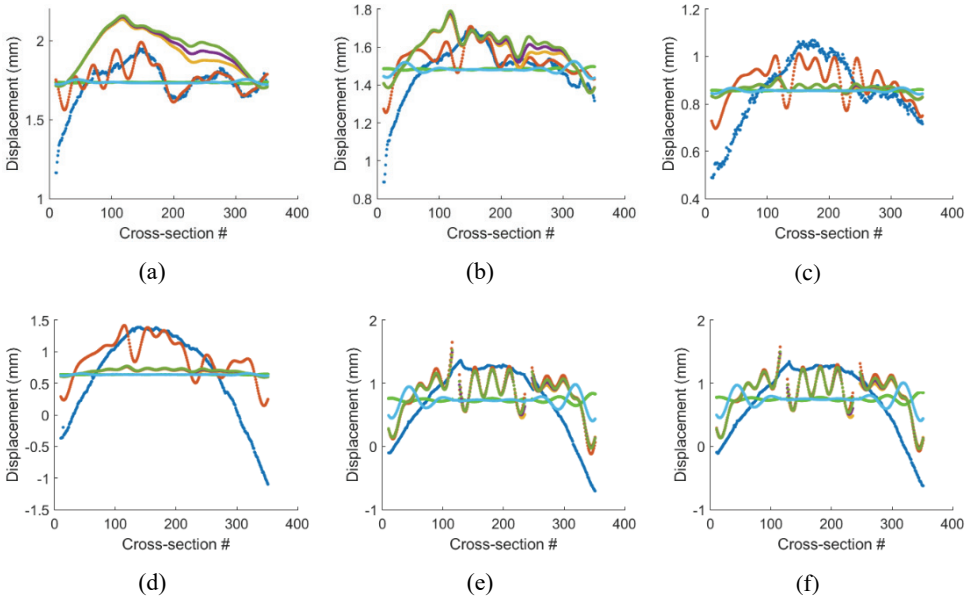

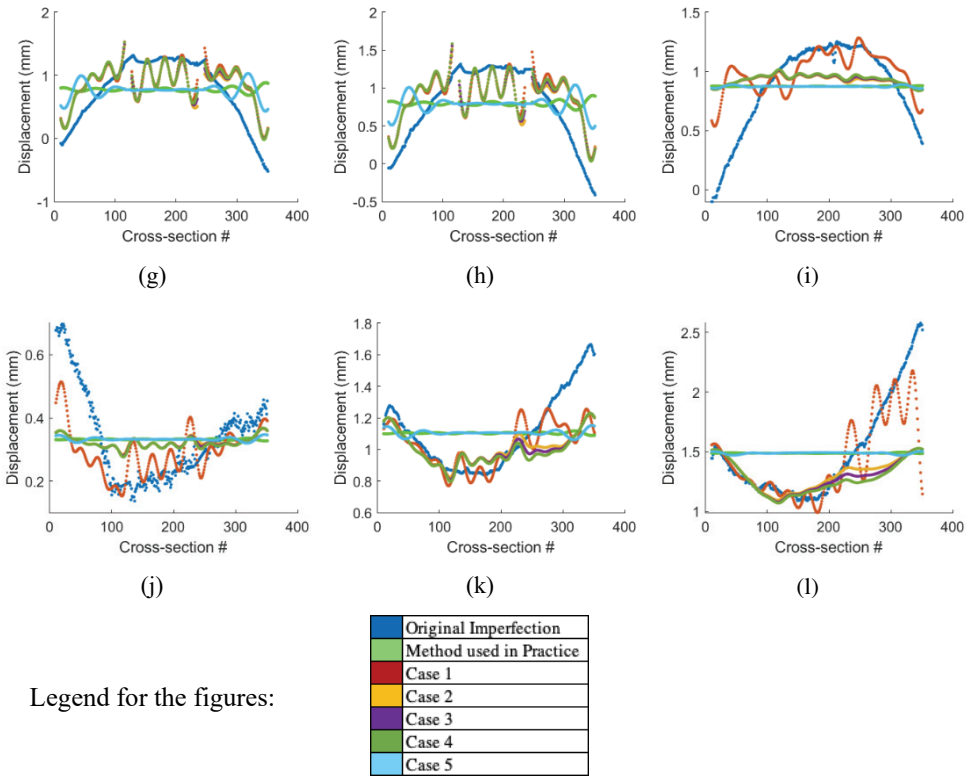

Figure 10 - Reconstructed geometric imperfections for 12 keypoints of C-90-900-H-2 with varying MSB coefficients.

6.3.1. Results of GMNIA with Varying MSB Coefficients

This section displays the GMNIA results for all the investigated CFS members. Analyses are terminated when the displacement capacities obtained during the experiment are obtained. The top displacement vs. load curves obtained from nonlinear analysis for mode shape-based geometric imperfection coefficients, 0.1t coefficient, and collected test data are given in Figure 11 for all investigated CFS members. The test data for comparing the numerical results are obtained by averaging the data from the three LVDTs attached to the top plate.

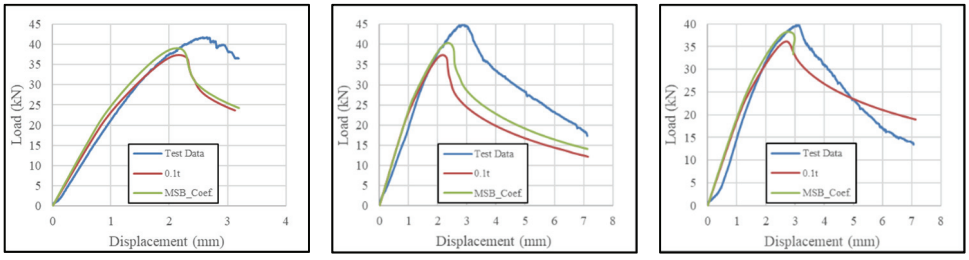

(a) C-90-900-NH-1 (b) C-90-900-NH-2 (c) C-90-900-H-1

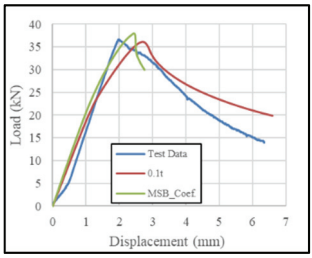

(d) C-90-900-H-2

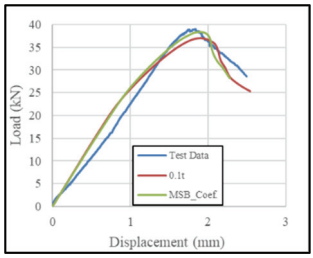

(e) C-90-1000-NH-1

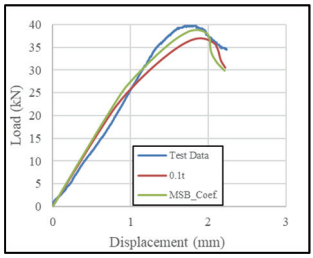

(f) C-90-1000-NH-2

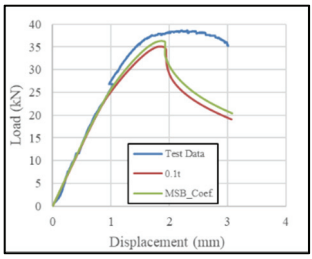

(g) C-90-1000-H-1

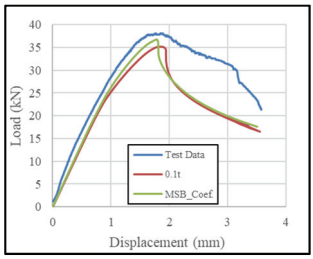

(h) C-90-1000-H-2

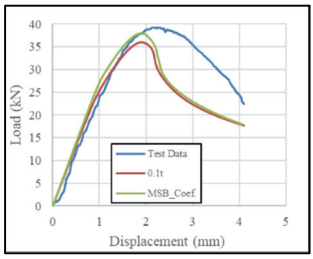

(i) C-90-1100-NH-1

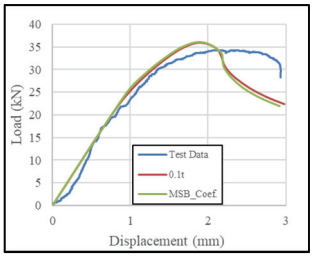

(j) C-90-1100-NH-2

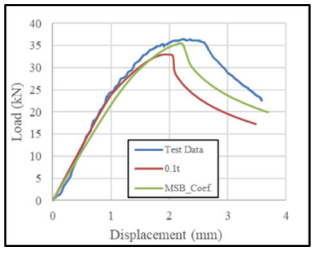

(k) C-90-1100-H-1

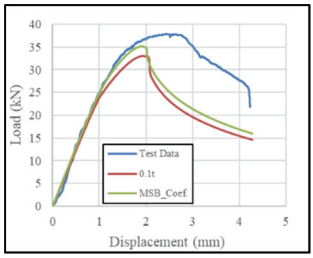

(l) C-90-1100-H-2

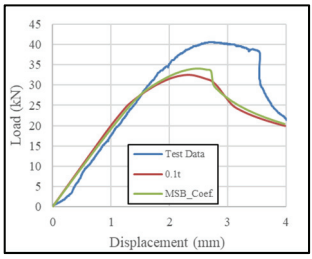

(m) C-90-1200-H-1

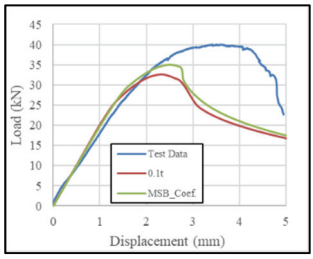

(n) C-90-1200-H-2

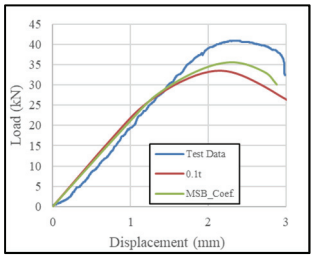

(o) C-90-1200-NH-1

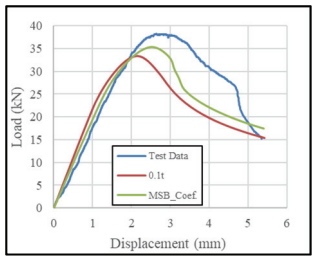

(p) C-90-1200-NH-1

Figure 11 - Top displacement vs. load curves obtained for all investigated CFS members for various cases.

The GMNIA results showed that the method in practice generally underestimates the capacity of the investigated CFS members. The GMNIAs performed with the imperfection distributions obtained by reconstruction mode shapes provide closer results to CFS members' actual behavior. However, the results obtained with the MSB coefficients also underestimate the member capacity, and at the same time, this method sometimes underestimates the displacement capacities.

Table 3 presents the initial slope and energy results obtained from GMNIAs for 0.1t and MSB coefficients and experiment results. The errors are computed by comparing the MSB coefficient results with the experiment results. The errors calculated for the initial slopes are mostly less than 10%, which indicates that the GMNIA results are in good accordance with the experiments. However, the average error for the energy, which represents the area under the top displacement vs. load curves, is approximately 18%. The lowest computed value is 1.45%, and the highest value of nearly 57%. Even though the total displacement capacity obtained from the GMNIAs matches the experiment results, in most of the GMNIAs, there is a significant capacity loss after the ultimate load capacity is reached. Therefore, the energy values computed for the GMNIA results for the same total displacement capacity as experiments are always lower than the values obtained for experiment results.

AISI-S100 is later used to calculate yielding, flexural buckling, torsional buckling, flexural torsional buckling, local buckling, and distortional buckling capacities. The test results are then compared with the GMNIA results, and the design capacities are computed with AISI-S100. The ultimate load capacities computed for local buckling are critical for all CFS members. Table 4 reports the ultimate load capacity of the investigated members recorded in experiments, computed with AISI-S100 (local buckling), obtained from GMNIA with 0.1t coefficient and GMNIA with MSB coefficients. The experiment results are higher than the axial load capacities computed via AISI-S100. It is observed that the results obtained from GMNIA with a 0.1t coefficient are on the safe side. The GMNIA results with a 0.1t coefficient give lower ultimate load capacities than the experiment results but closer to the axial load capacities computed via AISI-S100. Finally, the GMNIA results with MSB coefficients are higher than the axial load capacities calculated via AISI-S100 but more comparable to the experiment results.

7. CONCLUSIONS

In this work, a numerical and experimental study was conducted to examine the impact of geometric imperfections on the behavior of cold-formed steel (CFS) members. Point clouds representing the real geometry of 16 CFS members were collected using a 3D optical scanner. The results showed that these point clouds effectively represented the geometric imperfections in the members. These imperfections varied significantly across different members, indicating that a constant value for local imperfections would not accurately represent individual member conditions.

Geometric imperfections were integrated into finite element models using MSB coefficients to perform GMNIA. Mode shapes obtained from eigen-buckling analysis were used to reconstruct imperfection distributions in the finite element model. However, it was found that reconstructing the actual deformed shape of a CFS member using mode shapes was not possible. If only a single keypoint on each cross-section was considered, reconstructed imperfection distributions could be used.

To validate the GMNIA results, axial loading tests were conducted on the investigated CFS members. The buckling load, axial and lateral displacements, and material properties were monitored and recorded during the tests. The experimental results were used to validate the numerical models.

The GMNIA results using varying geometric imperfection coefficients showed that the method in practice was over-conservative. Models generated with MSB coefficients provided slightly better representation of member behavior but were still conservative. The study concluded that improving the representation of geometric imperfections or boundary conditions could enhance the accuracy of finite element model results.

It should be noted that while the method in practice is conservative and easy to implement, it is important to evaluate alternative approaches for optimal design and utilization of CFS frames, especially in seismic regions. Addressing overdesign and accurately simulating geometric imperfections is crucial. The development of an easy-to-use methodology for extracting imperfections and advancements in high-resolution 3D scanning offer opportunities to enhance the proposed method for more accurate results in the future. This will improve overall performance assessment and maximize the benefits of CFS structures in construction.

In future studies, it is recommended to focus on keypoint coefficients for individual keypoints as they provide the best representation of imperfection distribution. Additionally, exploring the integration of global modes into the coefficient extraction process could be valuable. However, assigning suitable weights to global modes poses a challenge as they are forcibly extracted. Further research is needed to address these aspects and enhance the analysis accuracy.

Acknowledgments

This material is based upon work supported by the Scientific and Technological Research Council of Turkey (TUBITAK) under Grant No. 217M513 and Hacettepe University.

Table 3 - Initial slope and energy results for GMNIA results for 0.1t and MSB coefficients and experiment results and the associated errors.

	Initial Slope (kN/mm)			Initial Slope	Energy (kN.mm)			Energy
Specimen	**Exp.**	**0.1t Coef.**	**MSB Coef.**	**Error (%)**	**Exp.**	**0.1t Coef.**	**MSB Coef.**	**Error (%)**
C-90-900-NH-1	21.35	20.58	22.70	6.32	87.89	76.58	82.13	-6.55
C-90-900-NH-2	20.08	20.58	21.32	6.18	199.46	144.44	160.93	-19.32
C-90-900-H-1	17.30	16.49	17.60	1.74	165.12	168.81	71.08	-56.95
C-90-900-H-2	19.03	16.49	19.09	0.27	139.60	158.18	65.06	-53.40
C-90-1000-NH-1	22.24	24.49	25.15	13.10	60.36	62.92	56.30	-6.73
C-90-1000-NH-2	25.11	24.49	26.64	6.10	56.65	54.11	55.82	-1.45
C-90-1000-H-1	28.00	25.52	25.85	-7.69	86.34	68.94	71.97	-16.64
C-90-1000-H-2	27.04	25.52	26.47	-2.08	100.36	74.37	79.10	-21.19
C-90-1100-NH-1	24.97	24.04	26.08	4.45	114.82	94.45	97.85	-14.78
C-90-1100-NH-2	25.21	25.65	26.13	3.62	73.66	72.45	70.85	-3.82
C-90-1100-H-1	25.73	23.49	21.51	-16.39	92.65	74.86	84.35	-8.96
C-90-1100-H-2	26.53	23.49	24.87	-6.25	119.48	87.50	93.50	-21.75
C-90-1200-H-1	18.77	19.03	18.95	0.95	107.47	90.10	90.96	-15.37
C-90-1200-H-2	17.04	19.03	19.15	12.39	144.83	108.89	113.62	-21.55
C-90-1200-NH-1	20.47	21.08	21.05	2.86	77.76	71.03	69.98	-10.00
C-90-1200-NH-2	17.32	21.46	19.17	10.71	138.68	118.02	124.81	-10.00

Table 4 - Axial load capacities of the investigated members recorded in experiments, computed with AISI-S100, obtained from GMNIA with 0.1t imperfection, and GMNIA with MSB coefficients.

Specimen	Experimental		AISI Design Strength		GMNIA + Method in Practice (0.1t)		GMNIA + Reconstruction with MSB Coef.	
	P_{Exp} (kN)	Failure mode	P_{AISI} (kN)	Fail. mode	P_{MiP} (kN)	Failure mode	P_{MSBC} (kN)	Failure mode
C-90-900-NH-1	41.78	Local + Distortional Buck.	38.98	Local Buck.	37.35	Local Buck.	39.06	Local Buck.
C-90-900-NH-2	45.05	Local Buck.	38.98	Local Buck.	37.35	Local Buck.	40.37	Local Buck.
C-90-900-H-1	39.79	Local Buckling at Hole	38.98	Local Buck.	36.10	Local Buckling at Hole	38.27	Local Buckling at Hole
C-90-900-H-2	36.66	Local Buckling at Hole	38.98	Local Buck.	36.10	Local Buckling at Hole	37.80	Local Buckling at Hole
C-90-1000-NH-1	38.94	Local + Distortional Buck.	36.77	Local Buck.	36.98	Local Buck.	38.32	Local Buck.
C-90-1000-NH-2	39.79	Local + Distortional Buck.	36.77	Local Buck.	36.98	Local Buck.	38.84	Local Buck.
C-90-1000-H-1	38.65	Local Buck.	36.77	Local Buck.	35.11	Local Buckling at Hole	36.33	Local Buckling at Hole
C-90-1000-H-2	38.08	Local + Distortional Buck.	36.77	Local Buck.	35.11	Local Buckling at Hole	36.61	Local Buckling at Hole
C-90-1100-NH-1	39.22	Local Buck.	34.46	Local Buck.	36.01	Local Buck.	37.90	Local Buck.
C-90-1100-NH-2	34.25	Local Buck.	34.46	Local Buck.	36.01	Local Buck.	36.11	Local Buck.
C-90-1100-H-1	36.52	Local Buckling at Hole	34.46	Local Buck.	33.08	Local Buckling at Hole	35.38	Local Buckling at Hole
C-90-1100-H-2	37.94	Local Buckling at Hole	34.46	Local Buck.	33.08	Local Buckling at Hole	35.17	Local Buckling at Hole
C-90-1200-H-1	40.64	Local Buckling at Hole	32.11	Local Buck.	32.56	Local Buckling at Hole	34.05	Local Buckling at Hole
C-90-1200-H-2	40.07	Local Buckling at Hole	32.11	Local Buck.	32.56	Local Buckling at Hole	34.97	Local Buckling at Hole
C-90-1200-NH-1	40.92	Local Buck.	32.11	Local Buck.	33.45	Local Buck.	35.59	Local Buck.
C-90-1200-NH-2	38.22	Local Buck.	32.11	Local Buck.	33.45	Local Buck.	35.37	Local Buck.

References

[1] Peterman KD. Experiments on the stability of sheathed cold-formed steel studs under axial load and bending. Baltimore, MD, USA: John's Hopkins University; 2012.

[2] McAnallen L, Padilla-Llano D, Zhao X, Moen C, Schafer B, Eatherton M. Initial geometric imperfection measurement and characterization of cold-formed steel C-section structural members with 3D non-contact measurement techniques. Proceedings of the Structural Stability Research Council. Toronto, Canada2014.

[3] Zhao X, Tootkaboni M, Schafer B. Development of a laser-based geometric imperfection measurement platform with application to cold-formed steel construction. Experimental Mechanics. 2015;55:1779-90.

[4] Salomon AL, Fratamico D, Schafer BW, Moen CD. Full field cold-formed steel column buckling measurements with high resolution image-based reconstruction. Proceedings of the Annual Stability Conference Structural Stability Research Council. Orlando, FL, USA2016.

[5] Zhao X, Tootkaboni MP, Schafer BW. High fidelity imperfection measurements and characterization for cold-formed steel members. Proceedings of the 7th International Conference on Coupled Instabilities in Metal Structures. Baltimore, MD, USA2016.

[6] Zhao X, Tootkaboni M, Schafer BW. Laser-based cross-section measurement of cold-formed steel members: model reconstruction and application. Thin-Walled Structures. 2017;120:70-80.

[7] Selvaraj S, Madhavan M. Geometric imperfection measurements and validations on cold-formed steel channels using 3D noncontact laser scanner. Journal of Structural Engineering. 2018;144.

[8] Dubina D, Ungureanu V. Effect of imperfections on numerical simulation of instability behaviour of cold-formed steel members. Thin-Walled Structures. 2002;40:239-62.

[9] Bonada J, Casafont M, Roure F, Pastor M. Selection of the Initial Geometrical Imperfection in Nonlinear FE Analysis of Cold-formed Steel Rack Columns. Thin-walled Structures. 2012;51:99-111.

[10] Zeinoddini V, Schafer B. Simulation of geometric imperfections in cold-formed steel members using spectral representation approach. Thin-Walled Structures. 2012;60:105-17.

[11] Garifullin M, Nackenhorst U. Computational Analysis of Cold-formed Steel Columns with Initial Imperfections. Procedia Engineering. 2015;117:1073-9.

[12] Gendy BL, Hanna M. Effect of Geometric Imperfections on the Ultimate Moment Capacity of Cold-Formed Sigma-Shape Sections. HBRC Journal. 2017;13:163-70.

[13] Sadovský Z, Kriváček J, Ivančo V, Ďuricová A. Computational modelling of geometric imperfections and buckling strength of cold-formed steel. Journal of Constructional Steel Research. 2012;78:1-7.

[14] Zeinoddini V, Schafer BW. Global imperfections and dimensional variations in cold-formed steel members. International Journal of Structural Stability and Dynamics. 2011;11:829-54.

[15] Martins AD, Dinis PB, Camotim D. On the Influence of Local-Distortional Interaction in the Behaviour and Design of Cold-Formed Steel Web-Stiffened Lipped Channel Columns. Thin-Walled Structures. 2016;101:181-204.

[16] Li Z. Stochastically simulated mode interactions of thin-walled cold-formed steel members using modal identification. Thin-Walled Structures. 2018;128:171-83.

[17] ABAQUS/CAE. ABAQUS Users' Guide 2019. Dassault Systemes: Paris, France: Dassault Systemes; 2019.

[18] Ye J, Hajirasouliha I, Becque J. Experimental investigation of local-flexural interactive buckling of cold-formed steel channel columns. Thin-walled structures. 2018;125:245-58.

[19] dos Santos ES, Batista EM, Camotim D. Experimental investigation concerning lipped channel columns undergoing local–distortional–global buckling mode interaction. Thin-Walled Structures. 2012;54:19-34.

[20] Dinis PB, Camotim D, Silvestre N. FEM-based analysis of the local-plate/distortional mode interaction in cold-formed steel lipped channel columns. Computers & Structures. 2007;85:1461-74.

[21] Camotim D, Dinis PB. Coupled instabilities with distortional buckling in cold-formed steel lipped channel columns. Thin-Walled Structures. 2011;49:562-75.

[22] Chou S, Chai G, Ling L. Finite element technique for design of stub columns. Thin-walled structures. 2000;37:97-112.

[23] Moen CD, Schafer B. Elastic buckling of thin plates with holes in compression or bending. Thin-Walled Structures. 2009;47:1597-607.

[24] HEXAGON. SmartScan. 2022.

[25] Guldur Erkal B, Cagrici OG. Automated Geometric Imperfection Detection and Quantification of CFS Members from Point Clouds. KSCE Journal of Civil Engineering. 2022.

[26] Eurocode 3 - Part 1-3. Eurocode 3: Design of Steel Structures, Part 1-3 - Design of Cold-Formed Steel Structures: ECCS Eurocode Design Manuals; 2012.

[27] Koiter WT. On the stability of elastic equilibrium: National Aeronautics and Space Administration; 1967.

[28] Schafer BW, Li Z, Moen CD. Computational modeling of cold-formed steel. Thin-Walled Structures. 2010;48:752-62.

[29] Schafer B, Peköz T. Computational modeling of cold-formed steel: Characterizing geometric imperfections and residual stresses. Journal of Constructional Steel Research. 1998;47:193-210.

[30] Gendy BL, Hanna MT. Effect of geometric imperfections on the ultimate moment capacity of cold-formed sigma-shape sections. HBRC Journal. 2019;13:163-70.

[31] ASTM-E8/E8M. Standard Test Methods for Tension Testing of Metallic Materials. West Conshohocken, PA.: ASTM International; 2013.

[32] Simulia D. ABAQUS 6.11 analysis user's manual. Abaqus. 2011;6:22.2.

[33] MatLab. MATLAB and Statistics Toolbox Release 2019a. Natick, MA, USA: The MathWorks, Inc.; 2019.

[34] Kashani AG, Olsen MJ, Parrish CE, Wilson N. A review of LiDAR radiometric processing: From ad hoc intensity correction to rigorous radiometric calibration. Sensors. 2015;15:28099-128.

[35] Laefer DF, Gannon J, Deely E. Reliability of crack detection methods for baseline condition assessments. Journal of Infrastructure Systems. 2010;16:129-37.

[36] Laefer DF, Truong-Hong L, Carr H, Singh M. Crack detection limits in unit based masonry with terrestrial laser scanning. Ndt & E International. 2014;62:66-76.

[37] Olsen MJ, Kuester F, Chang BJ, Hutchinson TC. Terrestrial laser scanning-based structural damage assessment. Journal of Computing in Civil Engineering. 2010;24:264-72.

Turkish Journal of Civil Engineering, 2023, 53-79, Yazı 751, ***Araştırma Makalesi***

Sönmüş Kireç-Diatomit-SBS Katkılarıyla Geri Dönüştürülmüş Asfalt Kaplamaların Performans Analizi

Burak KORZAY[1]
Atakan AKSOY[2*]
Mehmet Emre TEKİN[3]

ÖZ

Geri dönüştürülmüş asfalt kaplamalar (RAP); ekonomik ve çevresel üstünlüklere sahiptir. Sera gazı emisyonlarını ve bitüm gereksinimini azaltması, tamamen dönüşebilir olması, atık depolamayı azaltması, hammadde kaynaklarını koruması, kullanım çeşitliliği yönleriyle avantajlıdır. Sürdürülebilirlik yaklaşımlarıyla, artan oranda aşınma tabakalarında kullanılmaktadır. Bu hedeflerle, Türkiye için, saha çalışmalarına yönelik %50 RAP ile aşınma tabakası dizaynları üretilmiştir. Katkı olarak; SBS ile yaygın kullanım oranlarının çok daha düşük değerlerinde uyumlaştırıcı sönmüş kireç (HL) ve diatomit (D) kullanılmıştır. Çalışmada, HL ve D ile RAP karışımların su hasarı ve tekerlek izi bakımından garantili iyileştirilmesi hedeflenmiştir. Diatomit kullanımı; gerek Türkiye gerekse dünya için yenilikçi bir konudur. Sabit HL-SBS içeriğinde, D%5-10 oranları ayrı ayrı kullanıldı. AASHTO T283 Modifiye Lottman ve Hamburg tekerlek izi testleri uygulandı. %50RAP eklenmiş karışımlar, seçilen katkılar ile orijinal karışımlardan daha dirençli hale gelmiştir. Modifiye Lottman testinin D, HL, SBS ve RAP'lı karışımlar için ayırt edici olduğu ve performans artışını yansıttığı görülmektedir. Sabit ve az HL oranında, D oranının %5'den %10 değerine artırılması ile su hasarı direncinin artması, HL ve D'nin birlikte performans artışı oluşturabildiğini gösterdi. HL+SBS uyumu; daha yüksek su hasarı direnci oluşturmaktadır. SBS, gerek HL gerekse de D ile uyumlu çalışmaktadır. Düşük HL- D oranlarında ve yaygın oranda %5SBS kullanımı; %50RAP karışımlarda su hasarı direnci bakımından çok yüksek iyileşme sağlamaktadır. Tüm %50RAP modifiye karışımların kontrol karışımlardan daha

Not: Bu yazı
- Yayın Kurulu'na 8 Kasım 2022 günü ulaşmıştır. 1 Eylül 2023 günü yayımlanmak üzere kabul edilmiştir.
- 31 Ocak 2024 gününe kadar tartışmaya açıktır.

• https://doi.org/10.18400/tjce.1363595

1 İstanbul Büyükşehir Belediyesi, İSFALT A.Ş., İstanbul, Türkiye
burak.korzay@isfalt.istanbul - https://orcid.org/0000-0001-8401-2153

2 Karadeniz Teknik Üniversitesi, İnşaat Mühendisliği Bölümü, Trabzon, Türkiye
aaksoy@ktu.edu.tr - https://orcid.org/0000-0001-5232-6465

3 İstanbul Büyükşehir Belediyesi, İSFALT A.Ş., İstanbul, Türkiye
etekin@isfalt.istanbul - https://orcid.org/0000-0003-1582-4232

* Sorumlu yazar

yüksek tekerlek izi direnci vermesi bu karışımların uygulamada başarıyla kullanılabileceğini göstermektedir.

Anahtar Kelimeler: Asfalt kaplamalar, geri dönüştürülmüş asfalt kaplama, diatomit, sönmüş kireç, SBS polimer, su hasarı, tekerlek izi, Hamburg tekerlek izi deneyi.

ABSTRACT

Performance Analysis of Recycled Asphalt Pavements with Hydrated Lime-Diatomite-SBS Additives

Reclaimed asphalt pavements (RAP); has economic and environmental advantages. It is advantageous in terms of reducing greenhouse gas emissions and bitumen requirement, being completely recyclable, reducing waste storage, protecting raw material resources, and diversity of use. With sustainability approaches, it is increasingly used in wear layers. With these objectives, wearing layer designs with 50% RAP for field studies were produced for Turkey. As an additive materials; compatibilizer hydrated lime (HL) and diatomite (D) were used at much lower values than the common usage rates with SBS. It was aimed to obtain guaranteed improvement of RAP mixtures with HL and D in terms of water damage and rutting. Using of diatomite is one of the innovative issues for both Turkey and the world. 5-10% ratios of D were used separately for the constant HL-SBS content. AASHTO T283 Modified Lottman and Hamburg rutting tests were performed. Mixtures with 50%RAP added became more resistant than the original mixtures with the selected additives. It is seen that the modified Lottman test is distinctive for mixtures with D, HL, SBS and RAP and reflects the performances successfully. Increased water damage resistance at a constant low HL ratio with the increasing the D ratio from 5% to 10% indicate that HL and D together can produce performance improvement. HL+SBS compliance provides higher water damage resistance. SBS works in harmony with both HL and D. Low HL-D rates and widespread use of 5%SBS provides very high improvement in water damage resistance in mixtures with 50%RAP. The fact that all 50%RAP modified mixtures gave higher rutting resistance than control mixtures shows that these mixtures can be used successfully in practice.

Keywords: Asphalt pavements, recycled asphalt pavement, diatomite, hydrated lime, SBS polymer, water damage, rutting, Hamburg test.

GİRİŞ

Endüstri, RAP kalitesini iyileştirmek ve asfalt karışımlarda daha yüksek oranda kullanmak için sürekli farklı yollar aramaktadır. Amerika'da, şu anda, eski asfalt kaplamalardan kazınan RAP'ın yeni kaplamalarda kullanım oranı %99'dur. Üreticilerin; ortalama RAP yüzdeleri olarak %20 veya daha fazla kullanım bildirdiği eyaletlerin sayısı önemli ölçüde artmıştır. 2009'da on eyaletten 2017'de 24 eyalete yükselmiştir ancak ortalama RAP yüzdesi hala %20-35 civarındadır [1]. RAP karışımının %95'inden fazlasının yeni kaplamalarda ve kalan %5'in temel tabakaları gibi diğer alanlarda kullanılmasıyla, asfalt karışımı üreticileri, ülkenin en gayretli geri dönüştürücüleri olmaktadır. Asfalt karışımlarında kullanılan toplam tahmini RAP miktarı 2021'de 94,6 milyon tondu. Bu, 2009'da kullanılan tahmini RAP tonajından %68,9'luk bir artışı temsil etmektedir. 2009'dan bu yana toplam asfalt karışımı tonajı yalnızca %20,6 arttı. RAP kullandığını bildiren üreticilerin yüzdesi, 2020'ye göre %1,1 artışla yanıt

verenlerin %100'ü oldu. İki üretici, 2021'de RAP'ın küçük bir miktarını (36.000 ton veya %0,07) düzenli depolamaya tabi tuttuklarını bildirdi [2]. Son araştırmalar, mekanik özelliklerde tatmin edici sonuçlar elde ederek, yeni karışım tasarımlarına %50'nin üzerindeki oranlarda RAP ikamesinin yeni karışımları üretmek için uygun olduğunu göstermektedir [3-4]. %100 RAP'ın, malzeme döngüsünü kapatarak gerçek sürdürülebilirliği sağlayacağı ve geleneksel asfaltla aynı yüksek değerli uygulamada kullanılmasına imkan olacağı savunulmaktadır [5]. Yeniden kullanılan RAP yüzdesi, dünyanın birçok ülkesinde kademeli artmaktadır. Ağırlıkça %15–%20 aralığında bir RAP bitümlü karışımların üretimi için standart uygulama haline gelmektedir. Yüksek (ağırlıkça %40'ın üzerinde) veya çok yüksek (ağırlıkça %100'e kadar) RAP'lı bitümlü karışımlar üretmenin fizibilitesi incelenmektedir. RAP kullanımını; ağırlıkça %15-30'luk ortalama RAP içeriğinin ötesine geçecek şekilde sınırlayan olumsuz algılar ve pratik sorunlar vardır. Bunlar; HMA (sıcak karışım asfalt) karışımlarında RAP agregalarının kalitesi, üretim plent tesisinin teknolojisi, karışım tasarım metodolojisi ve RAP içeren nihai karışımın performansı olarak özetlenebilir [6]. ABD ve Avrupa'daki ortak uygulamalar, esas olarak yeni HMA /WMA (ılık karışım asfalt) karışımlarına eklenen RAP miktarı ve bağlanmamış katmanlar için agrega olarak kullanılan miktar açısından farklılık gösterir. Bu nedenle, Tablo 1'de listelenen yüzdeler, Avrupa Devletlerinin geri dönüştürülmüş agrega potansiyelinden daha çok yararlanabileceğini vurgulamaktadır [7-8].

Tablo 1 - ABD ve Avrupa'da RAP kullanımının karşılaştırılması [7-8]

Değerlendirilen Miktarlar	Amerika	Avrupa
Toplam HMA ve WMA üretimi	389.300.000 Ton	297.900.000 Ton
Plent tesislerinde kabul edilen toplam RAP	101.100.000 Ton	49.500.000 Ton
Sıcak Karışım Asfalt/Ilık asfalt karışımlarında kullanılan RAP	%81,3	%51,4
Soğuk Asfalt karışımlarında kullanılan RAP	%0,297	%3,81
Bağlanmamış tabakalar için agrega olarak kullanılan RAP	%6,33	%17
Başka amaçlar için kullanılan RAP	%1,98	%2
RAP dolgu	%0	%9.63

2011 yılında FHWA (The Federal Highway Administration), karışımın toplam ağırlığına göre %25'ten fazla RAP içeren asfalt betonlarını yüksek içerikli RAP olarak tanımlamıştır [9]. Sürdürülebilirlik analizi; %30, %40 ve %50 RAP içeren karışımları hazırlamak için tüketilen enerjinin sırasıyla %26, 33 ve %40 azaldığını ortaya koymaktadır [10]. HMA karışımlarına %30 ve %40 RAP eklenmesinin inşaat, bakım, rehabilitasyon ve malzeme ikamesi değerleri dikkate alındığında sırasıyla %19 ve %40 maliyet tasarrufu sağladığını dile getirilmektedir [11]. %25 RAP dahil edilmesi sırasıyla enerji tüketiminde, eşdeğer CO_2 emisyonunda ve maliyette %33, 35 ve %8,5 azalmaya neden olmaktadır [12]. Yüksek RAP oranı, RAP'ın yaşlanmış bağlayıcısı nedeniyle nihai karışımların yorulma ve termal çatlama direncini önemli ölçüde azaltmaktadır [13-14].

HMA plentlerinin kurutucusunda aleve maruz kalan RAP agregalarının doğrudan ısıtılması sonucunda RAP bağlayıcının daha fazla yaşlanması ve sertleşmesi nedeniyle, yüksek RAP içeren karışımların mekanik özellikleri etkilenmektedir [15-17]. RAP içeriği esas olarak üretim kalitesi ve dolayısıyla asfalt plentindeki karışımların performansı gibi pratik konularla sınırlıdır. RAP malzemeleri yüksek sıcaklıklarda yaşlanır ve yüksek oranda kullanılması potansiyel olarak yolların erken çatlamasına neden olabilir. Diğer bir neden ise, öğütme işlemi nedeniyle agregaların ezilmesi sonucu çok miktarda ince partikül oluşmasıdır. Bu daha ince parçacıklar, yüksek RAP içeriğinde karışım tasarımı için derecelendirme gereksinimlerini sınırladığı için RAP kullanımının maksimum içeriğini sınırlar. Tesisler RAP'ın daha yüksek oranına izin vermemektedir, çünkü batch plentlerde tipik RAP katma aralığı %10-20'dir ve drum plentler %50'ye kadar uyum sağlayabilir [18].

Artan yaşlanma bağlayıcının gerilme gevşeme kapasitesini azaltmakta, bu da karışımın çatlama direncini azaltmaktadır [19]. RAP, işlenmemiş malzeme tüketimini; ilişkili maliyet ve enerjiyi azaltır. Ayrıca, RAP dökümü için gerekli olan değerli depolama alanlarından tasarruf edilebilmektedir. RAP malzemesinin orijinal özelliklerini eski haline getirmek için bazı gençleştiriciler katılmalıdır. Gençleştirici ile oluşan asıl mekanizma çok iyi bilinmemektedir. RAP karışımlarının performansının öngörülemez olmasını sağlayabilir ve dolayısıyla RAP içeriğinin arttırılmasında bir kısıtlama oluşturur. RAP malzeme kalitesi için herhangi bir uygun karakterizasyon yönteminin olmaması ve saf ve RAP bağlayıcının harmanlanması hakkında çok az bilgi sahibi olunması da; RAP karışımın performansı hakkında öngörülemez olmanın ve dolayısıyla daha yüksek RAP içeriği kullanma konusunda ihtiyatlı olmanın başlıca nedenidir [20]. Yüksek RAP içeriğine sahip kesimlerin esas olarak daha düşük sürüş kalitesi, daha fazla çatlama ve daha iyi tekerlek izi direnci gösterme eğiliminde olduğu, ancak farklılıkların her zaman istatistiksel olarak anlamlı olmadığı belirtilmektedir [21]. Yüksek oranda RAP eklenmesinin, üstyapı performansından ödün vermeden kullanılabileceği belirtilmektedir [22].

EN13108'e göre karışım prosedürünün güvenilirliği araştırıldı. Özellikle, aşınma tabakası RAP bileşenlerinin dozajlanması ve RAP bağlayıcı içinde bulunan bağlayıcının ve ex-novo eklenen bağlayıcının Performans Derecesi ve kritik sıcaklıklarının belirlenmesi için SuPerPave® tasarım yönergeleri uygulandı. RAP yüzdesi olarak %30, %40 ve %50 oranları kullanıldı. Sonuçlar, uygulanan rasyonel karışım tasarımının, Avrupa standartlarıyla tamamen uyumlu olarak aşınma tabakası geri dönüştürülmüş karışımların performans seviyelerini garanti ettiğini gösterdi [23]. Değişen belirli karışım tasarım parametrelerinin (agrega ve filler yapısı, bağlayıcı içeriği ve türü) %20 RAP malzemesi içeren karışımların mekanik özellikleri üzerindeki etkisi kalitatif değerlendirilmiştir. Analiz sonuçları, bağlayıcı yapısındaki ve bağlayıcı içeriğindeki değişikliklerin, karışımların kompleks modülü üzerinde istatistiksel olarak önemli ~~bir~~ etkiye sahip olduğunu göstermiştir. RAP malzeme içeriğinin ve yeni eklenen bağlayıcı penetrasyon derecesinin, karışımların kompleks modülü ve yorulma ömrü üzerindeki etkisi nicel olarak tahmin edilmiştir. %60'a kadar RAP malzemesi içeren karışımların gözlenen yorulma ve kompleks modül performansları teknik, ekonomik ve çevresel açıdan oldukça cesaret vericidir [24].

NAPA anketi, hemen hemen tüm asfalt fabrikalarının ürünlerinde RAP kullandığını ifade etmektedir. (HMA)/(WMA~~)~~ kullanılan toplam RAP miktarı arttı. Asfalt karışımlarında kullanılan ulusal ortalama RAP yüzdesi 2009'da %15,6'dan 2016'da %20,5'e istikrarlı bir şekilde yükseldi ve buna karşılık gelen RAP kullanımından elde edilen yıllık tasarruf 2 milyar

dolardan fazla oldu. AB Üyesi 28 ülke için 2016 yılında üretilen 226,8 milyon ton asfalt malzemesinin yaklaşık %17'si mevcut RAP malzemelerine karşılık gelmektedir [16]. Termal üretim koşullarının mekanizmaları ve bunların RAP karışımlarının performansı üzerindeki etkileri iyi anlaşılmamıştır. Üretim koşulları ile RAP karışımlarının performansı arasındaki korelasyonların deneysel kanıtları da laboratuvarda üretilen ve plentte üretilen RAP karışımlarına dayalı olarak gözden geçirilmiştir. Deneysel çalışmalar, karıştırma süresi, karışım boşaltma sıcaklığı ve silo depolama süresi gibi üretim parametrelerinin RAP karışımlarının performansı üzerindeki önemini vurgulamıştır. Yerel asfalt fabrikalarında kullanılan en iyi üretim uygulamalarını belirlemek için RAP karışımlarının saha performansı bakımından; tesis tipi, ham agrega sıcaklığı, RAP giriş sıcaklığı, RAP nem içeriği, karışım tahliye sıcaklığı, silo depolama sıcaklığı ve süresi, taşıma süresi ve teslimat sıcaklığı dahil olmak üzere RAP karışımlarının üretim koşullarının kaydedilmesi ve ardından takip edilmesi şiddetle tavsiye edilir. Daha kısa bir silo depolama süresi, ham ve RAP bağlayıcılar arasında eksik bir karışıma neden olabileceğinden ve daha uzun bir silo depolama süresi, bağlayıcıların aşırı oksitlenmesine neden olabileceğinden, RAP karışımları için silo depolama süresine özel dikkat gösterilmelidir. Yüksek oranda RAP karışımlarında daha yumuşak bir orijinal bağlayıcı tercih edilmelidir [16].

SBS kopolimer modifiye asfalt, temel olarak kalıcı deformasyon, düşük sıcaklıkta çatlama, yorulma, soyulma, aşınma direnci ve yaşlanmayı önlemeyi iyileştirmek amacıyla geliştirilmiştir. SBS modifiye karışımlarda sorgulanmaktadır. Geri kazanılmış SBS modifiye asfalt karışımları, SBS'nin varlığı nedeniyle geri kazanılmış asfalt bağlayıcılardan farklıdır [25-27]. RAP ve gençleştirici katkının performans üzerine etkileri incelenmiştir. Geri kazanılmış SBS modifiye asfalt kaplamayı içeren asfalt karışımlara yeni SBS modifiye asfalt bağlayıcı ve gençleştirici maddenin karıştırılmasıyla; daha iyi nem duyarlılığı, tekerlek izi direnci, dinamik modül, düşük sıcaklıkta çatlama önleme performansı ve yorulma direncine sahip karışımlar elde edildiğini görülmüştür. Gençleştirici, RAP içeren daha sürdürülebilir asfalt kaplama hazırlama çabasına fayda sağlayacaktır [28]. Eski SBS modifiye asfalt karışımının geri dönüştürülmesinin, modifiye edilmemiş asfalt karışımı ile aynı geri dönüşüm sürecini takip edip edemeyeceği konusunda çok az literatür vardır. RAP ile (HMA) için tasarım süreci, RAP yüzdesi %25'ten düşük olduğunda orijinal HMA için karışım tasarımına benzer [29-32]. RAP'ın SBS Polimeri İle modifiye edilmiş bağlayıcı içeren karışımlara dahil edilmesinin kırılmaya karşı direnci arttırdığı; yarı dairesel çentikli kırılma testi ile belirlenmiştir. Karışımların yorulma özelliklerini önemli ölçüde değiştirme eğiliminde olan %30'dan fazla RAP'a sahip karışımlarda dikkatli olunmalıdır [33].

Fransa'da, A84 karayolunda, beş yıl sonra elde edilen saha sonuçlarına göre, HL, asfalt katkısı olarak güçlü bir teknik ilgi çekmektedir. HL'li ve HL'siz beş bölüm oluşturuldu ve takip edildi. Karışımlar, %15 RAP içeren yarı yoğun asfalt betonu (Fransız BBSG) idi. Deneysel program, standart ve ileri düzey reolojik ve kimyasal testlere dayalı bağlayıcı değerlendirmesini ve daldırma sonrasında kalan mukavemet, kompleks modül ve yorulma gibi karışım testlerini içeriyordu. Ek olarak, RAP'ın nem direnci üzerindeki olumsuz etkisi vurgulanmış ve HL, performans kaybını en aza indirmek için etkili bir çözüm olarak ortaya çıkmıştır [34].

Asfalta D eklenmesi (DMA), yüksek sıcaklık performansını, depolama stabilitesini, tekerlek izi direncini ve uzun vadeli yaşlanma direncini artırabilir. DMA mastik; kireçtaşı, HL ve uçucu külle modifiye edilenden daha uygun yüksek ve orta sıcaklık performanslarına sahiptir

[35]. Bununla birlikte, DMA, asfalt karışımının ısıl iletkenliğini ve düşük sıcaklıkta deformasyon yeteneğini düşürmek gibi bazı çekinceler sunmaktadır [36]. DMA hazırlanması için direkt ve indirekt yöntemler kullanılabilir. Direkt harmanlama yöntemi kullanıldığında, D mineral tozu olarak asfalt ve agrega karışımına ilave edilir. İndirekt yöntemi kullanıldığında, karışımın hazırlanmasından önce DMA bağlayıcı hazırlanır [37]. DMA karışımların yorulma performansının kontrol karışımlara göre önemli ölçüde iyileşmesi, asfalt ve D arasındaki üstün uyum özelliklerine atfedilmektedir. Bu uyum, karıştırma süresini azaltmakta, DMA yaşlanmasını azaltmakta, doğrudan doğruya asfalt karışımın durabilitesini iyileştirmektedir [38].

Bu araştırmada; RAP malzemesinin yüksek oran olarak kabul edilen %50 katma oranı için katkı seçenekleri bağlamında performansları araştırılmış ve alternatif karışımlar üretilmiştir. %50 RAP İstanbul'da Avrupa yakasından temin edilen Akdağlar Aşınma Tabakası tip dizaynı ile kullanılmıştır. Yaşlanmanın yönetilmesi ve deneme üretimine de geçilecek oluşundan dolayı gerek uygulama gerekse plent koşulları düşünülerek karışımların kalitesinin sürdürülebilir kılınmasında farklı katkı seçenekleri oluşturulmuştur. RAP malzemenin homojenizasyon sorunu olabilmesinden dolayı hem HL hem D katkılı hem de SBS katkılı seçenekler üretilmiştir. Oluşturulmuş geniş kombinasyonda karışım örneklerine su hasarı ve Hamburg tekerlek izi deneyleri gerçekleştirilmiştir. Elde edilen performans düzeyleri geleneksel kontrol ve geleneksel SBS kontrol karışımlar ile kıyaslanmaktadır. D katkısının seçilmesi nedeni Türkiye için henüz yeni bir perspektif olarak silika içeriğinin yüksek oluşu ile yaşlanmanın yönetilmesi ve karışım performansının artırılması olmaktadır. Önemli oran olarak %50RAP uygulamasını başarılı kılarak ekonomik kazanımlar elde etme ve orijinal karışımlara benzer performansların sorgulanması noktasında; HL, D ve SBS formülasyonları farklı seçeneklerde kullanılmıştır. D %5 ve %10 oranları olarak literal uyumla birlikte 2 farklı oran seçeneğinde kullanılmıştır. Belirlenen katkı seçeneklerinin literatürde belirtilen yaygın kullanım oranlarına göre oldukça düşük düzeyde seçilen bu katkıların oluşturabileceği birlikte çalışma konusu sorgulanmaktadır. Yüksek RAP oranları için oluşturulan karışımlar SBS katkısının da varlığında ayrıca irdelenmektedir. Çok yoğun bir deneysel araştırma çerçevesi ile elde edilen sonuçlar laboratuvar testleri anlamında sorgulanmaktadır ve literal olarak irdelenmektedir.

MALZEME VE YÖNTEM

Bu araştırmada; agrega, bitüm, diatomit, HL, SBS polimer malzemeleri ve araziden temin edilen RAP malzemesi kullanılmıştır. Elek analizi tane boyutu dağılım verileri Tablo 2'de; kaba agrega fiziksel özellikleri Tablo 3'de, ince agrega fiziksel özellikleri ise Tablo 4'de verilmektedir. RAP gradasyonu Tablo 2'de verilmektedir ve bitüm yüzdesi de %3,85 olarak ekstraksiyon deneyinden hesaplanmıştır.

Tablo 5 bitüm özelliklerini vermektedir. Dizaynda, (12–19), (5–12) ve (0 –5) mm dane boyutu agregalar ve B50/70 bitüm kullanılmıştır. Gradasyonun hazırlanmasında, Tablo 6'da ki elek ortalamaları alındı. Gradasyon eğrisi Şekil 1'de sunulmaktadır. İSFALT AŞ Fabrikası'ndan Akdağlar Taş Ocağı'ndan alınarak laboratuvara teslim edilen Kumtaşı agregalarla "Asphalt Institute MS-2 Marshall Metoduna göre 2x75 darbeyle 135-140°C'de sıkıştırılan numunelerle Aşınma Tip 1 dizaynı sonucunda, optimum bitüm; kuru agregaya göre ağırlıkça %5,3±0,2 (100g kuru agrega + 5,3gr B50/70 bitüm) olarak bulunmuştur.

Optimum bitüm hesabında Marshall grafiklerinden faydalanılmış, %4 boşluk değerine karşılık gelen bitüm değeri alınmıştır. Dizayn sonuçları Tablo 7'de verilmektedir.

Tablo 2 - Tane boyutu dağılımı (Deney metodu-ASTM C136 /117)

Elek No (inç)	Elek No (mm)	12-19 mm	5-12 mm	0-5 mm	RAP
3/4"	19	100,0	100,0		100
1/2"	12,5	15,6	97,1		100
3/8"	9,5	4,9	73,3	100,0	99,4
No 4	4,75	3,9	15,4	98,4	83,4
No 10	2,0	3,9	5,2	61,3	53,4
No 40	0,425	3,9	5,0	24,4	25,1
No 80	0,180	3,9	4,4	12,5	18
No 200	0,075	2,0	3,0	5,6	12

Tablo 3 - Kaba agrega fiziksel özellikleri

Deney Adı	Metot	Birim	Sonuç	Limit
Los Angeles Aşınma	TS EN 1097-2	%	17	Maks. 27
Yassılık İndeksi, 5-12 mm	TS EN 933-3	%	13	Maks. 20
Yassılık İndeksi, 12-19 mm	TS EN 933-3	%	11	Maks 20
Soyulma Mukavemeti	TS EN 12697-11	%	70	Min. 60
Kil ve Ufalanabilir Taneler	ASTM C142	%	0	Maks.0,3
Kuru Tane Yoğunluğu	TS EN 1097-6	Mg/m^3	2,72	-
Görünür Tane Yoğunluğu	TS EN 1097-6	Mg/m^3	2,77	-
Doygun Kuru Yoğunluğu	TS EN 1097-6	Mg/m^3	2,74	-
Su Absorbsiyonu	TS EN 1097-6	%	0,8	Max. 2,0

Tablo 4 - İnce agrega fiziksel özellikleri

Deney Adı	Deney Metodu	Birim	Sonuç	KTŞ 2013
Plastisite İndeksi	TS 1900-1	%	NP	NP
Metilen Mavisi	TS EN 933-9+A1	MB	1,3	Max.1,5
Kurutulmuş Tane Yoğunluğu	TS EN 1097-6	Mg/m^3	2,66	-
Görünür Tane Yoğunluğu	TS EN 1097-6	Mg/m^3	2,79	-
Doygun Kuru Yoğunluk	TS EN 1097-6	Mg/m^3	2,71	-
Su Absorbsiyonu	TS EN 1097-6	%	1,7	Max. 2,0
Filler Tane Yoğunluğu	TS EN 1097-7	Mg/m^3	2,75	-

Tablo 5 - Bitümlü bağlayıcı özellikleri (B50/70)

Deney Adı	Metot	Birim	Sonuç	Şartname
Penetrasyon 25°C	TS EN 1426	0,01mm	60	50-70
Özgül Ağırlık d25/25	TS EN 15326 +A1	-	1,014	-
Yoğunluk 25°C		Kg/m^3	1011	-
Yumuşama Noktası	TS EN 1427	°C	50	46-54
Parlama Noktası	TS EN ISO 2592	°C	306	Min.230
Çözünürlük	TS EN 12592	%	100	Min.99

Tablo 6 - Agrega kullanım oranları ve karışım gradasyon eğrisi

Oran		5%	52%	43%	Karışım Grad.	KTŞ 2013 Aşınma-Tip 1 Alt-Üst Sınırlar		İşyeri Karışım Formülü	
ELEK AÇIKLIK (Inch)	(mm)	12-19 mm	5-12 mm	0-5 mm					
¾”	19,0	5,0	52,0	43,0	100,0	100,0		100,0	
½”	12,5	0,8	50,5	43,0	94,3	88,0	100,0	90,0	98,0
3/8”	9,5	0,2	38,1	43,0	81,4	72,0	90,0	77,0	85,0
No 4	4,75	0,2	8,0	42,3	50,5	42,0	52,0	47,0	52,0
No 10	2,00	0,2	2,7	26,4	29,3	25,0	35,0	26,0	32,0
No 40	0,425	0,2	2,6	10,5	13,3	10,0	20,0	10,0	16,0
No 80	0,180	0,2	2,3	5,4	7,9	7,0	14,0	7,0	11,0
No 200	0,075	0,1	1,6	2,4	4,1	3,0	8,0	3,0	6,0
Agrega Karışımının Efektif Özgül Ağırlığı (G_{ef}): 2,736 gr/cm^3 Agrega Karışımının Hacim Özgül Ağırlığı (G_{sb}): 2,692 gr/cm^3									

İşyeri Karışım Formulü, laboratuvar dizaynına göre plentin ayarlanmasından sonra, üretilen karışımın fiziksel özelliklerinin ve sıkışma kontrolüne esas yoğunluğun tayinini kapsar. Dizayn, Akdağlar Ocağı’ndan alınarak laboratuvara teslim edilen agregalarla hazırlanan, Aşınma Tip 1 karışımı içindir ve plentin çalışmasına esastır. SBS polimer kullanılmıştır. HL, S-KK-80-T türünde sönmüş kalker kirecidir. SBS Kraton-1192, %5 oranında 50/70 Penetrasyon bitüme katıldı. Modifiye bitüm, 3000 rpm yüksek kesmeli karıştırıcıda 4 saat süreyle 180 °C'de hazırlandı. Bentaş Bentonit firmasından temin edilen ve D_2 kodlu diatomit kullanılmıştır. D XRF ana oksit sonuçları, Tablo 8’de ve granülometrisi de de Şekil 2’de verildi. Diatomit, bitümün %5-%10 oranlarında kullanılmıştır. HL, kuru karışımın %0.5 oranındadır. Diatomit ve HL kuru karışıma katılmıştır. D_2 diatomit katkısının XRD analizi Şekil 3’de; SEM görüntüsü Şekil 4’de verilmektedir.

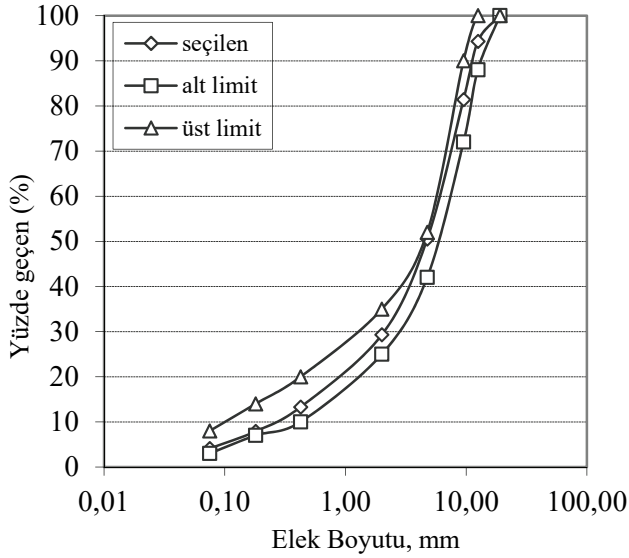

Şekil 1 - Kullanılan Karışım Gradasyon Eğrisi

Tablo 7 - Dizayn kriterleri

	Sonuç	Şartname
Bitüm % 'si (ağırlıkça,100'e)	5,3 ± 0,2	4,0 -7,0
Pratik Özgül Ağırlık, gr/cm3 (Mg/m^3)	2,422	
Marshall Stabilitesi, kg	1200	Min.900
Akma, mm	3,8	2- 4
Filler / Bitüm Oranı	0,8	Maks. 1,5
Boşluk, %	4,0	3- 5
Asfaltla (bitüm) dolu boşluk, %	73,0	65- 75
Agregalar arası boşluk (VMA), %	14,6	14- 16

Tablo 8 - Diatomit katkısı ana oksit analiz sonuçları

	SiO_2	Al_2O_3	Fe_2O_3	MgO	CaO	Na_2O	K_2O	TiO_2	P_2O_5	MnO
Birim	%	%	%	%	%	%	%	%	PPM	%
D2	74,099	8,437	2,839	3,049	1,852	0,109	1,002	0,46	0,139	0,054
	SO_3	Cl	BaO	CuO	NiO	SrO	V_2O_5	ZnO	ZrO_2	
Birim	%	PPM	%	%	%	%	%	%	%	
D2	0,016	83	0,017	0,319	ND	0,029	0,077	ND	0,018	

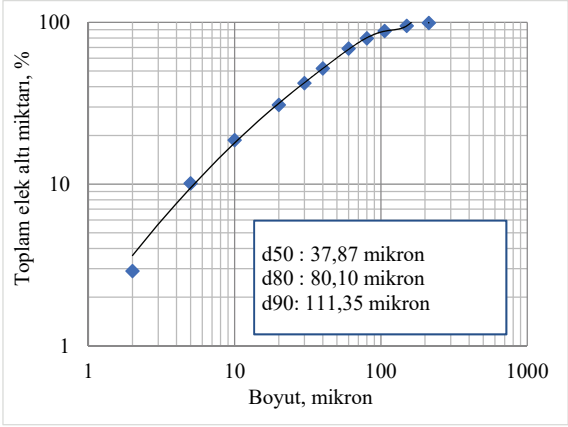

Şekil 2 - D_2 kodlu diatomit granülometri eğrisi

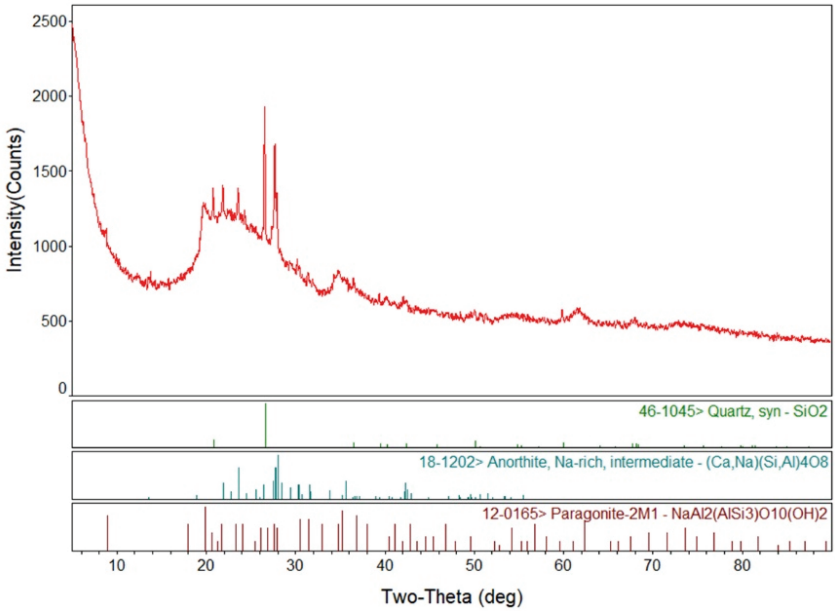

Şekil 3 - D_2 kodlu numunenin XRD analizi

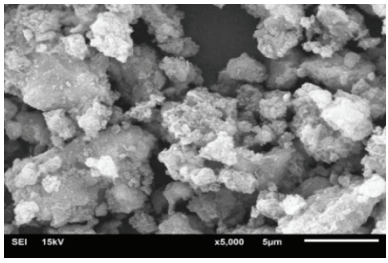

Şekil 4 - D_2 SEM görüntüsü

Modifiye Lottman Su Hasarı Testi (AASTHO T 283)

Asfalt kaplamalarda en yaygın sorunlardan biri, esas olarak bağlayıcı kütlesi içindeki kohezyonun azalması veya agregalar ile asfalt bağlayıcı arasındaki adezyonun azalması nedeniyle oluşan su hasarıdır [39]. Asfalt karışımlarının nem duyarlılığını değerlendirmek için Modifiye Lottman testi (AASHTO T283) uygulanmaktadır. Yaygın olarak kabul edilmektedir ve asfalt karışımların suya karşı duyarlılığı için en doğru testlerden biridir [40].

Kullanılan numuneler koşulsuz ve koşullu numuneler olarak iki kısma ayrılmıştır. Koşullu gruptaki numuneler, vakumlu piknometre ile %70 ile %80 arasında su ile doygun hale getirildi. Daha sonra bir plastik film ile kaplandı ve 10 ml su içeren plastik torbaya yerleştirildi. Plastik içindeki numuneler, 20 saat boyunca -18°C'de donmuş halde tutuldu. Dondurma işlemini tamamlayan numuneler 60°C su banyosunda 24 saat bekletilmiştir. Su banyosundan sonra plastik torba ve film çıkartılarak koşullandırma işlemi tamamlanmıştır. Koşullu ve koşulsuz gruplardaki numuneler 2 saat 25°C'de su banyosuna yerleştirildikten sonra dolaylı çekme dayanımı (ITS) testi yapılmıştır. Test makinesi ve numune boyutları tarafından kaydedilen tepe yükü kullanılarak, çekme mukavemetleri eşitlik ile hesaplanır.

$$\text{Çekme Mukavemeti (psi)} = 2P/\pi tD \quad (1)$$

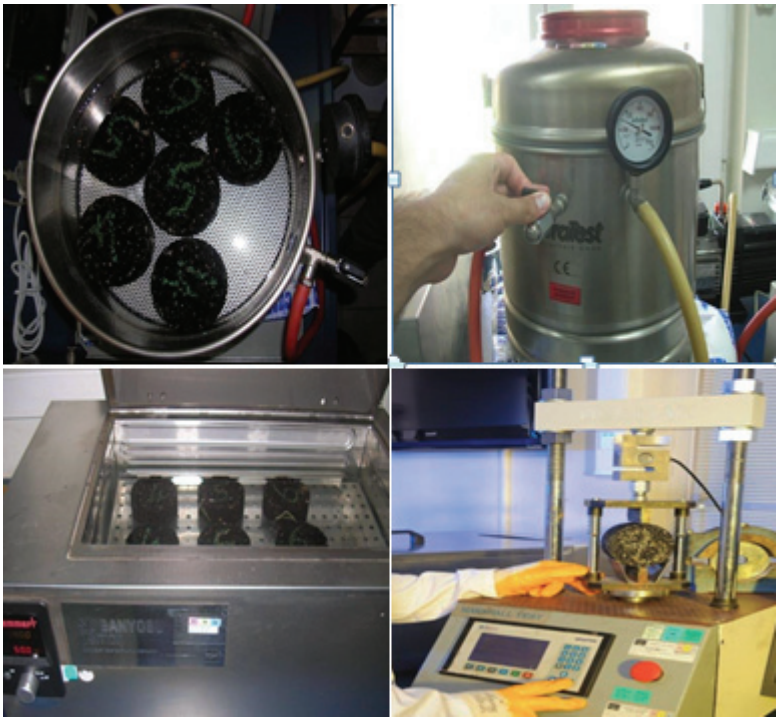

Şekil 5 - Su hasarı deneyi görüntüleri

Çekme mukavemeti (1) bağıntısı ile bulunur. Burada; P Maksimum yük (lbf), t Numune kalınlığı (inç), Numune çapı D (inç) olarak kullanılır. Her briket için çekme mukavemeti hesaplandıktan sonra koşullu numunelerin ortalama çekme mukavemeti, kuru numunelerin ortalama çekme mukavemetine oranı % olarak hesaplanır.

$$ITSR=(ITS_w/ITS_d)x100 \quad (2)$$

Dolaylı çekme mukavemeti oranı için (2) bağıntısı kullanılır. Burada; ITSR yüzde (%) cinsinden dolaylı çekme mukavemeti oranı, ITS_w ıslak grubun psi cinsinden ortalama dolaylı gerilme dayanımı, ITS_d kuru grubun psi cinsinden ortalama dolaylı gerilme değeridir. Deney süreçlerine ait bazı görüntüler, Şekil 5'de verilmektedir.

Oluşturulan karışım kombinasyonları için özdeş briket koşullu/koşulsuz su hasarı oranları Tablo 9-Tablo 16 arasında verilmektedir. Tablo 9-16 tablolarında, %50RC ifadesi %50 oranında RAP katılmış karışım anlamında kullanılmaktadır.

Tablo 9 - Kontrol karışım koşullu/koşulsuz özdeş briket su hasarı oranları

Kontrol Karışım		Koşullu		
		S1	S2	S3
Koşulsuz		137,02	127,51	129,45
S1	163,58	0,8376	0,7795	0,7914
S2	154,4	0,8874	0,8258	0,8384
S3	172,5	0,7943	0,7392	0,7504

Tablo 10 - Koşullu/koşulsuz briketler su hasarı oranları (%50RC%0.5HL)

%50RC %0.5HL		Koşullu		
		S1	S2	S3
Koşulsuz		127,44	141,17	123,03
S1	163,58	0,7791	0,8630	0,7521
S2	154,4	0,8254	0,9143	0,7968
S3	172,5	0,7388	0,8184	0,7132

Tablo 11 - Koşullu/Koşulsuz Briketler Su Hasarı Oranları (%50RC%0.5HL%10D)

%50RC %0.5HL%10D		Koşullu		
		S1	S2	S3
Koşulsuz		141,39	138,06	147,10
S1	163,58	0,8644	0,8440	0,8993
S2	154,4	0,9157	0,8942	0,9527
S3	172,5	0,8197	0,8004	0,8528

Tablo 12 - Koşullu/koşulsuz briketler su hasarı oranları (%50RC%0.5HL%5SBS %5D)

%50RC %0.5HL%5SBS %5D		Koşullu		
		S1	S2	S3
Koşulsuz		162,07	160,00	161,95
S1	163,58	0,9908	0,9781	0,9901
S2	154,4	1,0497	1,0363	1,0489
S3	172,5	0,9396	0,9276	0,9389

Tablo 13 - Koşullu/koşulsuz briketler su hasarı oranları (%5SBS)

%5SBS		Koşullu		
		S1	S2	S3
Koşulsuz		130,20	127,89	128,84
S1	163,58	0,7959	0,7818	0,7876
S2	154,4	0,8432	0,8283	0,8344
S3	172,5	0,7548	0,7414	0,7469

Tablo 14 - Koşullu/koşulsuz briketler su hasarı oranları (%50RC%0.5HL %5D)

%50RC %0.5HL %5D		Koşullu		
		S1	S2	S3
Koşulsuz		122,81	146,18	134,02
S1	163,58	0,7508	0,8937	0,8193
S2	154,4	0,7954	0,9468	0,8680
S3	172,5	0,7120	0,8474	0,7769

Tablo 15 - Koşullu/koşulsuz briketler su hasarı oranları (%50RC%0.5HL%5SBS)

%50RC %0.5HL%5SBS		Koşullu		
		S1	S2	S3
Koşulsuz		150,71	161,22	143,65
S1	163,58	0,9214	0,9856	0,8782
S2	154,4	0,9761	1,0442	0,9304
S3	172,5	0,8737	0,9346	0,8328

Tablo 16 - Koşullu/koşulsuz briketler su hasarı oranları (%50RC%0.5HL%5SBS%10D)

%50RC %0.5HL %5SBS %10D		Koşullu		
		S1	S2	S3
Koşulsuz		147,88	147,99	161,39
S1	163,58	0,9041	0,9047	0,9866
S2	154,4	0,9578	0,9585	1,0453
S3	172,5	0,8573	0,8579	0,9356

Şekil 6 kontrol ve tüm modifiye karışımların ITS değerlerini sunmaktadır. Şekil 7, kontrol ve modifiye karışımların koşulsuz ITS değerlerini vermektedir. Şekil 6 ve Şekil 7 kapsamındaki veriler irdelendiğinde, uygulanan su hasarı koşullandırmasının ITS değerlerini azalttığı belirtilebilir. %50RAP katkılı karışımlarda Şekil 6 ve Şekil 7'da görüldüğü üzere, karışımda ister HL isterse D olsun karışıma SBS girmesi durumunda ITS değerleri yaklaşık %15 düzeyinde artmaktadır. Bu artış, özellikle koşulsuz briketler için çok belirgin olmaktadır. Koşullandırma durumunda ise yine HL ve D birlikte ve ayrı ayrı varlığında, SBS katkısı bireysel briket anlamında ve ortalama değerleri anlamında yine mukavemet artışı oluşturmaktadır.

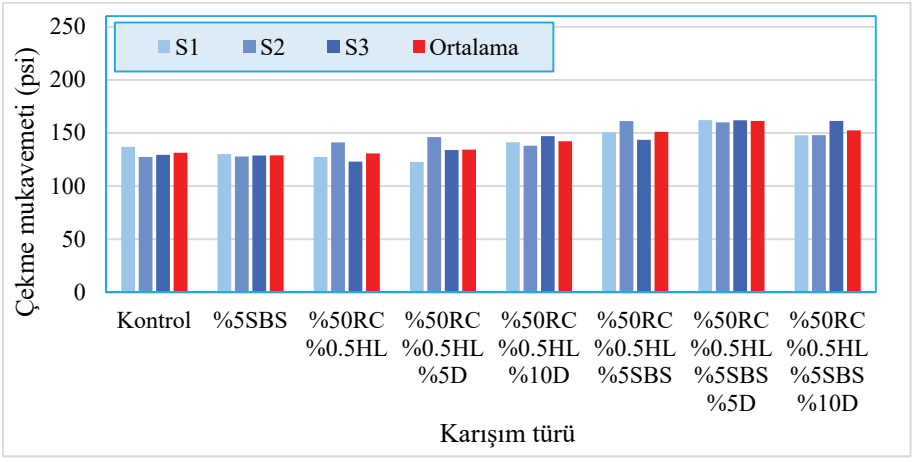

Şekil 6 - Koşullu çekme dayanımı

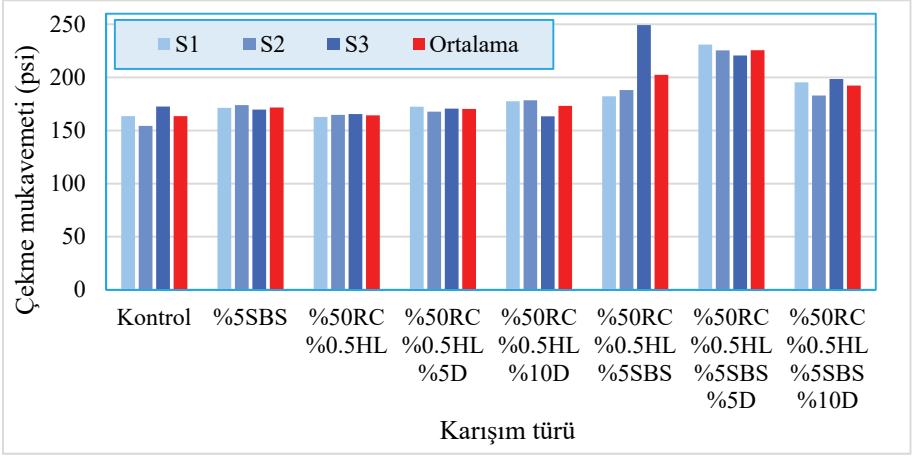

Şekil 7 - Koşulsuz çekme dayanımı

Şekil 8, koşullu ve koşulsuz çekme dayanımlarının ortalamalarını vermektedir. Değerler, kontrol ve katkılı modifiye karışım alternatifleri için, özdeş briketlerin ortalaması olarak sunulmaktadır.

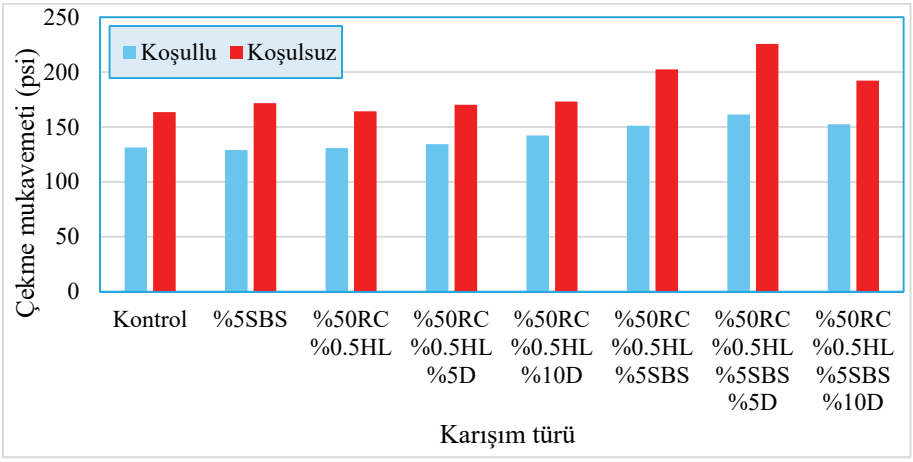

Şekil 8 - Koşullu ve koşulsuz çekme dayanımlarının ortalamaları

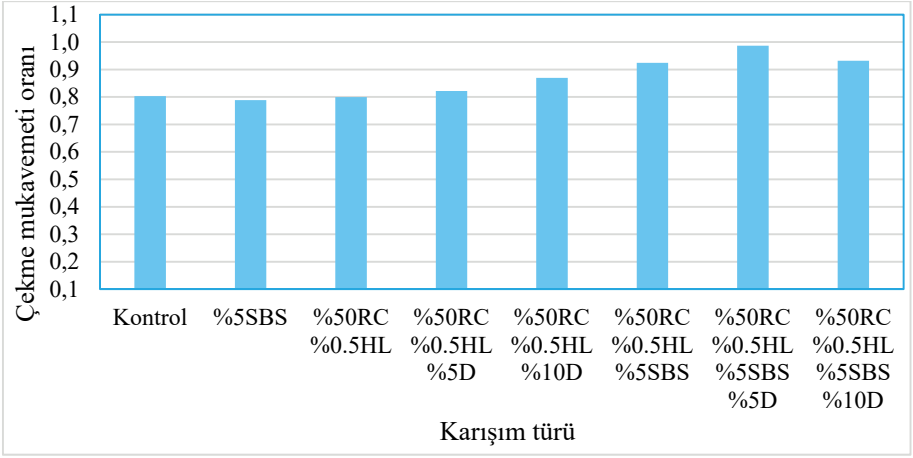

Şekil 9 - Kontrol karışımların ve %50RAP katkılı modifiye karışımların koşullu/kontrol koşulsuz dolaylı çekme mukavemeti oranları

Şekil 9'dan görüldüğü üzere, %50RAP katkılı karışımlarda sadece %0.5HL kullanılması su hasarı direnci bakımından henüz iyileşme sağlayamamıştır. Sadece HL kullanılması durumunda bile, %50RAP karışımlar için kontrol ve SBS katkılı kontrol karışıma benzer sonuç alınmaktadır. Sadece su hasarı değerlendirilirse %50RAP karışımlar için bu oran yaklaşımı değeri yüksektir. Diğer performans problemleri ile karşılaştırma yapılmalıdır.

Tekerlek izi ve özellikle yorulma deneyleri gerçekleştirilmelidir. %5D katıldığında kısmi iyileşme başlamıştır. %10D değerinde ise su hasarı direnci belirgin olarak artmıştır. Düşük HL oranında D oranının %5'den %10 değerine artırılması ile su hasarı direncinin artması, HL ve diatomitin birlikte performans artışı ortaya koyabildiğini göstermektedir.

Şekil 9'da kontrol karışımların ve %50RAP katkılı modifiye karışımların koşullu/kontrol koşulsuz dolaylı çekme mukavemeti oranları verilmektedir. 0.75 oran değeri bir kabul kriteri olarak ele alındığında, kontrol ve %5SBS kontrol karışımları kabul kriteri olarak kabul görmektedir. Dikkati çeken önemli nokta, %50RAP katkılı karışımlarda HL ve D katkısı ile SBS varlığında su hasarı oran değerlerinin %50 RAP seçeneklerinde dahi artmış olmasıdır. Kontrol karışımlara göre, %50RAP katılı karışımların HL-SBS varlığında su hasarı direnci %12 oranında artmaktadır. Bu karışım bünyesinde %5D ilavesi ile kontrol karışımlara göre artış oranı %18,68 olmaktadır. Aynı karışımlarda D oranının %5 değerinden %10 değerine çıkması halinde artış oranı %13 olmaktadır. HL-SBS varlığında, %50RAP katkılı karışımlarda %5D değeri %10D değerine göre daha yüksek su hasarı direnci vermektedir. %50RAP katkılı karışımların su hasarı direncinin orijinal karışımların su hasarı direncinin üzerine çıktığı görülmektedir. HL, su hasarı ve diğer performans yönlerinden önemli üstünlük sağlayan bir katkı malzemesidir. HL katma oranı, literatürde belirtilen ve önerilen genel kullanım oranının yaklaşık 1/3 kısmı olarak kullanılmıştır. Bir karışım uyumlaştırıcı fonksiyonu ve performans geliştirici olarak öngörülmüştür. D katkısı ise yine literatürde %13 oranı olarak genellikle kullanılırken bu araştırmada, çoklu katkı seçenekleri bağlamında, yine daha düşük ve çok düşük oranları olarak %5 ve %10 oranları kullanılmıştır.

HL+SBS birlikte kullanılan %50RAP katkılı karışımlarda ise çok daha yüksek su hasarı direnci söz konusudur. HL+SBS uyumunun daha yüksek bir su hasarı direnci oluşturduğu görülmektedir. Su hasarı performans artışı bakımından %50RAP katkılı karışımlarda HL+D birlikteliğine göre HL+SBS birlikteliği belirgin olarak daha fazla su hasarı direnci oluşturmaktadır. Her ne kadar HL katkısının bitümdeki karboksilik asit bileşenleri ile tepkimeye girdiği değerlendirilse de, esas anlamda bitüm ve karışım modifiyeri olan SBS katkısının HL ile daha yüksek uyum verdiği görülmektedir ve su hasarının da bitüm modifikasyonu ile olan ilişkisinin daha belirgin etkin faktör olduğu anlaşılmaktadır. SBS katkısı %50RAP katkılı karışımlarda sönmüş kireçli ve diatomitli karışımlar için su hasarı direncini daha da artırmış ve bu anlamda 0.90 değerini aşan çok yüksek bir su hasarı direnci oluşturmuştur. %0.5HL katkılı karışımlarda geleneksel SBS kullanım oranında daha düşük diatomit oranı (%5) daha belirgin bir iyileşme sağlayabilmiştir. Bu noktada, katkısız kontrol koşullu karışımlara göre %22,5 yüksek su hasarı direnci RAP katkılı karışımlar **için oluşmuştur ki bu çok üstün başarım olarak değerlendirilmektedir**. Buradan şu genel sonucu çıkarmak da olanaklıdır. SBS katkısı gerek sönmüş kireçle gerekse de diatomitle uyumlu çalışmaktadır.

Hidrate kirecin, asfalt kaplamada bağlayıcı filmi sertleştirmek için en çok kullanılan filler maddesi olduğu ve aktif dolgu partikülleri arasındaki güçlü fiziksel-kimyasal etkileşim nedeniyle agrega-asfalt bağını geliştirerek asfalt karışımının nem etkilerine karşı daha az duyarlı olmasına neden olduğu bilinmektedir. HL ve asfalt bağlayıcı gelişmiş kohezyon mukavemeti ve hasar direncine sahip bir bağlayıcı üretmektedir [41]. Diatomit modifiye asfalt karışımın su stabilite değerleri, modifiye edilmemiş karışıma kıyasla önemli ölçüde artmasına rağmen, diyatomitin asfalt karışımlarının çatlama direnci üzerinde çok az bir iyileştirmeye sahip olduğu belirtilmektedir [42]. Donma-çözülme döngüsü etkileri altında

diatomit ile modifiye edilmiş asfalt karışımının performansı araştırıldı. Diatomit kullanılarak nem hasarı direncinin açıkça iyileştirildiği belirtilmektedir [43-44]. Uçucu kül ve diatomit dahil olmak üzere üç tip katı atık maddenin, yoğun asfalt karışımların tekerlek izi ve nem-hasar direnci performansını artırmak için kireçtaşı tozuna alternatif doğal filler maddeleri olarak da kullanılabileceği belirtilmektedir [45].

Modifiye Lottman testi ayırt edici ve başarım düzeyi yüksek bir deney yöntemi olarak öngörülmektedir. Bu araştırmada da Modifiye Lottman testinin bu ayırt ediciliği görülmüştür. Belli mantık dahilinde kendisine yüklenen fonksiyonları gerçekleştirdiği görülen SBS, HL, Diatomit modifiye karışımlar için bu ayırt ediciliği bu karışımlar noktasında da göstermiştir. Düşük oranda HL, düşük oranda diatomit ve yaygın oranda %5SBS kullanım oranlarında; %50RAP karışımlar su hasarı direnci bakımından çok yüksek bir iyileşme sağlamaktadır. Bu sonuç bu karışımların uzun dönemli performans anlamında tekerlek izi ve diğer performans problemleri açısından da çok iyi sonuç vereceği anlamında değerlendirilmektedir.

Hamburg Tekerlek İzi Deneyi

Laboratuvar tekerlek izi testi sonuçları ile saha performansı arasında daha doğru bir ilişki bulmak için onlarca yıldır çaba sarf edilmiş ve Hamburg tekerlek izi (HWT) testi, asfalt kaplama analiz cihazı (APA), Fransız üstyapı tekerlek izi testi ve akma sayısı testi gibi çeşitli tekerlek izi test yöntemleri geliştirilmiştir. Bu test yöntemleri arasında, HWT tekerlek izi derinliğinin, hızlandırılmış yükleme kolaylığı ve saha tekerlek izi derinliği ile güçlü bir korelasyona sahip olduğu kanıtlanmıştır. Ek olarak, diğer tekerlek izi test yöntemleriyle karşılaştırıldığında, HWT testi, saha karotlarını test numunesi olarak kullanabilmektedir. Açıkça, laboratuvar tekerlek izi numuneleri ile karşılaştırıldığında, HWT tekerlek izi derinliğini kullanarak bir tekerlek izi tahmin modeli oluşturmak anlamlıdır [46].

Tekerlek izi deneyi İSFALT Laboratuvarındaki Şekil 10'da görülen Hamburg tekerlek izi cihazı kullanılarak yapılmıştır. Hamburg cihazı mikser, kompaktör ve test makinesi olmak üzere üç üniteden oluşmaktadır. Her üç ünite de elektronik ısı kontrol donanımlı olarak çalışmaktadır. İç kısımların ısıtılması ve kontrol sistemi, sıcak hava üflemesi veya su çevrimi ile yapılabilmektedir. Bütün test kontrolleri bilgisayar yazılımı ile desteklenmektedir. Online display bağlantı görüntüsü ve bilgi depolama özellikleri yardımıyla her bir tekerleğin oluşturduğu iz, sıcaklık ve geçiş sayısı sürekli olarak kaydedilmekte ve ekrandan da birebir izlenebilmektedir. Numune üzerinde oluşan tekerlek izi derinlikleri cihaza bağlı bilgisayar yardımıyla otomatik olarak hesaplanarak grafiğe yansıtılmaktadır. Bitümlü karışımların deformasyona karşı direnci, yüklü bir tekerleğin sabit sıcaklıkta (60°C) tekrarlanan geçişleriyle oluşan tekerlek izi derinliği ölçülerek değerlendirilmiştir. Numunelerde kullanılan optimum bağlayıcı, agrega gradasyonu ve malzeme özellikleri Marshall numuneleri için hazırlanan malzemeyle aynıdır. Deneyde kullanılmak üzere her bir karışım tipi için, 2'şer adet numune hazırlanmıştır. Hazırlanan numuneler deneysel uygulamaya alınmadan önce 48 saat bekletilerek dinlendirilmiştir. Marshall tasarımında tespit edilen 5,3 bitüm içeriğiyle hazırlanan numuneler, test edilmeden önce, deney sıcaklığı olan 60ºC'ye gelmesi için, ısı ayarlı test kabininde 4 saat süreyle bekletilmiştir. Deney, sağ ve sol tarafta bulunan iki kalıp içerisinde yer alan aynı özellikteki karışım numunelerine uygulanmış ve bu iki değerin ortalaması deney sonucu olarak kaydedilmiştir. 20000 geçiş yapılarak tekerlek izi

derinlikleri tespit edilmiştir. Grafiklerle gösterilen tekerlek izi ölçümleri tüm karışımlar için Şekil 11-13'de verilmektedir. TS EN 12697-22 prosedürü uygulanmıştır.

Şekil 10 - HWTT tekerlek izi test cihazı

Su hasarı deneyleri ve Hamburg tekerlek izi deneylerinin seçilen yöntemler olarak tutarlılıkları bu araştırmada oluşturulan geleneksel ve modifiye karışımlar için de net olarak gözlenmektedir. Geleneksel RAP içermeyen kontrol SBS karışımın 20 bin yükleme sonunda oluşturduğu deformasyon derinliği 1,89mm olmuştur. Bu karışıma %50 oranında RAP katılmasıyla, sönmüş kirecin birlikte kullanılması durumunda 1,95mm tekerlek izi derinliği oluşmuştur. %50RAP olmasına karşın bu değer, katkısız ve RAP olmayan karışımların yani kontrol karışımların 2,34mm tekerlek izi derinliğine göre %20 daha fazla bir tekerlek izi direnci oluştuğunu göstermektedir.

Şekil 11 karışımlar için sol tekerlek grafiklerini, Şekil 12 sağ tekerlek grafiklerini ve Şekil 13 ise ortalama tekerlek izi grafiklerini sunmaktadır. %50RAP katkılı karışımlarda HL ve SBS katkılı karışımlara %5diatomit ilavesinde 1,85mm; %10 diatomit katılması durumunda ise 1,83mm tekerlek izi derinlikleri oluşmaktadır. %50RAP katkılı seçeneklerde karışıma HL+SBS katkı birlikteliğine diatomit eklenmesi düşük ya da orta oranda kullanım noktasında (%5-%10) tekerlek izi direncini artırmaktadır. %50RAP katkılı seçeneklerde %5SBS oranında, düşük oranda HL (%0,5) ve düşük oranlı diatomit için tekerlek izi dirençleri; hiç katkısız kontrol karışımlara göre %27 oranında; SBS katkılı kontrol hasarsız karışımlara göre %3 oranında daha iyi sonuç vermektedir. Açıkça SBS katkısının tekerlek izi direnci konusundaki üstünlüğü görülmektedir. %50RAP katkılı karışımlarda da SBS katkısının HL ve HL+diatomit birlikteliğiyle uyumlu çalışması SBS katkısının farklı filler malzemeler ile rahatlıkla kullanılabileceğini işaret etmektedir. Oluşturulan SBS'li ve düşük oranlı HL+Diatomit seçenekleri %50RAP katkılı karışımları orijinal karışımlara göre daha yüksek tekerlek izi direncine kavuşturmaktadır. Oluşturulan bu katkı seçenekleri %50RAP geri dönüşüm konusunu mümkün kılmaktadır.

Şekil 13'de ortalama tekerlek izi derinlikleri (mm) verilmektedir. Artan diatomit oranına göre karşılaştırma yapılması ayrıca hedeflendiği ve grafiklerde anlaşılırlığın oluşması için grafikler bu bakımdan düzenlenmiştir. Tekerlek izi bakımından SBS polimer üstün performans sağlamaktadır. 20000 yükleme altında tüm RAP %50 katkılı karışımlarda sabit

%0,5HL katkısı bulunmaktadır. Su hasarı deneylerindeki gibi burada da SBS ve HL arasında, HL düşük değerde kullanılsa da (1/3) önemli bir birlikte çalışma etkisi (sinerji) oluşmaktadır. SBS ve HL katkıları bir arada yüksek uyumludur ve birlikte çalışmaktadır.

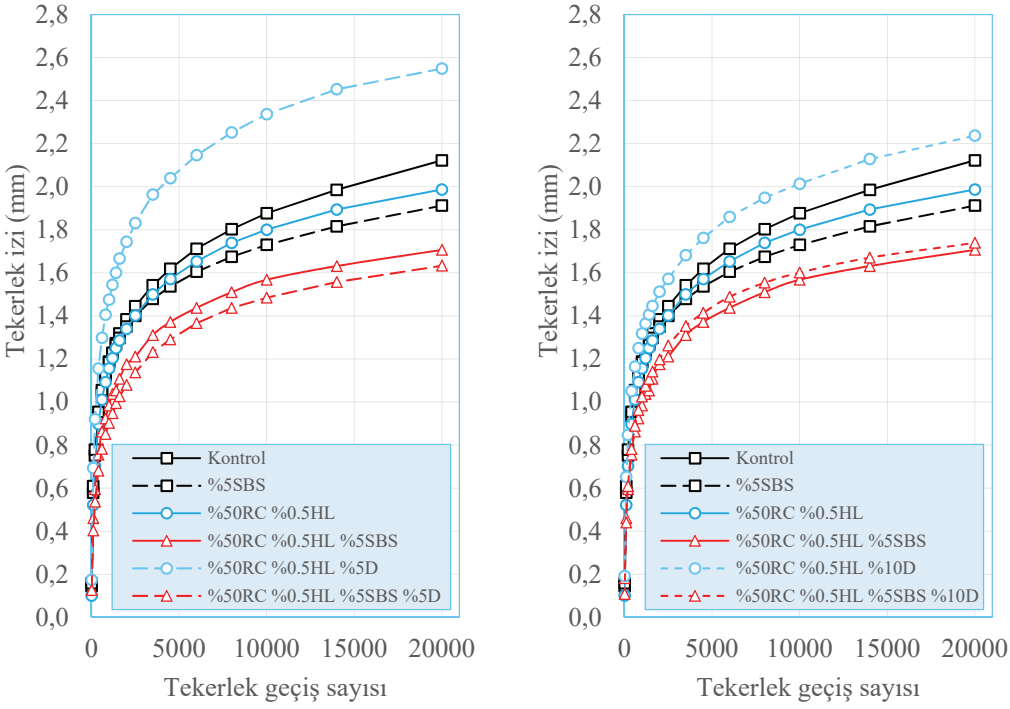

Şekil 11 - Sol tekerlek deformasyon eğrileri

SBS katkısının yanına HL eklenmesi, SBS+HL birlikteliğine diatomit eklenmesi durumunda Hamburg tekerlek izi testi bu katkısal gelişim düzeyini tekerlek izi direnci bakımından ortaya koymaktadır. Bu bakımdan Hamburg tekerlek izi deneyi bu ayırt ediciliği noktasında üstün bir deney yöntemi olarak değerlendirilmiştir. Hamburg tekerlek izi deneyi kuru ortam olarak gerçekleştirilmiştir. Kullanılan HL katkısının kimyasal bir modifiyer olarak gerek agrega ile suyun varlığında ve gerekse de bitümün karboksilik asitleriyle girdiği tepkime sonucunda tekerlek izi bakımından çok daha yüksek tekerlek izi direncinin aktif adezyon koşullarında oluşacağı değerlendirilmektedir. Bu kuru deneyde de SBS kontrol karışımlara göre belirgin olarak tekerlek izi direncini artırmaktadır. Su hasarı direnci bakımından olduğu gibi tekerlek izi direnci bakımından da %50RAP katkılı karışımlar SBS ve HL ve D katkıları ile tekerlek izi direnci bakımından kontrol karışımlardan %28-%45 düzeyinde daha iyi tekerlek izi direnci göstermiştir. Bu durum seçilen 20000 yükleme koşulu için geçerli olmuştur. Su hasarı sonuçları ile birlikte değerlendirildiğinde daha yüksek yükleme sayıları yani uzun dönemli tekerlek izi direnci bakımından oluşturulan bu katkı birleşiminin daha da üstün tekerlek izi direnci göstereceği değerlendirilmelidir. Bu konu diğer araştırmalara konu edilecektir. Oluşturulan tüm %50RAP katkılı modifiye karışımların kontrol karışımlardan daha yüksek

tekerlek izi direnci vermesi %50RAP karışımların uygulamada başarıyla kullanılabileceğini göstermektedir. Araştırma sonuçlarının yorulma performansı bakımından da seçilen bir pilot karışım olarak %50RAP+%0.5HL+%5SBS+%5diatomit karışımı için gerçekleştirilmesi düşünülmektedir.

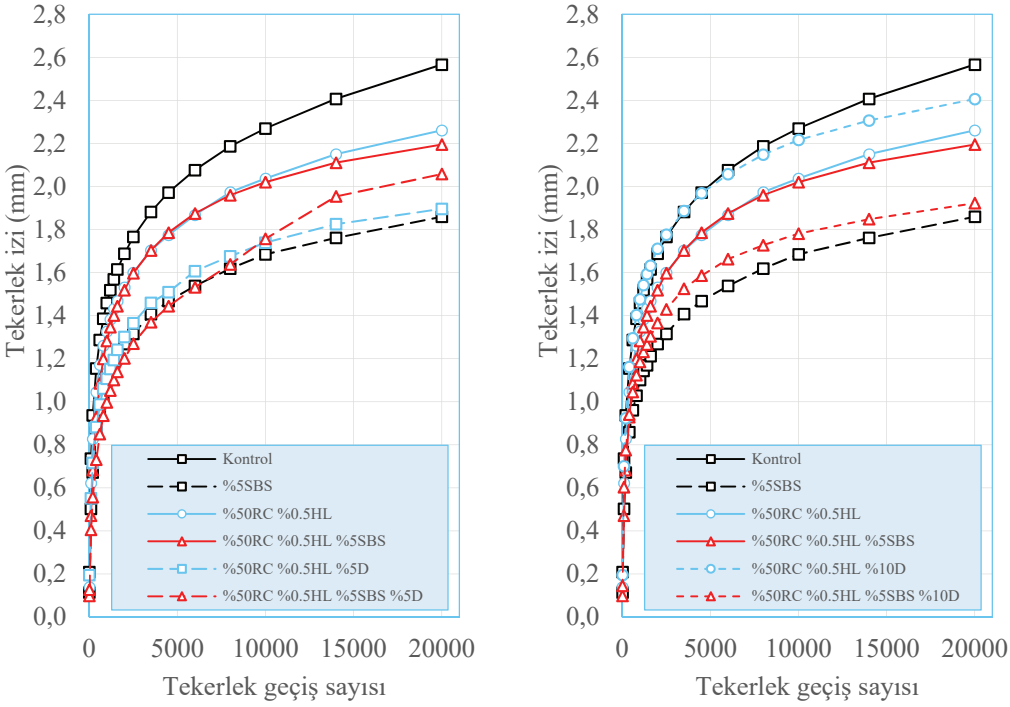

Şekil 12 - Sağ tekerlek deformasyon eğrileri

Filler ilavesinin, karışımdaki düşük oranına rağmen karışım mukavemetini artırdığı kanıtlanmıştır. Filler tozunun ikili rol oynadığına inanılmaktadır. Filler temel işlevi; boşlukları doldurmak, büyük agregalar arasında çok sayıda temas noktası sağlamak ve böylece bağlayıcı ve agrega birbirine geçme etkilerini artırarak karışımı güçlendirmektir. Diğer işlevi, bağlayıcıyı sertleştirmek ve büyük agrega parçacıkları arasında daha iyi yapışmaya katkıda bulunan daha **yüksek tutarlılıklı** bir bağlayıcı veya mastik oluşturmaktır [47]. D kireçtaşı tozuna kıyasla mineral fillere uygun alternatif olduğundan, giderek daha fazla ilgi kazanmaktadır. D-kireçtaşı tozunun çeşitli hacim oranlarına (0:1, 0,25:0,75, 0,5:0,5, 0,75:0,25 ve 1:0) sahip beş grup kum asfalt, SLD yöntemi ile değerlendirildi. D kullanımıyla, kum asfaltların sıkıştırma mukavemeti, deformasyon özellikleri ve düşük sıcaklık çatlak direncinin iyileştirildiğini görüldü. Kireçtaşı-D optimal oranı; sekant modülü ve sünme gerinim sonuçlarına göre SLD yöntemiyle (0,327:0,673) olarak belirlendi [48].

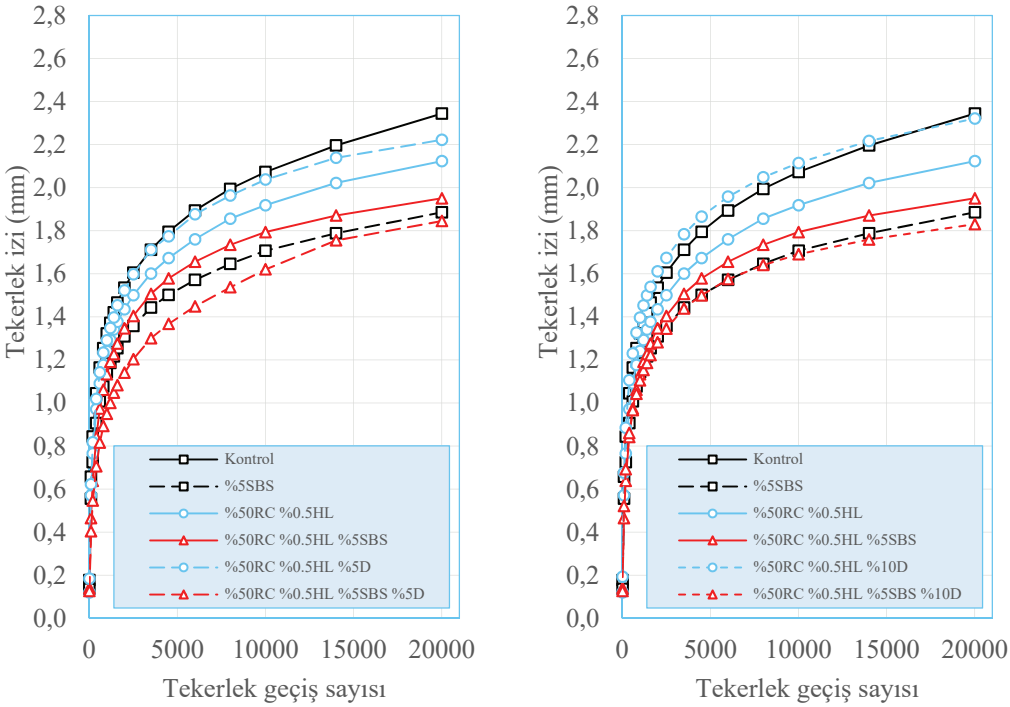

Şekil 13 - Ortalama tekerlek izi eğrileri

Şekil 13'de eğrileri verilen ortalama tekerlek izi değerlerinin, sayısal olarak belirli tekerlek geçiş sayılarında tekerlek izi miktarları (mm) Tablo 17'de verilmektedir.

Diatomit asfalt mastiğinin; kireçtaşı, HL ve uçucu kül asfalt mastiklerinden daha iyi performans gösterdiği ve potansiyel filler olduğu belirtilmektedir [35]. DMA, yüksek sıcaklık ve reolojik özellikleri iyileştirmekte, düşük sıcaklık özelliğini ise önemli ölçüde etkilememektedir. DMA yaşlanma direnci, diatomit içeriği arttıkça önemli ölçüde iyileşmektedir [49-50]. Asfalt filler mastiği üretmek için %2 içerikli HL, çimento ve D seçilmiştir. Filler kullanımı mastiklerin sertliğini artırmaktadır. D mastik, yüksek sıcaklık ve stres seviyelerinde tekerlek izine karşı en iyi direnci sergiler ve diatomit filler kullanımının uygun olduğunu doğrular [51]. Mineral fillerlerin birkaç polimer modifiye bitümün reolojik davranışına etkisi–araştırıldı. PMB'leri üretmek için saf bir bitüm ve iki tip polimer (elastomerik ve plastomerik) kullanılmış ve mastik elde etmek için farklı minerallere (kireçtaşı ve bazalt) sahip iki filler maddesi seçildi. Değiştirilmemiş mastikler için BBR sonuçları, filler tipinden bağımsız olarak sertlik artışının benzer olduğunu gösterirken, polimer modifiye mastikler için sonuçlar, takviye derecesinin filler/polimer tipi kombinasyonuna bağlı olduğunu göstermektedir Filler ilavesi, filler/polimer kombinasyonuna bağlı olarak, kalıcı deformasyon duyarlılığını azaltmakta ve elastik tepkiyi artırmaktadır. Filler ile bitüm arasında fiziksel-kimyasal etkileşim oluşmakta ve etkileşim seviyesinin büyük ölçüde polimer modifikasyonunun tipine bağlı olduğu görülmektedir [47].

Tablo 17 - Belirli tekerlek geçiş sayılarında tekerlek izi miktarı (mm)

Tekerlek geçişi	Kontrol			%5SBS			%50RC %0,5HL			%50RC %0.5HL %5SBS			%50RC %0.5HL %5SBS %10D			%50RC %0.5HL %10D			%50RC %0.5HL %5SBS %5D			%50RC %0.5HL %5D		
	Sol	Sağ	Ort	Sol	Sağ	Ort	Sol	Sağ	Ort	Sol	Sağ	Ort	Sol	Sağ	Ort	Sol	Sağ	Ort	Sol	Sağ	Ort	Sol	Sağ	Ort
10	0,15	0,21	0,18	0,16	0,11	0,14	0,10	0,14	0,12	0,18	0,10	0,14	0,11	0,15	0,13	0,19	0,20	0,19	0,13	0,13	0,13	0,17	0,20	0,18
100	0,58	0,74	0,66	0,61	0,50	0,56	0,52	0,62	0,57	0,46	0,47	0,47	0,44	0,60	0,52	0,65	0,70	0,68	0,40	0,41	0,40	0,69	0,55	0,62
200	0,75	0,94	0,84	0,78	0,67	0,73	0,70	0,83	0,77	0,60	0,68	0,64	0,61	0,78	0,69	0,85	0,92	0,89	0,54	0,56	0,55	0,92	0,72	0,82
500	0,99	1,23	1,11	1,01	0,92	0,96	0,95	1,11	1,03	0,80	1,02	0,91	0,84	0,99	0,92	1,11	1,24	1,18	0,73	0,80	0,77	1,23	0,93	1,08
1000	1,19	1,46	1,32	1,19	1,10	1,14	1,16	1,33	1,24	0,98	1,28	1,13	1,03	1,19	1,11	1,32	1,48	1,40	0,90	1,00	0,95	1,48	1,11	1,29
2000	1,38	1,69	1,54	1,35	1,27	1,31	1,34	1,53	1,44	1,18	1,52	1,35	1,20	1,37	1,28	1,51	1,71	1,61	1,08	1,20	1,14	1,74	1,30	1,52
4000	1,58	1,93	1,76	1,51	1,43	1,47	1,54	1,74	1,64	1,35	1,74	1,55	1,38	1,56	1,47	1,72	1,93	1,83	1,26	1,41	1,34	1,99	1,48	1,74
6000	1,71	2,08	1,89	1,61	1,54	1,57	1,65	1,87	1,76	1,44	1,87	1,66	1,49	1,66	1,58	1,86	2,06	1,96	1,37	1,53	1,45	2,15	1,61	1,88
10000	1,88	2,27	2,07	1,73	1,69	1,71	1,80	2,04	1,92	1,57	2,02	1,79	1,60	1,78	1,69	2,01	2,22	2,12	1,49	1,76	1,62	2,34	1,74	2,04
12000	1,94	2,34	2,14	1,78	1,72	1,75	1,85	2,10	1,98	1,60	2,07	1,84	1,64	1,82	1,73	2,08	2,27	2,17	1,53	1,87	1,70	2,39	1,77	2,08
14000	1,99	2,41	2,20	1,82	1,76	1,79	1,89	2,15	2,02	1,63	2,11	1,87	1,67	1,85	1,76	2,13	2,31	2,22	1,56	1,95	1,76	2,45	1,83	2,14
16000	2,03	2,46	2,25	1,85	1,81	1,83	1,92	2,19	2,05	1,69	2,14	1,91	1,70	1,88	1,79	2,17	2,35	2,26	1,58	2,01	1,80	2,49	1,85	2,17
18000	2,08	2,51	2,30	1,88	1,84	1,86	1,96	2,23	2,09	1,68	2,17	1,93	1,72	1,90	1,81	2,21	2,38	2,29	1,61	2,04	1,82	2,54	1,89	2,21
20000	2,12	2,57	2,34	1,91	1,86	1,89	1,99	2,26	2,12	1,71	2,20	1,95	1,74	1,92	1,83	2,24	2,41	2,32	1,63	2,06	1,85	2,55	1,90	2,22

Diatomitin, mineral tozlara kıyasla asfalt mastiğin yaşlanmasını önemli ölçüde iyileştirdiği görüldü. Asfalt mastik, diatomit değiştirme oranı %75 olduğunda yüksek sıcaklıkta optimum mekanik özelliklere sahip olmaktadır [52]. Orta ve yüksek sıcaklıklarda asfalt mastik üzerinde diatomitin iyileştirmesinin HL ve uçucu külden daha etkin olduğu belirtilmektedir [35].

Diatomit tekerlek izi direncini önemli ölçüde iyileştirmekte buna karşın eğilme rijitlik modülü arttığında düşük sıcaklık performansını düşürmektedir. Diatomit ilavesi; asfalt mastik ve karışımının yüksek sıcaklık stabilitesine ve yaşlanma karşıtı performans gelişimine katkıda bulunmaktadır [53]. Diatomitin asfalt karışımların rijitlik modülü üzerinde önemli etkiye sahip olduğu, asfalt karışımların tekerlek izi ve yorulma önleme performansını artırdığı görüldü. Diatomit, asfalt karışımların çeşitli özelliklerini büyük ölçüde iyileştirmiştir. Ancak bu çalışmalar yoğun gradasyonlu asfalt karışımlarına dayalı iken, açık gradasyonlu karışımlara yönelik araştırmalar daha azdır [36].

SONUÇLAR

%15-20 RAP katkılı karışımlar, dizayn süreçlerinde bir sorun oluşturmaksızın rahatlıkla kullanılabilmektedir. %50 oranında RAP kullanımı yüksek bir orandır ve bu araştırmada daha yüksek ekonomik ve diğer kazanımlar noktasında bu karışımlar sorgulanmaktadır.

Asfalt karışımın üretim aşamasında, plentlerde bitüm oksidasyonu ve buharlaşan bileşen kaybıyla yaşlanma oluşmaktadır. Arazi koşullarında artan oksidasyon ise uzun süreli yaşlanma olmaktadır. RAP katkılı karışımlar bu anlamda iki tür yaşlanmaya da maruz kalmışlardır ve tekrar üretime girdiklerinde yeniden yaşlanacaklardır. Bu bakımdan; diatomit katkısına silika içeriği ile ısı yayılımını kontrol ederek yaşlanmayı azaltması yönüyle karar verilmiştir. Sönmüş kirecin bitüm üzerindeki yaşlanma önleyici etkileri ayrıca düşünülmüştür. %50RAP katkılı karışımlarda; SBS katkısı ve bu filler türü katkıların birlikte çalışma etkisi değerlendirilmiş ve katkı seçim süreci özellikle yaşlanma yönlü iyileştirme pratiği üzerine odaklandırılmıştır. SBS polimer varlığında, SBS polimer ile birlikte çalışma etkisi ele alınarak ve düşük oranlarda da performans artışı sağladıkları bilindiğinden dolayı; D ve HL yaygın kullanım oranlarının oldukça düşük değerlerinde (1/3) kullanılmıştır. Diatomitin yeni perspektif olarak, düşük ve orta kullanım oranı (%5-%10) seçenekleri de dahil edilmiştir (Maksimum %13 olarak biliniyor). SBS polimeri %5 yaygın kullanım oranında kullanılmıştır. Bu araştırmadan aşağıda belirtilen sonuçları çıkarmak olanaklı gözükmektedir:

Modifiye Lottman testinin; D, HL, SBS ve RAP'lı karışımlar için ayırt edici olduğu ve performansları başarımlı yansıttığı görülmektedir. %0,5 HL oranında (düşük HL oranı-%1-1,5 genelde kullanılan); D oranının %5'den (%18 artış) %10 değerine (%13 artış) artırılması ile su hasarı direncinin artması, HL ve diatomitin birlikte performans artışı oluşturduğunu göstermektedir. HL+SBS birlikteliği (0.92); HL+D (%5D) birlikteliğine göre (0.87) daha yüksek bir su hasarı direnci oluşturmaktadır. SBS katkısı gerek HL gerekse de diatomitle uyumlu çalışmaktadır. Düşük oranda HL, düşük oranda D ve yaygın oranda %5SBS kullanım oranlarında; %50RAP karışımlar su hasarı direnci bakımından çok yüksek (0.99) bir iyileşme (%19 fazla) sağlamaktadır.

%50RAP katkılı (HL-D-SBS) modifiye karışımların; kontrol karışımlardan %27 daha yüksek tekerlek izi direnci vermesi bu karışımların başarıyla kullanılabileceğini göstermektedir. %50RAP seçenekleri, seçilen katkı birleşimleri ile orijinal karışımlardan daha dirençli hale hem tekerlek izi hem de su hasarı deneylerinde getirilmiştir. Düşük kullanım oranlı diatomit+HL birlikteliğinin, SBS oranı azaltılması için kullanılıp kullanılamayacağı araştırılmalıdır.

Kaynaklar

[1] Williams BA, Copeland A, Ross TC. Asphalt Pavement Industry Survey on Recycled Materials and Warm-Mix Asphalt Usage: 2017 Natl. Asph. Pavement Assoc., vol. 8th Annual, no. Information Series 138 (8th edition), IS 138(8e).

[2] Williams BA, Willis JR, Shacat J. Asphalt Pavement Industry Survey on Recycled Materials and Warm-Mix Asphalt Usage: 2021, Natl. Asph. Pavement Assoc., vol. 12th Annual, no. 12th Annual Asphalt Pavement Industry Survey IS 138 Produced December 2022.

[3] Zaumanis M, Cavalli M C and Poulikakos LD. How not to design 100% RAP using performance-based tests, Road Mater. Pavement Des., vol. 0, no. 0, pp. 1–13, 2018.

[4] Tran N, Taylor A, Turner P, Holmes C and Porot L. Effect of rejuvenator on performance characteristics of high RAP mixture, Asph. Paving Technol. Assoc. Asph. Paving Technol. Tech. Sess., vol. 85, pp. 283–313, 2016.

[5] Zaumanis M. 100 % Recycled Hot Mix Asphalt and the Use of Rejuvenators, Worcester Polytechnic Institute2014.

[6] Tarsi G, Tataranni P, Sangiorgi C. The Challenges of Using Reclaimed Asphalt Pavement for New Asphalt Mixtures: A Review, 13, 4052; doi:10.3390/ma13184052 Materials 2020.

[7] Brett AW, Willis JR, Ross TC. Asphalt Pavement Industry Survey on Recycled Materials and Warm-Mix Asphalt Usage: 9th ed.; IS 138; National Asphalt Pavement Association: Greenbelt, MD, USA, 2019.

[8] European Asphalt Pavement Association—EAPA. Asphalt in Figures 2018; EAPA: Brussels, Belgium, 2018.

[9] Copeland, A. Reclaimed Asphalt Pavement in Asphalt Mixtures: State of the Practice; No. FHWA-HRT-11-021; Federal Highway Administration: McLean, VA, USA, 2011.

[10] Aurangzeb Q, Al-Qadi IL, Ozer H, Yang R, Hybrid life cycle assessment for asphalt mixtures with high RAP content, Resour. Conserv. Recycl. 83 77–86, https://doi.org/10.1016/j.resconrec.2013.12.004. (2014)

[11] Visintine BA. An investigation of various percentages of reclaimed asphalt pavement on the performance of asphalt pavements, Materials Science, 17 March 2011.

[12] Li J, Xiao F, Zhang L, Amirkhanian SN. Life Cycle Assessment And Life Cycle Cost Analysis Of Recycled Solid Waste Materials İn Highway Pavement: A Review, J. Clean. Prod. 233 1182–1206, https://doi.org/10.1016/j.jclepro.2019.06.061, 2019.

[13] Li X, Marasteanu MO, Williams RC, Clyne TR. Effect of reclaimed asphalt pavement (proportion and type) and binder grade on asphalt mixtures, Transp. Res. Rec. 2051 (1) 90–97, https://doi.org/10.3141/2051-11 2008.

[14] Zaumanis M, Mallick RB, Frank R, 100% Recycled Hot Mix Asphalt: A Review And Analysis, Resour. Conserv. Recycl. 92, 230–245, 2014.

[15] Karimi MM, Jahanbakhsh H, Nejad FM. Energy-Based Approach To Characterize İnduced Heating Of Asphalt Concrete Under Electromagnetic Field, Constr. Build. Mater. 273 2021.

[16] Zhang K., Huchet F, Hobbs A. A Review Of Thermal Processes İn The Production And Their İnfluences On Performance Of Asphalt Mixtures With Reclaimed Asphalt Pavement (RAP), Constr. Build. Mater. 206 (2019) 609–619,

[17] Kandhal PS, Mallick RB. Pavement Recycling Guidelines For State And Local Governments: Participant's Reference Book. No. FHWA-SA-98-042, 1997.

[18] Zaumanis M and Mallick RB. Review Of Very High-Content Reclaimed Asphalt Use İn Plantproduced Pavements: State Of The Art, Int. J. Pavement Eng., vol. 16, no. 1, pp. 39–55 2015

[19] Molenaar AAA, Hagos ET, Van de Ven MFC. Effects of Aging on the Mechanical Characteristics of Bituminous Binders in PAC, J. Mater. Civ. Eng., vol. 22, no. 8, pp. 779– 787, 2010.

[20] Rathore M et al. Asphalt Recycling Technologies: A Review on Limitations and Benefits, IOP Conf. Ser. Mater. Sci. Eng. 660 012046, IOP Publishing doi:10.1088/1757-899X/660/1/012046, 2019.

[21] Anderson E, Daniel JS. Long-Term Performance Of Pavement With High Recycled Asphalt Content: Case Studies. Transportation Research Record: Journal Of The Transportation Research Board, No. 2371. Transportation Research Board of the National Academies, Washington, DC, pp 1–12. doi:10.3141/2371-01 2013.

[22] Apeagyei A, Clark T, Rorrer T. Stiffness of high RAP asphalt mixtures: Virginia's experience, J Mater Civ Eng 25(6):747–754. doi:10.1061/(ASCE)MT.1943-5533. 0000543, 2013.

[23] Olita S, Ciampa D. SuPerPave® Mix Design Method of Recycled Asphalt Concrete Applied in the European Standards Context, Sustainability, 13, 9079. https://doi.org/10.3390/su13169079, 2021.

[24] Mangiafico S et al. Statistical Analysis Of The İnfluence of RAP And Mix Composition On Viscoelastic And Fatigue Properties Of Asphalt Mixes, Materials and Structures 48:1187–1205 DOI 10.1617/s11527-013-0225-z, 2015.

[25] Cong PL, Zhou B, Chen SF. Low Temperature Rheological And Mechanistic Characteristics Of Three Different Types Of Asphalt Binders, Int. J. Pavement Res. Technol. 4 307–312, 2011.

[26] Dony A, Colin J, Bruneau D, Drouadaine I, Navaro J. Reclaimed Asphalt Concretes With High Recycling Rates: Changes İn Reclaimed Binder Properties According To Rejuvenating Agent, Constr. Build. Mater. 41 175–181, 2013.

[27] Gonzalez O, Munoz ME, Santamaría A. Rheology And Stability Of Bitumen/ EVA Blends, Eur. Polym. J. 40 2365–2372, 2004.

[28] Cong P et al. Investigation Of The Properties Of Asphalt Mixtures İncorporating Reclaimed SBS Modified Asphalt Pavement, Construction and Building Materials 113 334–340, 2016.

[29] Colbert B, You Z. The Properties Of Asphalt Binder Blended With Variable Quantities Of Recycled Asphalt Using Short Term And Long Term Aging Simulations, Constr. Build. Mater. 26, 552–557, 2012.

[30] Yu X, Zaumanis M, Santos S, Poulikakos LD. Rheological, Microscopic, And Chemical Characterization Of The Rejuvenating Effect On Asphalt Binders, Fuel 135 162–171, 2014.

[31] Valdes G, Perez-Jimenez F, Miro R, Martinez A, Botella R. Experimental Study Of Recycled Asphalt Mixtures With High Percentages Of Reclaimed Asphalt Pavement (RAP), Constr. Build. Mater. 23 1289–1297, 2011.

[32] Shirodkar P, Mehta Y, Nolan A, Sonpal K, Norton A, Tomlinson C, Dubois E, Sullivan P, Sauber R. A Study To Determine The Degree Of Partial Blending Of Reclaimed Asphalt Pavement (RAP) Binder For High RAP Hot Mix Asphalt, Constr. Build. Mater. 25 150–155, 2011.

[33] Huang B, Li G, Vukosavljevic D, Shu X, Egan BK. Laboratory Investigation of Mixing Hot-Mix Asphalt with Reclaimed Asphalt Pavement. In Transportation Research Record: Journal of the Transportation Research Board, No. 1929, Transportation Research Board of the National Academies, Washington D.C. pp. 37–45. 2005.

[34] Bouron S, Hammoum F, Ruat H. et al. Improving The Durability Of Asphalt Mixtures With Hydrated Lime: Field Results From Highway A84, Case Studies in Construction Materials 14 e00551 2021.

[35] Cheng Y, Tao J, Jiao Y et al. Influence Of The Properties Of Filler On High And Medium Temperature Performances Of Asphalt Mastic, Construction and Building Materials, vol. 118, pp. 268–275, 2016.

[36] Guo Q, Li L, Cheng Y, Jiao Y, and Xu C. Laboratory Evaluation On Performance Of Diatomite And Glass Fiber Compound Modified Asphalt Mixture, Materials and Design, vol. 66, pp. 51–59, 2015.

[37] Zhou Z. Experimental Study on Mix Design of Diatomite Modified Asphalt Mixture. Master's Thesis, Jilin University, Changchun, China, 2008.

[38] Li ZS. A Study on The Performance of Diatomite Modified Asphalt Mixture. Master's Thesis, Jilin University, Changchun, China, 2008.

[39] Jahangiri B et al. Performance Evaluation of Asphalt Mixtures With Reclaimed Asphalt Pavement And Recycled Asphalt Shingles İn Missouri, Transp. Res. Rec. 2019.

[40] AASHTO (2014). Standard Method of Test for Resistance of Compacted Asphalt Mixtures to Moisture-induced Damage. AASHTO T 283e14. American Association of State and Highway Transportation Officials, Washington, DC.

[41] Epps J, Berger E, and Anagnos JN. Treatments. In: Moisture Sensitivity Of Asphalt Pavements: A National Seminar. Washington, D.C.: Transportation Research Board of the National Academies. 117–183, 2003.

[42] Yang C, Xie J, Zhou X, Liu Q, Pang L. Performance Evaluation and Improving Mechanisms of Diatomite-Modified Asphalt Mixture. Materials, 11, 686, 2018.

[43] Shukry NAM, Hassan NA, Abdullah ME, Hainin MR, Yusoff NIM, Jaya RP, Mohamed A. Effect Of Various Filler Types On The Properties Of Porous Asphalt Mixture. IOP Conf. Ser. Mater. Sci. Eng. 342, 012036, 2018.

[44] Luo S, Chen N, Xu H, Tan B, Chen, Q. Study on Indoor Pavement Performance of Diatomite-Modified Asphalt Mixture. In Proceedings of the 2016 International Conference on Innovative Material Science and Technology (IMST 2016), Shenzhen, China, 19–21 August 2016.

[45] Zhang H. Optimum Filler–Bitumen Ratio of Asphalt Mortar Considering Self-Healing Property, J. Mater. Civ. Eng. ©ASCE, 31-8, American Society of Civil Engineers https://doi.org/10.1061/(ASCE)MT.1943-5533.0002792 August 2019.

[46] Chen L et al. Rutting Prediction Model for Semirigid Base Asphalt Pavement Based on Hamburg Wheel Tracking Test, Int. J. Geomech., 21(11): 04021215, ASCE, 2021.

[47] Cardone, F et al. Influence Of Mineral Fillers On The Rheological Response Of Polymer-Modified Bitumens And Mastics, Journal of Traffic and Transportation Engineering, 2 (6), 373–381, 2015.

[48] Cheng Y et al. Effects of Diatomite–Limestone Powder Ratio on Mechanical and Anti-Deformation Properties of Sustainable Sand Asphalt Composite, Sustainability, 10, 808, 2018.

[49] Cong P, Chen S, Chen H. Effects Of Diatomite On The Properties Of Asphalt Binder, Constr. Build. Mater. 30, 495–499, 2012.

[50] Cong P, Liu N, Tian Y, Zhang Y. Effects Of Long-Term Aging On The Properties Of Asphalt Binder Containing Diatoms. Constr. Build. Mater. 123, 534–540, 2016.

[51] Shukrya NAM et al. Influence Of Diatomite Filler On Rheological Properties Of Porous Asphalt Mastic, International Journal Of Pavement Engineering, VOL. 21, NO. 4, 428–436 https://doi.org/10.1080/10298436.2018.1483504, 2020.

[52] Wang YD. Research On The Anti-Ageing Mechanism And Mechanical Properties Of Diatomite Modified Asphalt Binder [Master's thesis], Jilin University, Changchun, China, 2015.

[53] Zhu DP, Zhang JZ, Chen JB, Yuan K, Cheng C. Experiment On Road Performance Of Diatomite Modified Asphalt Mixture in Permafrost Regions, China Journal of Highway and Transport, vol. 26, no. 4, pp. 23–28, 2013.

Turkish Journal of Civil Engineering, 2023, 81-98, Paper 752, ***Research Article***

On a New Method of Quasi-static and Dynamic Analysis of Viscoelastic Plate on Elastic Foundation

Gülçin TEKİN[1*]
Fethi KADIOĞLU[2]

ABSTRACT

An alternative solution technique based on mixed finite element (MFE) formulation in the Laplace-Carson domain is proposed for quasi-static and dynamic analyses of viscoelastic plate (VEP) resting on an elastic foundation (EF). This work contributes a numerical solution to the problem of a viscoelastic Kirchhoff plate supported on a Winkler foundation. VEP-EF interaction problems are taken into account under different wave-type loadings. The viscoelastic material behavior of the plate is modeled by the Zener rheological solid model. A four-nodded linear isoparametric element with sixteen degrees of freedom is used to model the VEP. The functional developed in the Laplace-Carson domain based on the Gâteaux differential method is transformed to the real time domain by utilizing the Dubner and Abate (D&A) inverse Laplace transform technique (ILTT). To evaluate the applicability of the results, five numerical samples are considered. Further analyzes are performed on different wave type loadings to offer a new perspective on the time-dependent behavior of VEP on EF.

Keywords: Viscoelastic plate, plate-foundation interaction, wave-type loadings, Gâteaux differential, Laplace-Carson transform, Dubner & Abate.

1. INTRODUCTION

Analysis of interaction of different structural elements with the supporting foundation is a typical problem in diverse fields of modern engineering disciplines such as structural, pavement and foundation. Numerous authors have employed various approximate numerical methods to investigate structural element - foundation interaction problems in recent years.

Note:
- This paper was received on March 21, 2023 and accepted for publication by the Editorial Board on September 4, 2023.
- Discussions on this paper will be accepted by January 31, 2024.
- https://doi.org/10.18400/tjce.1268992

1 Department of Civil Engineering, Yıldız Technical University, Istanbul, Türkiye
gulcint@yildiz.edu.tr - https://orcid.org/0000-0003-0207-4305

2 Department of Civil Engineering, Istanbul Technical University, Istanbul, Türkiye
fkadioglu@itu.edu.tr - https://orcid.org/0000-0001-7049-1704

* Corresponding author

Plate-foundation interaction problems are very common in civil engineering. In many practical applications, elastic and viscoelastic plates are in contact with the soil. Elastic ground effects are among the many factors that can have significant and unexpected effects on the behavior of plates. Therefore, there is a need to understand the behavior of composite plates resting on the elastic foundation. There are Winkler and Pasternak models, elastic half-space models, and other approximate models describing elastic foundations [1-2]. The Pasternak model has been widely adopted to describe the mechanical behavior of elastic soils, and the well-known Winkler model is a special case of this model. The Winkler elastic foundation model provides satisfying results in many practical engineering applications. A concise review of elastic foundation models is considered by Wang et al. [3] and Kerr [4]. In many research papers, elastic plate-Winkler elastic foundation interaction problems are investigated using various techniques such as boundary element, finite difference and finite element [5-14], which assumes that the plate material is linear elastic. When viscoelastic materials have been incorporated as structural elements in many engineering situations, the need for studies on viscoelastic problems has increased. Viscoelastic constitutive relations are more realistic than elastic constitutive relations to reflect the material behavior. Basic concepts regarding the mechanical behavior of viscoelastic structural components are presented in the studies [15-21]. The investigation of ground effects on the behavior of elastic/viscoelastic plates has been the subject of many studies [22-35]. Based on our literature review, many research activities have been devoted to the development of theoretical and computational methods for elastic/viscoelastic plate - elastic/viscoelastic foundation interaction problems. However, to the best of our knowledge, this study is unique in that it proposed MFE formulation to analyze the response of thin VEPs, which is modeled by the Zener rheological solid model, subjected to wave-type loadings and resting on EF. In the present study, different quasi-static and dynamic example problems are considered for quantifying the effect of EF on the behavior of VEPs. This study has contributions to scientific knowledge as follows: this study presents an improved MFE formulation that is simple, reliable and efficient in computations. By mixed formulation moment and shear force values (if any) are obtained independently from displacements without any back substitution process, which is unavoidable in displacement models. All field equations can be enforced to the functional systematically. For instance, the Gâteaux differential method can be applied to any field equations for which stationary functional and boundary condition terms of the problem under consideration are not known beforehand. Geometric and dynamic boundary conditions can be obtained more easily. For the Gâteaux differential method, boundary conditions are wholly dealt with through mathematical manipulations. The field equations can be verified via potential testing, which is defined by [36]. The Gâteaux differential method is applicable if the operator form of the field equations is potential (positive definite and self-adjoint). A numerical methodology presented in this study was applied for the analysis of viscoelastic structural members by Aköz and Kadıoğlu [36] and Kadıoğlu and Aköz [37-39]. In these studies, MFE formulations of viscoelastic parabolic and circular beams were derived based on the Gâteaux Differential method. Moreover, the proposed solution procedure was successfully applied to the analysis of viscoelastic Kirchhoff plates constituted by different rheological models by Aköz et al. [40] and to the analysis of Mindlin-Reissner plates made of viscoelastic materials based on the shear deformation theory by Tekin and Kadıoğlu [41].

2. METHOD

2.1. Winkler Elastic Foundation

In the Winkler foundation model, the relevance between the external pressure q_0 and the deflection of the foundation surface parallel to the z-axis w (Fig. 1) is given by:

$$q_k = k\,w \tag{1}$$

Here, k is the modulus of subsoil response of foundation. When applied to laterally loaded plates, the mathematical model for the plate-elastic foundation interaction system yields a biharmonic differential equation as:

$$D\,\nabla^4 w + kw = q_0 \tag{2}$$

Here, D indicates the bending stiffness of the plate and ∇^4 indicates a biharmonic operator:

$$\nabla^4 = \frac{\partial^4}{\partial x^4} + 2\frac{\partial^4}{\partial x^2 \partial y^2} + \frac{\partial^4}{\partial y^4} \tag{3}$$

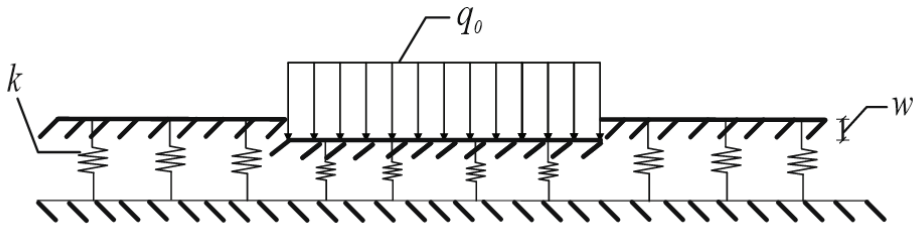

Fig. 1 - Winkler foundation model

2.2. Viscoelastic Plate - Winkler Elastic Foundation Coupling

The governing equations of plates made of viscoelastic materials were derived in Laplace-Carson space by [40] using the Kirchhoff plate theory with internal forces of which their positive directions are depicted in Fig. 2.

The Laplace-Carson transform $\bar{g}(r)$ of a function $g(t)$ with respect to time is defined by

$$\bar{g}(r) = r \int_0^\infty e^{-rt}\, g(t)\, d\,t \tag{4}$$

Here, r is the parameter of the Laplace transform, which is in general a complex number. Implementation of the Laplace-Carson transform with regard to time in field equations to remove time derivatives yields the following field equations in terms of four variables in the Laplace-Carson space, including the bending and twisting moments ($\overline{M}_x, \overline{M}_y, \overline{M}_{xy}$) and a component of displacement ($\overline{w}$) shown as follows:

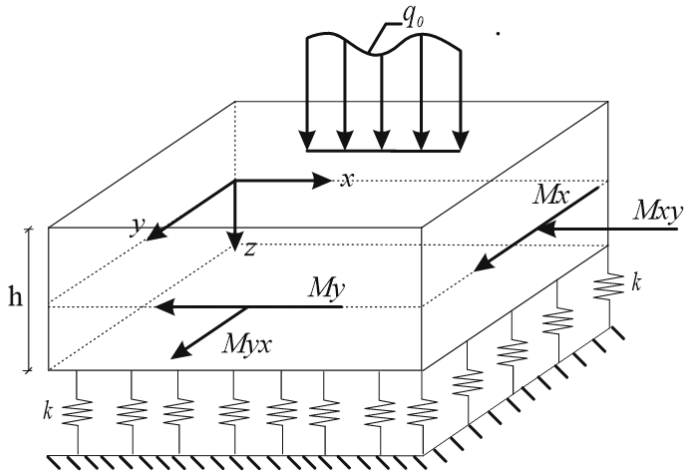

Fig. 2 - Internal forces of laterally loaded plate structure

$$
\begin{aligned}
-\frac{\partial^2 \bar{M}_x}{\partial x^2} - \frac{\partial^2 \bar{M}_y}{\partial y^2} - 2\frac{\partial^2 \bar{M}_{xy}}{\partial x \partial y} &= \bar{q}_0 - k\bar{w} \\
-\bar{M}_x - \bar{D}^*\left(\frac{\partial^2 \bar{w}}{\partial x^2} + \nu \frac{\partial^2 \bar{w}}{\partial y^2}\right) &= 0 \\
-\bar{M}_y - \bar{D}^*\left(\frac{\partial^2 \bar{w}}{\partial y^2} + \nu \frac{\partial^2 \bar{w}}{\partial x^2}\right) &= 0 \\
-\bar{M}_{xy} - (1-\nu)\,\bar{D}^* \frac{\partial^2 \bar{w}}{\partial x \partial y} &= 0
\end{aligned}
\tag{5}
$$

Here, q_0 is the wave-type load distribution, ν is Poisson's ratio of the plate and $D^*$is the operator form of the plate's flexural rigidity, which is defined for plates in the hereditary integral form. More information can be found from [40 and 42].

Field equations of VEPs - Winkler foundation interaction problem with the boundary conditions in the Laplace-Carson domain can be shown in operator form as:

$$\bar{Q} = \bar{L}\bar{\mathrm{v}} - \bar{f} \tag{6}$$

$$
\begin{bmatrix}
k & \bar{P}_{12} & \bar{P}_{13} & \bar{P}_{14} & 0 & 0 & 0 & 0 \\
\bar{P}_{21} & \bar{P}_{22} & \bar{P}_{23} & 0 & 0 & 0 & 0 & 0 \\
\bar{P}_{31} & \bar{P}_{32} & \bar{P}_{33} & 0 & 0 & 0 & 0 & 0 \\
\bar{P}_{41} & 0 & 0 & \bar{P}_{44} & 0 & 0 & 0 & 0 \\
0 & 0 & 0 & 0 & 0 & 0 & 0 & 1 \\
0 & 0 & 0 & 0 & 0 & 0 & -1 & 0 \\
0 & 0 & 0 & 0 & 0 & 1 & 0 & 0 \\
0 & 0 & 0 & 0 & -1 & 0 & 0 & 0
\end{bmatrix}
\begin{bmatrix}
\bar{w} \\ \bar{u}_2 \\ \bar{u}_3 \\ \bar{u}_4 \\ \bar{w}_0 \\ \bar{w}_0{}' \\ \bar{M} \\ \bar{T}
\end{bmatrix}
=
\begin{bmatrix}
\bar{q}_0 \\ 0 \\ 0 \\ 0 \\ \hat{\bar{T}} \\ -\hat{\bar{M}} \\ \hat{\bar{w}}' \\ -\hat{\bar{w}}
\end{bmatrix}
\tag{7}
$$

where

$$\begin{aligned}
\bar{P}_{12} &= -\bar{D}\left(\frac{\partial^2}{\partial x^2}+\nu\frac{\partial^2}{\partial y^2}\right)\\
\bar{P}_{13} &= -\bar{D}\left(\frac{\partial^2}{\partial y^2}+\nu\frac{\partial^2}{\partial x^2}\right)\\
\bar{P}_{14} &= -\bar{D}(1-\nu)\frac{\partial^2}{\partial x\,\partial y}\\
\bar{P}_{22} &= \bar{P}_{33} = -\bar{D}\\
\bar{P}_{23} &= \bar{P}_{32} = -\nu\bar{D}\\
\bar{P}_{44} &= -\frac{1}{2}\bar{D}(1-\nu)\\
\bar{u}_2 &= \frac{\bar{M}_x-\nu\bar{M}_y}{\bar{D}(1-\nu^2)}\\
\bar{u}_3 &= \frac{\bar{M}_y-\nu\bar{M}_x}{\bar{D}(1-\nu^2)}\\
\bar{u}_4 &= \frac{2\bar{M}_{xy}}{\bar{D}(1-\nu)}
\end{aligned} \tag{8}$$

These are the matrix shape of the operators. Here $\bar{L}$ is the derivative operator, $\bar{v}$ is the variables and $\bar{f}$ is external loads in the Laplace-Carson space. $\bar{Q}$ is a potential and these inner products

$$< d\bar{Q}(\bar{v}, \bar{v}'), \bar{v}* >= < d\bar{Q}(\bar{v}, \bar{v}*), \bar{v}' > \tag{9}$$

must be equal [43] in which $d\bar{Q}(\bar{v}, \bar{v}')$ is the Gâteaux derivative of the operator $\bar{Q}$.

$$d\bar{Q}(\bar{v}, \bar{v}*) = \begin{bmatrix}
k\bar{w}^* - \frac{\partial^2 \bar{M}^*{}_x}{\partial x^2} - \frac{\partial^2 \bar{M}^*{}_y}{\partial y^2} - 2\frac{\partial^2 \bar{M}^*{}_{xy}}{\partial x \partial y}\\
-\bar{D}\left(\frac{\partial^2 \bar{w}^*}{\partial x^2}+\nu\frac{\partial^2 \bar{w}^*}{\partial y^2}\right) - \bar{M}^*{}_x\\
-\bar{D}\left(\frac{\partial^2 \bar{w}^*}{\partial y^2}+\nu\frac{\partial^2 \bar{w}^*}{\partial x^2}\right) - \bar{M}^*{}_y\\
-(1-\nu)\bar{D}\frac{\partial^2 \bar{w}^*}{\partial x \partial y} - \bar{M}^*{}_{xy}\\
\bar{T}^*\\
-\bar{M}^*\\
\bar{w}^{*\prime}\\
-\bar{w}^*
\end{bmatrix} \tag{10}$$

Thus, the functionals stand for the field equations which form the basis of finite element formulation can be found as (see, Oden and Reddy [43]):

$$I(\bar{v}) = \int_0^1 < \bar{Q}(\varphi\,\bar{v}, \bar{f}), \bar{v} > d\varphi \tag{11}$$

φ being a scalar. Finally, from Eq. (11), the explicit expression of the functional of the thin VEP-EF interaction problem in the Laplace-Carson space takes the form:

$$I(\bar{v}) = \frac{1}{2}k\,[\bar{w}, \bar{w}] + \left[\frac{\partial \bar{w}}{\partial x}, \frac{\partial \bar{M}_{xy}}{\partial y}\right] + \left[\frac{\partial \bar{w}}{\partial y}, \frac{\partial \bar{M}_{xy}}{\partial x}\right] - \frac{1}{2\bar{D}\,(1-\nu^2)}\{[\bar{M}_x, \bar{M}_x] + [\bar{M}_y, \bar{M}_y]\}$$
$$-[\bar{q}_0, \bar{w}] + \left[\frac{\partial \bar{M}_x}{\partial x}, \frac{\partial \bar{w}}{\partial x}\right] + \left[\frac{\partial \bar{M}_y}{\partial y}, \frac{\partial \bar{w}}{\partial y}\right] + \frac{\nu}{\bar{D}\,(1-\nu^2)}[\bar{M}_x, \bar{M}_y] - \frac{1}{\bar{D}\,(1-\nu)}[\bar{M}_{xy}, \bar{M}_{xy}] \quad (12)$$
$$-\left[\hat{\bar{T}}, \bar{w}\right]_\sigma - \left[\bar{w}', \left(\bar{M} - \hat{\bar{M}}\right)\right]_\sigma - [\hat{\bar{w}}', \bar{M}]_\varepsilon - [\bar{T}, (\bar{w} - \hat{\bar{w}})]_\varepsilon$$

The expressions in the square brackets with the subscripts σ and ε represent the boundary conditions which are classified into two types: dynamic and geometric boundary conditions, respectively. The explicit form of the boundary conditions of the problem can be written in the form:

$$[\bar{T}\,, \bar{w}] = \left[\left(\frac{\partial \bar{M}_x}{\partial x} + \frac{\partial \bar{M}_{xy}}{\partial y}\right) n_x + \left(\frac{\partial \bar{M}_y}{\partial y} + \frac{\partial \bar{M}_{xy}}{\partial x}\right) n_y, \bar{w}\right]$$
$$[\bar{M}\,, \bar{w}'] = \left[\bar{M}_x, \frac{\partial \bar{w}}{\partial x} n_x\right] + \left[\bar{M}_y, \frac{\partial \bar{w}}{\partial y} n_y\right] + \left[\bar{M}_{xy}, \left(\frac{\partial \bar{w}}{\partial x} n_y + \frac{\partial \bar{w}}{\partial y}\, n_x\right)\right] \quad (13)$$

The expression $[\bar{q}_0, \bar{w}]$ in Eq. (12) corresponds to:

$$[\bar{q}_0, \bar{w}] = \frac{1}{2}\rho\omega[\bar{w}, \bar{w}]$$

for dynamic analysis, where ω is the angular frequency.

The linear rectangular element that has a number of four nodes is constructed for the finite element analysis of the VEP-elastic foundation interaction problem. The interpolation functions of this element (Fig. 3), expressed in the (ξ, η) coordinates that are mere translations of (x, y), is given by [44]:

$$\Psi_i = \frac{1}{4}(1 + \xi\xi_i)(1 + \eta\eta_i) \qquad i = 1,2,3,4 \quad (14)$$

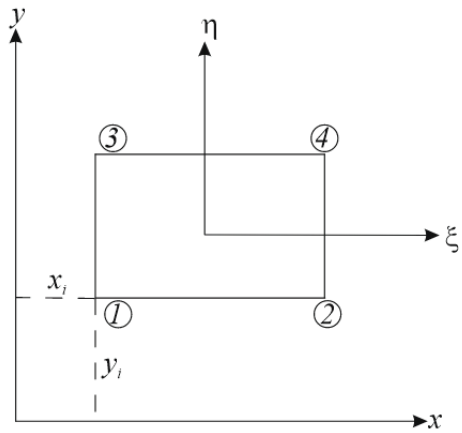

Fig. 3 - Rectangular element

A rectangular master element with four degrees of freedom with $\bar{w}$, $\bar{M}_x$, $\bar{M}_y$, $\bar{M}_{xy}$ as the nodal variables (the total degrees of freedom is 16) is denoted as the VPLTEF16 element.

All variables which must be carried as the primary nodal degrees of freedom, must be approximated by the given interpolation functions and they are inserted into Eq. (12). This functional is extremized with regard to sixteen nodal variables; thereby the sixteen element equations given by Eq. (15) are obtained for the thin VEP-EF interaction problem under wave-type loadings.

$$\begin{bmatrix} k[k_1] & [k_2] & [k_3] & [k_4] \\ [k_2] & -\frac{[k_1]}{\bar{D}(1-\nu^2)} & \frac{\nu[k_1]}{\bar{D}(1-\nu^2)} & 0 \\ [k_3] & \frac{\nu[k_1]}{\bar{D}(1-\nu^2)} & -\frac{[k_1]}{\bar{D}(1-\nu^2)} & 0 \\ [k_4] & 0 & 0 & -\frac{[k_1]}{2\bar{D}(1-\nu)} \end{bmatrix} \begin{bmatrix} \bar{w} \\ \bar{M}_x \\ \bar{M}_y \\ \bar{M}_{xy} \end{bmatrix} = \begin{bmatrix} [k_1]\ \bar{q}_0 \\ 0 \\ 0 \\ 0 \end{bmatrix} \qquad (15)$$

In Eq. (15), $[k_1]$, $[k_2]$, $[k_3]$ and $[k_4]$ are the submatrices.

3. ILLUSTRATIVE EXAMPLES AND DISCUSSION

A computer program has been written in the FORTRAN to perform the analyses. Numerical examples are considered for simply supported rectangular plate with the following geometrical properties:

- $\frac{a}{2} = \frac{b}{2} = 2\ m$ and thickness of plate h=0.1 m (see Fig. 4)

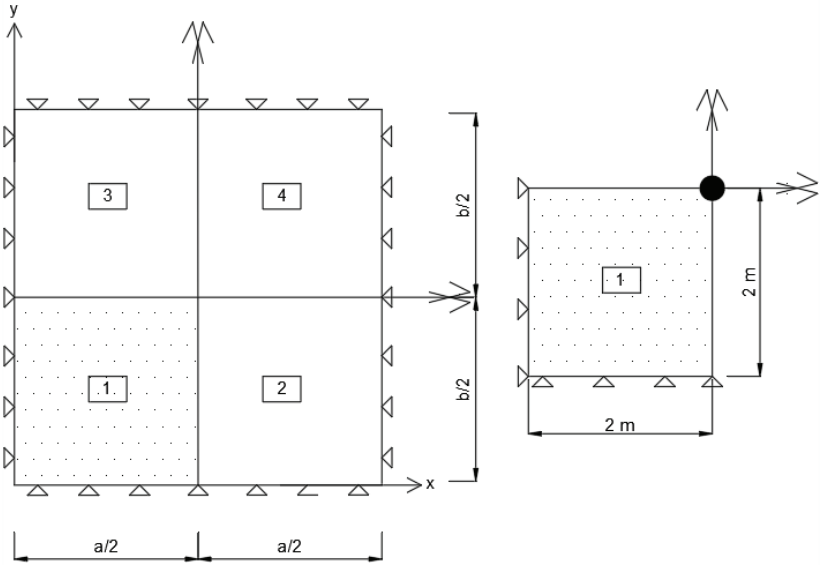

Fig. 4 - Symmetry property of simply supported rectangular plate

Due to the two-way symmetry, we can focus upon a quarter of the plate. The analyses were performed with a mesh size of 4x4. The time histories of wave-type loads considered in the analyses are shown in Fig. 5.

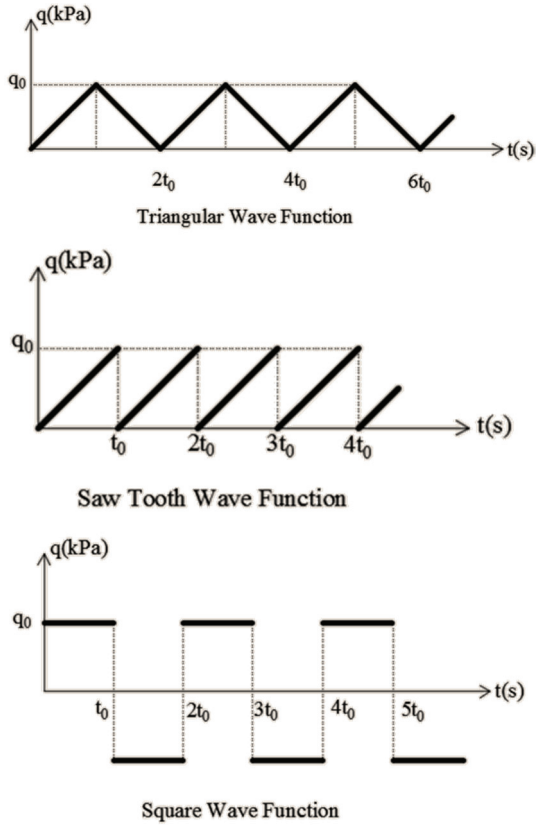

Fig. 5 - Wave-Type load distributions

For describing the viscoelastic behavior of plate material, all numerical examples are employed for the Zener rheological solid model. The Zener model illustrated in Fig. 6 is also known as the standard linear solid.

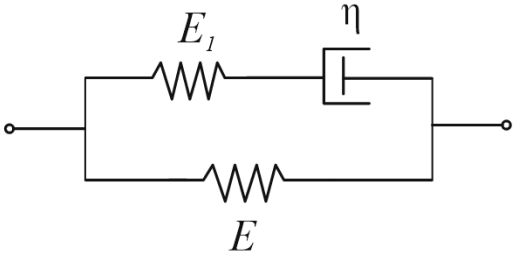

Fig. 6 - Mechanical analog for the Zener solid model

The creep compliance of the Zener solid model is expressed by:

$$J_{(t)} = \frac{1}{E}(1 - e^{-\alpha t}) + \frac{1}{E+E_1}(1 - e^{-\alpha t}) \quad , \qquad \alpha = \frac{E\,E_1}{\eta(E+E_1)} \tag{16}$$

The material properties are $E_1 = E = 98$ MPa, $\eta = 245$ MPa.s and $\nu = 0.3$. The solutions are transformed back to the time domain by using the D&A numerical ILTT technique. For more information about the D&A Laplace inversion process, the interested reader is referred to literature [45].

Example 1:

In this example, quasi-static analysis of a thin VEP subjected to triangular wave-type loading of 1000 N/m^2 considered for $t_0 = 2$ sec and time-varying displacement values at the mid-point of the plate are illustrated in Fig. 7 for different subgrade reactions (k =100 000 kN/m^3, 200 000 kN/m^3 and 300 000 kN/m^3). For numerical inversion, D&A ILTT is employed for aT=5, N=400 and T=20 sec. These results are quite reasonable and indicate that an increase in the value of the subgrade reaction results in the same rate decrease in the central displacement response.

In addition, dynamic and quasi-static response of a thin VEP with foundation interaction with stiffness k=100.000 kN/m^3 subjected to the same wave-type loading for t_0=4 sec is considered. The material density of the plate ρ is assumed to be 2400 kg/m^3. For numerical inversion, D&A ILTT is employed for aT=5, N=600 and T=30 sec. As expected, the VEP starts to vibrate about the quasi-static state but it never approaches the quasi-static state with time when it is subjected to harmonic loading like triangular wave-type loading as depicted in Fig. 8.

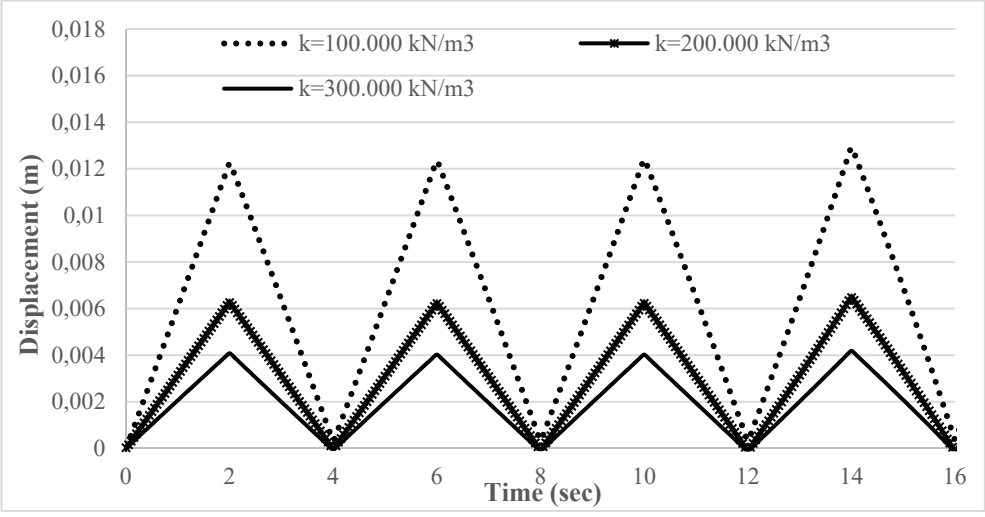

Fig. 7 - Quasi-static central displacement response of viscoelastic thin plate with elastic foundation interaction under triangular wave-type loading

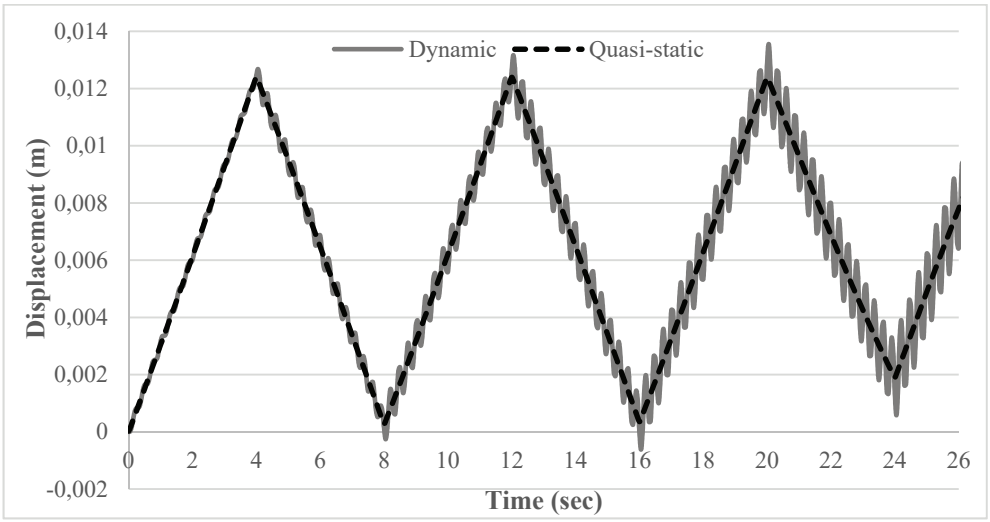

Fig. 8 - Dynamic and Quasi-static central displacement response of viscoelastic thin plate with elastic foundation interaction under triangular wave-type loading

Example 2:

In this example, quasi-static and dynamic analyses of thin VEPs on elastic foundation with stiffness k=100.000 kN/m^3 and subjected to saw tooth wave-type loading of 1000 N/m^2 is considered for t_0=4 sec. The problem is solved by the variation of the central displacement and the results are demonstrated in Fig. 9.

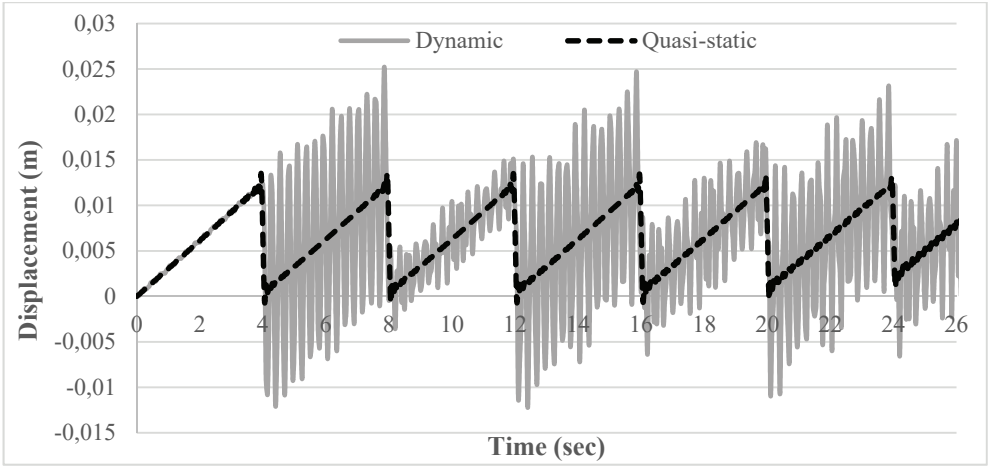

Fig. 9 - Central displacement versus time results under saw tooth wave-type loading

For the numerical inversion, the D&A transform technique is used for ρ=2400 kg/m^3, aT=5, N=600 and T=30 sec. The longer loading time t_0, the springback of the plate is much slower after unloading due to the fact that the dissipation of energy of the plate is more and more, whereas the strain energy stored is less and less with the increment of loading time.

Example 3:

As an example, a thin VEP with no foundation interaction is considered. Two different plate thicknesses are considered. The numerical results are presented in Fig. 10 for central displacement variation with time under the square wave-type loading for t_0= 2 sec. The same material properties as in the previous example are considered. For numerical inversion, the D&A ILTT for aT=5, N=400 and T=20 sec is considered. As expected, the vibration period and displacement of the VEP reduces as the thickness of the plate increases.

Example 4:

In this example, bending moment (M_x) and displacement variation at the mid- point of the thin VEP on the EF with stiffness k=100.000 kN/m^3 subjected to a square wave-type loading (t_0=4 sec) with the amplitude q_0=1000 N/m^2 are investigated. In Fig. 11, quasi-static and dynamic bending moment (M_x) and vertical displacement (w) responses are presented by employing D&A ILTT for aT=5, N=600 and T=30 sec. The same material properties given in the previous example are considered.

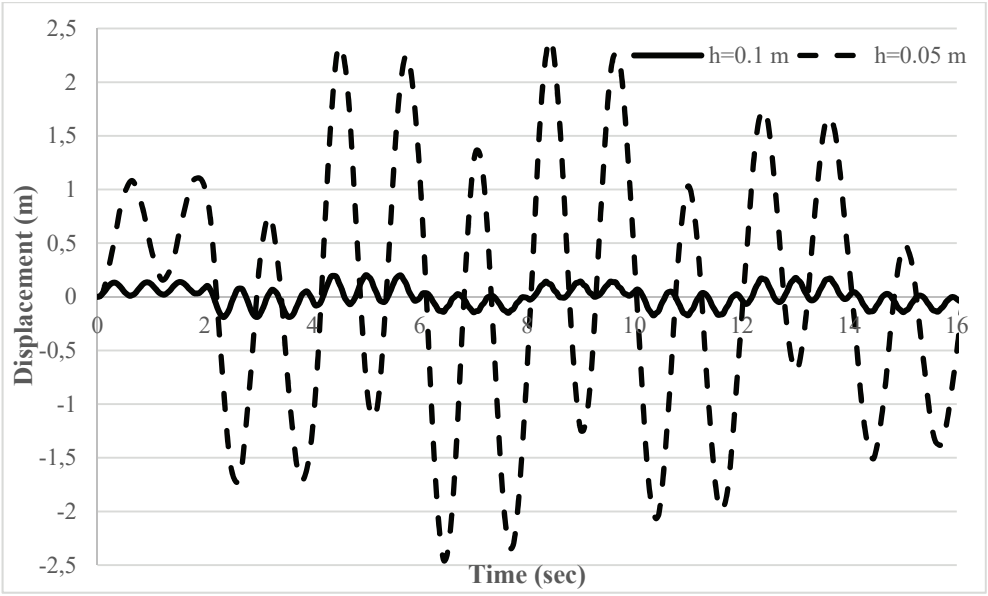

Fig. 10 - Influence of the plate thickness on displacement and vibration period of the viscoelastic thin plate without foundation interaction

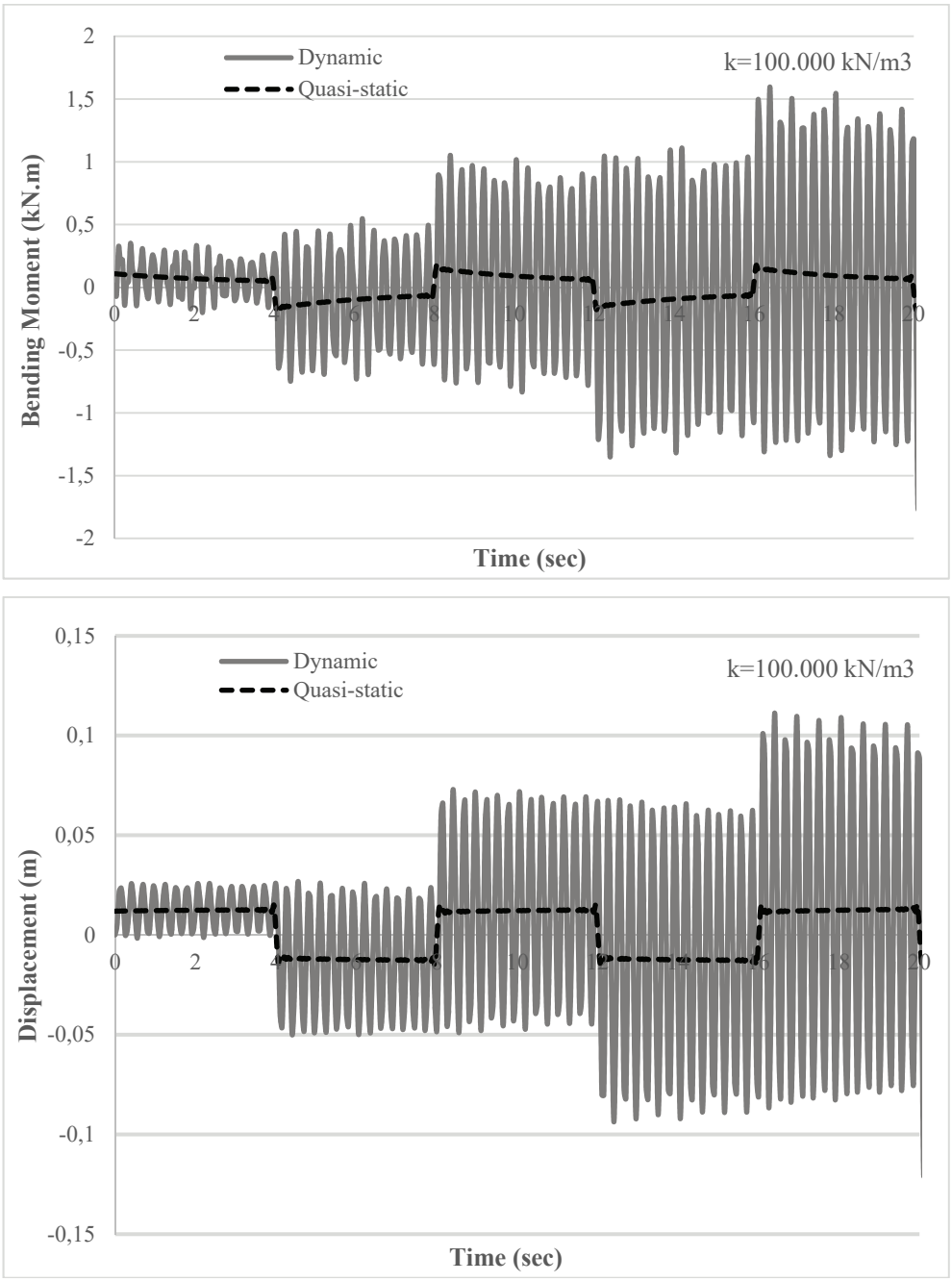

Fig. 11 - Dynamic and Quasi-static central bending moment and displacement responses of viscoelastic thin plate with foundation interaction subjected to square wave-type loading

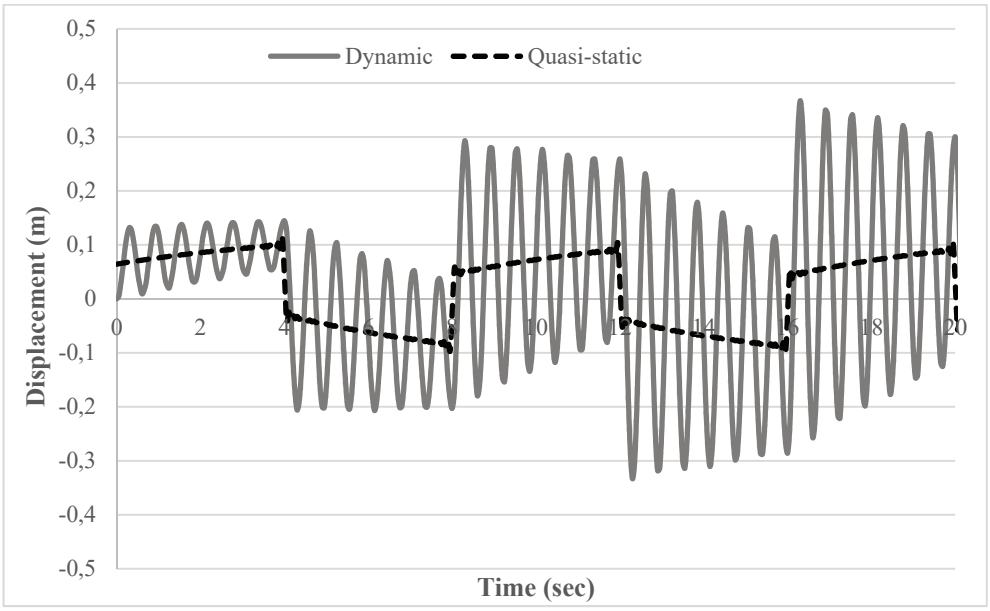

Fig. 12 - Dynamic and Quasi-static central displacement response of viscoelastic thin plate without foundation interaction subjected to square wave-type loading

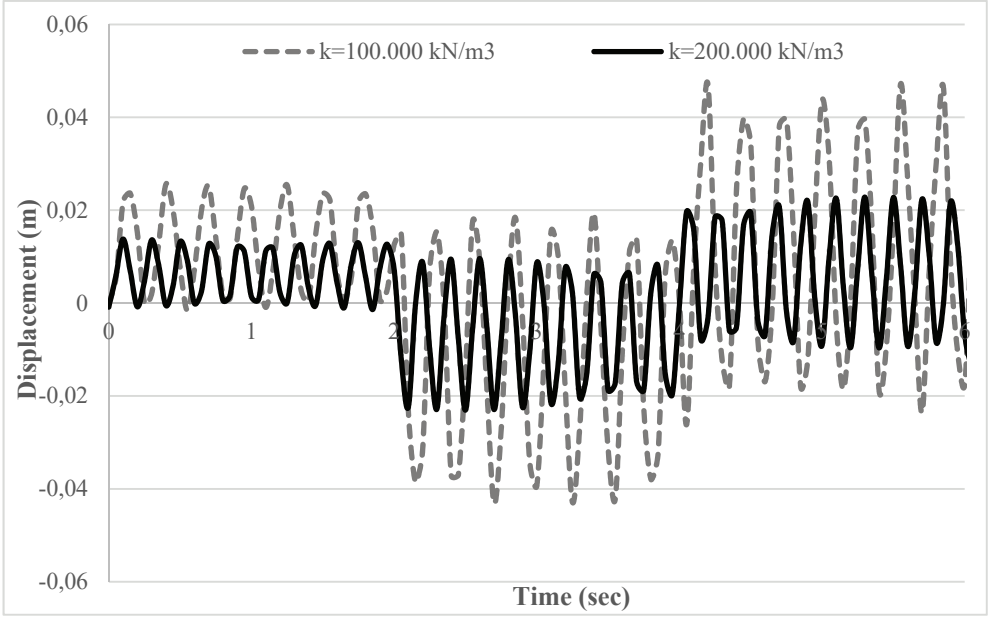

Fig.13 - Dynamic central displacement response of viscoelastic thin plate under square wave-type loading for different Winkler coefficients

Moreover, in Fig. 12, quasi-static and dynamic displacement responses of the plate without foundation interaction are presented in order to make comparison and provide quantitative information about the plate response in the absence and presence of elastic foundation interaction. It can be seen that the frequency of vibration is seriously influenced due to the interaction of the plate with the foundation.

Example 5:

In this problem, the dynamic response of thin VEP on the EF with different subgrade reaction constants (k=100.000 kN/m^3 and 200.000 kN/m^3) is considered. The problem is solved under the square wave-type loading for t_0=2 sec employing D&A ILTT for aT=5 and N=400 and T=20 sec. The same material properties as in the previous example are considered and the variation of displacement at the plate mid-point is given for different values of foundation stiffness in Fig. 13. Again, it is observed that the frequency of vibration is seriously influenced due to the variation of foundation stiffness parameter (k) and it increases when the foundation parameter (k) increases.

4. CONCLUSION

A proposal is presented of a simple numerical analysis method for the dynamic behavior of thin VEP- EF interaction problem under different wave-type loadings by utilizing the functional via a methodical procedure depending on the Gâteaux Differential. The functional and MFE formulation derived for the analysis are in the Laplace-Carson domain and for numerical transformation of the solutions back to the time domain, D&A ILTT is utilized. The analyses are performed with the aid of a FORTRAN code. The performance of the proposed methodology is tested through illustrative examples.

The results are quite reasonable:

i. An increase in the value of the subgrade reaction results in the same rate decrease in the central displacement response and the VEP starts to vibrate about the quasi-static state but it never approaches the quasi-static state with time as expected.

ii. The dynamic behavior of (un)constrained VEP is obtained by the proposed formulation. As expected, the frequency of vibration is seriously influenced due to the interaction of the plate with the foundation and it increases when the foundation parameter (k) increases.

iii. VEPs with different thickness values are analyzed. As expected, the vibration period and displacement of the VEP decreases as the thickness of the plate increases.

iv. Moments can be obtained directly without any mathematical operation by using this new functional, because it can be defined as one of the independent variables in the functional.

For further analysis stages, the behavior of viscoelastic structural members such as laminated composite beams according to different beam theories, shell structures and viscoelastic higher order shear deformation plate structures is planned to be investigated through this methodology.

References

[1] Pasternak, P.L.: On a New Method of Analysis of an Elastic Foundation by Means of Two Foundation Constants. Gosstroyizdat, Moscow (1954).

[2] Vlasov, V.Z., Leontiev, U.N.: Beams, Plates, and Shells on Elastic Foundations. Israel Program for Scientific Translations, Jerusalem (translated from Russian) (1966).

[3] Wang, Y.H., Tham, L.G., Cheung, Y.K.: Beams and plates on elastic foundations: a review. Prog. Struct. Eng. Mater. 7:174-182 (2005) https://doi.org/10.1002/pse.202.

[4] Kerr, A.D.: Elastic and viscoelastic foundation models. J. Appl. Mech. 31:491-498 (1964) https://doi.org/10.1115/1.3629667.

[5] Cheung, Y.K., Zienkiewicz, O.C.: Plates and tanks on elastic foundations-an application of finite element method. Int. J. Solids Struct. 1:451- 461 (1965) https://doi.org/10.1016/0020-7683(65)90008-9.

[6] Dowell, E.H.: Dynamic analysis of an elastic plate on a thin, elastic foundation. J. Sound Vib. 35:343-360 (1974) https://doi.org/10.1016/0022-460X(74)90065-0.

[7] Katsikadelis, J.T., Armenakas, A.E.: Plates on elastic foundation by BIE method. J. Eng. Mech. 110:1086-1105 (1984) https://doi.org/10.1061/(ASCE)0733-9399(1984)110:7(1086).

[8] El-Zafrany, A., Fadhil, S., Al-Hosani K.: A new fundamental solution for boundary element analysis of thin plates on Winkler foundation. Int. J. Numer. Methods Eng. 38:887-903(1995). https://doi.org/10.1002/nme.1620380602.

[9] Sladek, J., Sladek, V., Mang, H.A.: Meshless local boundary integral equation method for simply supported and clamped plates resting on elastic foundation. Comput. Methods Appl. Mech. Eng. 191:5943-5959 (2002) https://doi.org/10.1016/S0045-7825(02)00505-4.

[10] Zhong, Y., Zhang, Y-S.: Theoretic solution of rectangular thin plate on foundation with four edges free by symplectic geometry method. Appl. Math. Mech. (English Edition). 27: 833-839 (2006) https://doi.org/10.1007/s10483-006-0614-y.

[11] Yang, Z., Yuan-Yuan, G., Fangin, B-B.: Solution for a rectangular plate on elastic foundation with free edges using reciprocal theorem method. Math. AEterna. 2:335-343 (2012).

[12] Rahbar-Ranji, A., Bahmyari, E.: Bending analysis of thin plates with variable thickness resting on elastic foundation by element free Galerkin method. J. Mech. 28:479-488 (2012) https://doi.org/10.1017/jmech.2012.57.

[13] Kägo, E., Lellep, J.: Free Vibrations of Plates on Elastic Foundation, Procedia Eng. 57:489-496 (2013) https://doi.org/10.1016/j.proeng.2013.04.063.

[14] Li, R., Zhong, Y., Li, M.: Analytic bending solutions of free rectangular thin plates resting on elastic foundations by a new symplectic superposition method. Proc. Royal Society A 469:20120681 (2013) https://doi.org/10.1098/rspa.2012.0681.

[15] Flügge, W.: Viscoelasticity (Second Ed.). Springer, Berlin (1975).

[16] Christensen, R.M.: Theory of Viscoelasticity (Second Ed.). Academic Press, New York (1982).

[17] White, J.L.: Finite elements in linear viscoelastic analysis. In: Proceedings of the 2nd Conference on Matrix Method in Structural Mechanics. AFFDL-TR-68-150: 489-516 (1986).

[18] Wang, Y.Z., Tsai, T.J.: Static and dynamic analysis of a viscoelastic plate by the finite element method. Appl. Acoust. 25:77-94 (1988) https://doi.org/10.1016/0003-682X(88)90017-5.

[19] Chen, T-M.: The hybrid Laplace transform / finite element method applied to the quasi-static and dynamic analysis of viscoelastic Timoshenko beams. Int. J. Numer. Methods Eng. 38:509-522 (1995) https://doi.org/10.1002/nme.1620380310.

[20] Sorvari, J., Hämäläinen, J.: Time integration in linear viscoelasticity-a comparative study. Mech. Time-Depend. Mater. 14:307-328 (2010) https://doi.org/10.1007/s11043-010-9108-7.

[21] Zhou, X., Yu, D., Shao, X., Zhang, S., Wang, S.: Research and applications of viscoelastic vibration damping materials: A review. Compos. Struct. 136:460-480 (2016) https://doi.org/10.1016/j.compstruct.2015.10.014.

[22] Zhang, C., Zhu, H., Shi, B., Liu, L.: Theoretical investigation of interaction between a rectangular plate and fractional viscoelastic foundation. J. Rock Mech. Geotech. Eng. 6:373-379 (2014) https://doi.org/10.1016/j.jrmge.2014.04.007.

[23] Van, H.L, Thoi, T.N, Liu, G.R., Van, P.P.: A cell-based smoothed finite element method using three-node shear-locking free Mindlin plate element (CS-FEM-MIN3) for dynamic response of laminated composite plates on viscoelastic foundation. Eng. Anal. Bound. Elem. 42:8-19 (2014) https://doi.org/10.1016/j.enganabound.2013.11.008.

[24] Hasheminejad, S.M., Gheshlaghi, B.: Three-dimensional elastodynamic solution for an arbitrary thick FGM rectangular plate resting on a two parameter viscoelastic foundation. Compos. Struct. 94:2746-2755(2012) https://doi.org/10.1016/j.compstruct.2012.04.010.

[25] Çalık Karaköse, Ü.H.: FE analysis of FGM plates on arbitrarily orthotropic Pasternak foundations for membrane effects. Teknik Dergi. 33:11799-11822 (2022) https://doi.org/10.18400/tekderg.878982

[26] Gupta, A., Talha, M., Seemann, W.: Free vibration and flexural response of functionally graded plates resting on Winkler–Pasternak elastic foundations using nonpolynomial higher-order shear and normal deformation theory. Mech. Adv. Mater. Struct. 25:523-538(2018) https://doi.org/10.1080/15376494.2017.1285459.

[27] Özgan, K.: Modelling laminated orthotropic plate-foundation interaction subjected to moving load using Vlasov model. Teknik Dergi. 29: 8317-8338 (2018) https://doi.org/10.18400/tekderg.339219

[28] Gupta, A., Talha, M., Chaudhari, V.K.: Natural frequency of functionally graded plates resting on elastic foundation using finite element method. Proc. Technol. 23:163-170(2016). https://doi.org/10.1016/j.protcy.2016.03.013.

[29] Zenkour, A.M., Allam, M.N.M., Sobhy, M.: Bending of a fiber-reinforced viscoelastic composite plate resting on elastic foundations. Arch. Appl. Mech. 81:77-96(2011). https://doi.org/10.1007/s00419-009-0396-9.

[30] Daikh, A.A., Zenkour, A.M.: Bending of functionally graded sandwich nanoplates resting on Pasternak foundation under different boundary conditions. J. Appl. Comput. Mech. 6:1245-1259(2020). https://doi.org/10.22055/JACM.2020.33136.2166.

[31] Zenkour, A.M., Sobhy, M.: Thermal buckling of functionally graded plates resting on elastic foundations using the trigonometric theory. J. Therm. Stresses. 34:1119-1138(2011). https://doi.org/10.1080/01495739.2011.606017.

[32] Tabasi, H.M., Jam, J.E., Fard, K.M., Beni, M.H.: Buckling and free vibration analysis of fiber metal-laminated plates resting on partial elastic foundation J. Appl. Comput. Mech. 6:37-51(2020). https://doi.org/10.22055/JACM.2019.28156.1489

[33] Zamani, H.A., Aghdam, M.M., Sadighi, M.: Free vibration analysis of thick viscoelastic composite plates on visco-Pasternak foundation using higher-order theory. Compos. Struct. 182:25-35 (2017) https://doi.org/10.1016/j.compstruct.2017.08.101.

[34] Sofiyev, A.H., Zerin, Z., Kuruoglu, N.: Dynamic behavior of FGM viscoelastic plates resting on elastic foundations. Acta Mech. 231:1-17 (2020) https://doi.org/10.1007/s00707-019-02502-y.

[35] Khazanovich, L., Levenberg, E.: Analytical solution for a viscoelastic plate on a Pasternak foundation. Road Mater. Pavement Des. 21:800-820 (2020) https://doi.org/10.1080/14680629.2018.1530693.

[36] Aköz, A.Y., Kadıoğlu, F.: The mixed finite element method for the quasi-static and dynamic analysis of viscoelastic Timoshenko beams. Int. J. Numer. Methods Eng. 44:1909-1932 (1999) https://doi.org/10.1002/(SICI)1097-0207(19990430)44:12<1909::AID-NME573>3.0.CO;2-P.

[37] Kadıoğlu, F., Aköz, A.Y.: The mixed finite element method for the dynamic analysis of visco-elastic circular beams. In: Proceedings of the 4 th International Conference on Vibration Problems. Jadavpur University (1999).

[38] Kadıoğlu, F., Aköz, A.Y.: The quasi-static and dynamic responses of viscoelastic parabolic beams. In: Proceedings of the 11 th National Applied Mechanics Meeting (in Turkish), Bolu-Turkey (2000).

[39] Kadıoğlu, F., Aköz, A.Y.: The mixed finite element for the quasi-static and dynamic analysis of viscoelastic circular beams. Int. J. Struct. Eng. Mech. 15: 735-752 (2003) https://doi.org/10.12989/sem.2003.15.6.735.

[40] Aköz, A.Y., Kadıoğlu, F., Tekin, G.: Quasi-static and dynamic analysis of viscoelastic plates. Mech. Time-Depend. Mater. 19:483-503(2015) https://doi.org/10.1007/s11043-015-9274-8.

[41] Tekin, G., Kadıoğlu, F.: Viscoelastic behavior of shear-deformable plates. Int. J.Appl. Mech. 9:1750085 (23 pages) (2017) https://doi.org/10.1142/S1758825117500855.

[42] Ilyasov, M.H., Aköz, A.Y.: The vibration and dynamic stability of viscoelastic plates. Int. J.Eng. Sci. 38: 695-714 (2000) https://doi.org/10.1016/S0020-7225(99)00060-9.

[43] Oden, J.T., Reddy, J.N.: Variational Methods in Theoretical Mechanics. Springer, Berlin (1976).

[44] Reddy, J.N.: An Introduction to the Finite Element Method (Second Ed.). McGraw-Hill, New York (1993).

[45] Dubner, H., Abate, J.: Numerical inversion of Laplace transforms by relating them to the finite Fourier cosine transform. J. ACM. 15:115-123 (1968) https://doi.org/10.1145/321439.321446.

Turkish Journal of Civil Engineering, 2023, 99-128, Paper 753, ***Research Article***

Effects of Flow Unsteadiness on the Transport of Bimodal Bed Material

Gokcen BOMBAR[1]
Aysegul OZGENC AKSOY[2*]
Mehmet Sukru GUNEY[3]

ABSTRACT

The grain size distribution of the bed load was experimentally investigated under unsteady flow conditions with bimodal mixture of sand and gravel in a laboratory flume. Five various triangular hydrographs were generated. A clockwise behavior for the total bed load versus shear velocity was observed meaning that the bed load during rising limb was higher than that of falling limb. It was found that the percent finer at the plateau of bimodal sediment size distribution curve had higher values during the initial and final phases compared to those obtained during the peak time. At all plateaus, the percent finer values related to the hydrograph peak discharge were in the same order of magnitude with that of the bed material. The sand content of the transported bed material initially decreased, then maintained a constant value during a certain time interval and finally returned to its original value. The sand percent of the bed load decreased in the falling limb showing a counterclockwise loop and within the limits of the experimental campaign, the duration of the hydrograph did not affect the results considerably. Greater peak flow rate of the hydrograph resulted in greater hysteresis. The bimodality index was calculated for all transported sediment samples and it was revealed that its initial and final values were less than that of the bed material but it was approximately the same elsewhere. The 5% finer sediment amount was nearly equal during rising and falling limbs. It was revealed that D_{50} value of the bed load decreased in the rising limb showing a clockwise loop. The hysteresis was not considerably changed according to the hydrograph characteristics. The clockwise type hysteresis was also observed for the size group of D_{95}. The lag increased as the peak flow rate increased. A strong relation was found between the dimensionless total bed load W_t* and the total work index W_k as well as W_k and the ratio W_R/W_F. The correlations between the dimensionless total bed load and the

Note:
- This paper was received on December 29, 2022 and accepted for publication by the Editorial Board on September 4, 2023.
- Discussions on this paper will be accepted by January 31, 2024.
- https://doi.org/10.18400/tjce.1226516

1 İzmir Katip Çelebi University, Department of Civil Engineering, Izmir, Türkiye
gokcen.bombar@ikcu.edu.tr - https://orcid.org/0000-0002-8156-6908

2 Dokuz Eylül University, Department of Civil Engineering, Izmir, Türkiye
aysegul.ozgenc@deu.edu.tr - https://orcid.org/0000-0001-8779-5499

3 İzmir Ekonomi University, Department of Civil Engineering, Izmir, Türkiye
sukru.guney@ieu.edu.tr - https://orcid.org/0000-0003-1441-4784

* Corresponding author

unsteadiness parameters P, and P_{mod} were very weak, whereas a quite high value of determination coefficient was obtained with the unsteadiness parameter P_{gt}, implying an appreciable interdependence.

Keywords: Unsteady flow, mixed gravel and sand, bimodal sediment, bed load, unsteadiness parameter, hysteresis.

1. INTRODUCTION

The wide range of grain sizes found in most rivers, especially rivers with gravel bed, complicates the problem of the prediction of bedload transport rate. The grain size influences sediment transport and when the sediment bed is a mixture of different grain sizes, the relative size effects become important (Wilcock, 1993, 2001; Wilcock et al, 2001, Wilcock and Kenworthy, 2002). This effect is very sensitive to the composition of the mixture (Houssais and Lajeunesse 2012).

A gravel-bed river has bed material whose characteristic size is in the range of gravel or coarser material. The grain size distributions of most streams show bimodal characteristic. Their particle size distributions are described by a bimodal distribution, i.e. a distribution with two distinct peaks in the frequency distribution, one in the finer and other in the coarser fraction (Sambrook Smith et al. 1996, Müller et al, 2008). Such streams exhibit both sand and gravel modes.

In this study significant quantities of both gravel and sand are present. Studies related to bimodal sediments have been focused on their origin, spatial extent and, more recently, the processes occurring within them. Bimodality may occur readily and be spatially widespread. Bimodal beds may represent a distinct threshold between gravel- and sand-bed states (Sambrook Smith 1996). Since the rivers are often characterized as strongly bimodal (Parker, 2008) it is appropriate to further study the transport of bimodal sediments in order to understand the surface sorting, downstream fining and morphology and ecology of streams. As an example, Tian and Wang (2009) explored the effect of bimodal sediment distribution and its relation with the river ecology in the Dadu river basin by field investigations. The transport and sorting are particularly important in unsteady flows.

Various studies have examined bedload transport under unsteady flow conditions, particularly in the case of uniform sediment. For example, Reid et al. (1985) observed point-bars and associated scour pools at meanders during floods, with no well-developed bed forms at straight reaches. Kuhnle (1992) found that bedload transport rates were higher during the rising limb at high flows, while transport rates were higher during the recession limb at low flows. Qu (2002) observed a time lag between friction velocity and bedload transport, with flow unsteadiness affecting the lag. Lee et al. (2004) investigated bedload transport in a recirculating tilting flume and found that the total yield during the falling period was higher than during the rising period with a counterclockwise hysteresis.

Other studies have focused on mixed sediment beds under unsteady flow conditions. Saadi (2008) examined the stability of mixed bimodal grain sediment beds exposed to different durations of uniform antecedent flow hydrographs and found that longer exposure time increased bed stability. Bombar et al. (2011) investigated the dynamic behavior of sediment transport and proposed an unsteadiness parameter based on net acceleration. Güney et al. (2013) studied the effect of coarse surface development on the bimodal bed-load transport

under unsteady flow conditions. Mao (2012) analyzed sediment transport dynamics during different hydrographs and found that transport during the falling limb was lower than during the rising limb. Wang et al. (2013) studied the transport of bedload mixtures with different grain size distributions and found that coarser fractions reached peak transport rate during the rising limb, while finer fractions reached peak transport rate during the falling limb. Wang et al. (2014) revealed that coarser fractions reached their peak transport rate during the rising limb, while finer fractions typically reached their peak transport rate during the falling limb, which was attributed, at least in part, to the role of sub-threshold, antecedent base flow conditions in restructuring the bed surface grading. Later Wang et al. (2015) indicated that the unimodal sediment bed was inherently more stable than the bimodal bed due to the increased abundance of medium-sized gravels present in the unimodal sediment grade.

The effect of sediment composition on sediment transport in unsteady flow conditions has also been studied. Waters and Curran (2015) found that bedload yields were larger and more variable for sand/silt mixtures compared to sand/gravel mixtures. Tabarestani and Zarrati (2015) suggested that methods based on steady flow conditions underestimate sediment transport rates in unsteady flows and recommended further research on the effect of non-uniform stream bed composition. Gunsolos and Binns (2017) reviewed studies on sediment transport in unsteady flow conditions and emphasized the importance of sediment transport mode and composition in determining hysteresis patterns. Mrokowska and Rowinski (2019) summarized the impact of flow properties and sediment attributes on bedload transport and highlighted the need to quantify the effect of kinematic sieving in multi-modal sediment during flood events. Yarnell et al. (2016) tracked the movement of tracer grains in a gravel-bedded stream and found that larger storms moved a greater percentage of tracers downstream, with no significant variation in grain size distribution between storms. Li et al. (2018) investigated sediment transport under degrading channels and found that sand promoted the transport of gravel, while gravel hindered the transport of sand, with the effect being more pronounced at lower discharges and weakened by flow unsteadiness. Mao (2018) simulated hydrographs as a sequence of events and explored the effect of different antecedent conditions on sediment transport. Their results showed a low-magnitude antecedent event did not affect the rate of sediment transported by a subsequent high-magnitude flood, but a high-magnitude antecedent event reduced the sediment transported by a subsequent long-duration/low-magnitude event. Perret et al. (2018) studied the effect of multimodal sediment composition and the infiltration of fine sediment into the gravel matrix. Khosravi et al. (2019) evaluated the transport of uniform and graded sediment mixtures and found that the transport rate differed for fine and coarse fractions, with coarser fractions exhibiting higher mobility during the rising limb and finer fractions during the falling limb. Duan et al. (2020) compared bedload transport under steady and unsteady flow conditions and found that sediment particles were easier to transport under unsteady flow and moved greater distances. Plumb et al. (2020) observed hysteresis loops in both total and fractional transport, with longer duration hydrographs exhibiting more pronounced loops. Wang et al. (2021a, b) generated symmetrical hydrograph flows over a graded sediment bed and found that coarse size fractions exhibited clockwise hysteresis, while fine transported material showed counterclockwise hysteresis.

The hydrographs can be characterized by various parameters. The total flow work index, W_k is expressed as follows (Lee et al, 2004):

$$W_k = \frac{{u_{*0}}^2 V_{ol}}{g h_b^3 b} \tag{1}$$

where u_{*0} is the shear velocity of the base flow at the upstream end, V_{ol} is the total volume of water under the hydrograph (excluding the base flow), g is the gravitational acceleration, h_b is the initial flow depth (base flow) and b is the channel width.

The dimensionless total bed load W_t^* is expressed as (Bombar et al, 2011, Gumgum and Guney, 2021, Przyborowski et al, 2022):

$$W_t^* = \frac{W_t}{\rho_s b D_{50}^2} \tag{2}$$

where W_t is total bed load, and ρ_s is density of the sediment. W_t^* is used also in scour studies under live bed conditions.

The unsteadiness character of the flow was investigated through various dimensionless parameters. Lee et al. (2004) proposed the following unsteady flow parameter P

$$P = \frac{h_p - h_b}{t_d u_{*0}} \tag{3}$$

where h_p and t_d denote the flow depth corresponding to the peak flowrate and the total duration of the hydrograph, respectively.

The unsteady flow parameter suggested by De Sutter et al. (2001) is:

$$P_{\text{mod}} = \frac{h_p - h_b}{t_r \left[\left(u_b + u_p\right)/2\right]} \frac{{u_{*p}}^2 - {u_{*cr}}^2}{{u_{*cr}}^2} \tag{4}$$

where u_{*p} is the shear velocity at peak flow and u_{*cr} is the critical shear velocity, u_b, u_p denote the cross-sectional mean velocity corresponding to base and peak flow-rates, and t_r is the rising duration of the hydrograph.

The unsteady flow parameter P_{gt} introduced by Bombar et al (2011) is expressed as follows:

$$P_{gt} = \left| S_0 - \left[\frac{u_p - u_b}{g\, t_r} \right] \right| \tag{5}$$

at which S_0 is the channel bottom slope.

In this study, a set of triangular shaped hydrographs having rising and falling durations of 120 seconds to 300 seconds, from the steady state value of 8.6 l/s to the peak value of 50 l/s and 92 l/s were generated in order to investigate the effects of the flow unsteadiness on the transport of bimodal bed materials.

2. EXPERIMENTAL SET-UP, INSTRUMENTATION AND THE SEDIMENT CHARACTERISTICS

2.1. Experimental Set-Up

Experimental studies were carried out on an experimental system involving a rectangular flume 80 cm wide and 18.6 m long. The bottom slope of the flume was 0.006 and it its transparent sides made from plexiglas were 75 cm high. The bed was fixed with small concrete blocks at the first 3 m of the flume giving a total mobile bed length of 15.6 m. The sediment layer thickness was 7 cm along the flume. The sketch of the experimental set-up is given in Figure 1.

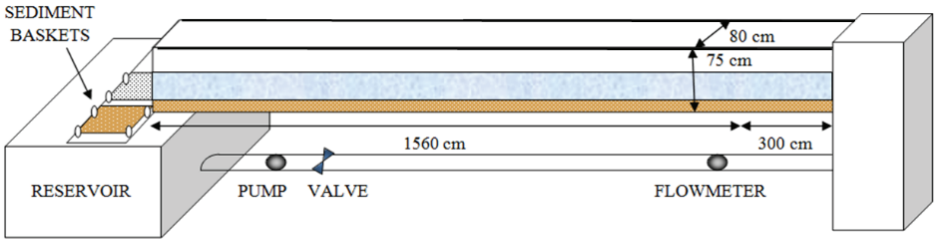

Figure 1 - Scheme of the experimental set-up.

The pump with 100 l/s flow rate capacity was connected to the speed control unit allowing the generation of various shaped hydrographs.

The bed was composed of coarse sand and fine gravel. Before the experiments, the bed was mixed to achieve homogeneity through the vertical and stream-wise directions. The flow rate at the beginning was slowly increased to the base discharge value in order not to disturb the sediments. The experiments were conducted without sediment feeding. The transported bed load was collected in the sediment baskets located at the downstream part of the flume. The grain size distribution was obtained by means of the sieve analysis performed after the collected sediment became dry.

2.2. Instrumentation

The OPTIFLUX 1000 electromagnetic flow meter (manufactured by Krohne) was mounted on the pipe before the entrance of the channel in order to measure the flow rates as Q_{FM}. The ULS– 40D, ultrasonic laboratory water level measuring system was used to measure the water levels in the flume. The IMP+ level monitoring system (Pulsar Process Measurement Limited) was also used to register water depths. The flow depth time series was obtained at x=5 m, 8 m, 11 m, 13.4 m, 15 m and 17 m The velocities were measured by using Ultrasonic Velocity Profiler (UVP) (manufactured by Met-Flow SA) which was located at the entrance of the flume as given in Figure 2. The UVP transducer was placed at the entrance of the flume, looking upwards with an angle of 16 degrees. This configuration helped to determine the flow depths specific to the location that the velocities were measured. The electrolysis was used for the generation of the hydrogen bubbles as seeding particles for the velocity measurements.

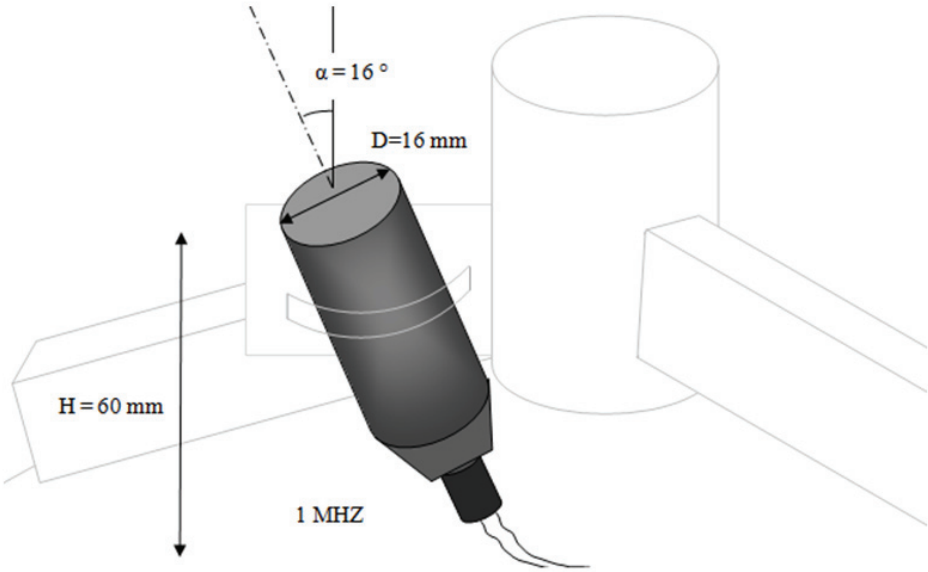

Figure 2 - Ultrasonic Velocity Profile (UVP) transducer configuration

2.3. Bed Material Characteristics

The bed material used in the flume was composed of bimodal sediment mixture. The grain size distribution of the mixture is given in Figure 3. The characteristics of the sediment mixture are given in Table 1. The sediment sizes are calculated by the method and excel sheets given in Gary Parker's Morphodynamics Web Page (2006a,b). The greater sizes such as D_{95} were chosen in accordance with the maximum sediment sizes given in Melville and Sutherland (1988).

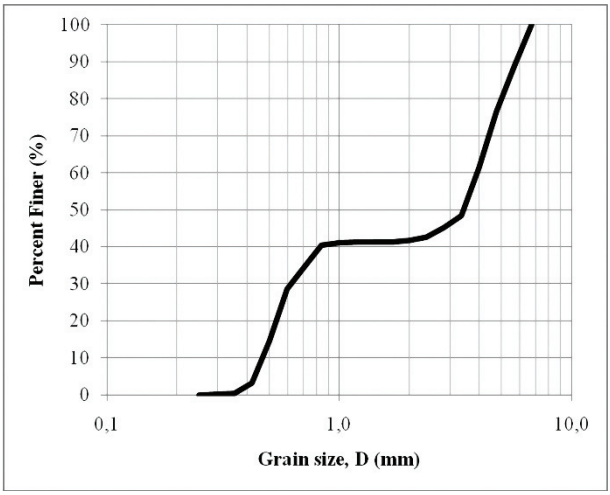

Figure 3 - Grain size distribution of the bed material

Table 1 - Characteristics of the sediment mixture

Parameter	Mixture
Geometric mean size D_g (mm)	1.84
Geometric standard deviation σ_g	2.84
D_5 (mm)	0.45
D_{10} (mm)	0.46
D_{16} (mm)	0.50
D_{30} (mm)	0.61
D_{35} (mm)	0.71
D_{50} (mm)	3.43
D_{60} (mm)	3.88
D_{70} (mm)	4.38
D_{84} (mm)	5.26
D_{86} (mm)	5.41
D_{90} (mm)	5.71
D_{95} (mm)	6.12
D_{96} (mm)	6.20

The sediment less than or greater than 2 mm in size is considered as sand or gravel, respectively. The bimodality index, B* for the particle size distribution in ϕ units

($\phi = -\log_2 D$ where D is particle diameter in mm) was calculated from the following equation proposed by Smith (1997).

$$B^* = \left|\phi_c - \phi_f\right| \left(\frac{P_c}{P_f}\right) \tag{6}$$

where ϕ_f and ϕ_c are the ϕ-sizes of the fine and coarse mode, respectively and P_f and P_c are the proportions of sediment contained in these two modes. The related values are ϕ_f = - 1, ϕ_c = 2, P_f =14.2 and P_c =15.4 which give the value of 3.2 for B*. According to Smith et al (1997), bimodality holds when B* > 1.5, implying that the studied sediment is highly bimodal.

Another definition of bimodality index, denoted by B, is given by Wilcock (1993).

$$B = \left(\frac{D_c}{D_f}\right)^{1/2} \Sigma P_m \tag{7}$$

where D_f and D_c are the grain sizes of the fine and coarse mode, respectively and ΣP_m is the sum of the proportion in mode. The value of B was found to be equal to 2.8 meaning that the sediment is bimodal since the limit value is 1.7.

The incipient motion and bed load calculations were performed by using the median grain size according to the method proposed by Wilcock, (1988) (Güney et al., 2013).

3. ANALYSIS OF RESULTS

3.1. Experimental Results

Experiments were conducted using 5 different triangle shaped input hydrographs. The characteristics of the hydrographs, predefined by a computer software and generated by using the control unit connected to the pump, are given in Table 2 where Q_b, Q_p represent the base and peak flow rates, respectively, calculated by the velocity and flow depth measured by UVP at the entrance. In the table, h_b, h_p represent the base and peak flow depths and u_b, u_p represent the base and peak velocities determined by UVP. The discharge values were measured by means of the flowmeter placed on the the pipe supplying water to the channel. The hydrograph generated at the discharge pipe of the pump was attenuated during its propagation through the flume and lower values of base and peak flow depths were registered in the channel. $h_{b\ x=13.4\ m}$ and $h_{p\ x=13.4\ m}$ denote the base and peak flow depths measured in the channel at x = 13.4 m downstream of the entrance of the flume. The t_r, t_f and t_d, are the rising, falling and total durations of the hydrograph respectively. Fr_{base} and Fr_{peak} refer to the Froude numbers calculated for base and peak flow rates, respectively. The Froude numbers given above were calculated by using these flow depths and corresponding velocity

values obtained by UVP. Froude numbers being smaller than unity indicates the subcritical character of the experimental conditions.

Table 2 - Characteristics of the hydrographs and flow parameters used in this study

Experiment	Exp-1	Exp-2	Exp-3	Exp-4	Exp-5
Q_b (l/s)	8.6	8.6	8.6	8.6	8.6
Q_p (l/s)	66.0	72.4	45.6	69.2	92.4
h_b (m)	0.049	0.049	0.049	0.049	0.049
h_p (m)	0.131	0.133	0.114	0.133	0.156
u_b (m/s)	0.22	0.22	0.22	0.22	0.22
u_p (m/s)	0.63	0.68	0.50	0.65	0.74
$Q_{pipe\,p}$ (l/s)	71.0	71.1	49.3	69.7	91.7
$h_{b\ x=13.4m}$ (mm)	37	37	37	37	37
$h_{p\ x=13.4m}$ (mm)	13	11	9.2	11	4-
t_r (min)	2	3	5	5	5
t_f (min)	2	3	5	5	5
t_d (min)	4	6	10	10	10
Fr_{base}	0.32	0.32	0.32	0.32	0.32
Fr_{peak}	0.56	0.60	0.47	0.57	0.60

Triangle-shaped input hydrographs were generated for a total of seven runs to ensure repeatability and reliability of the results. The mean value of each parameter i.e, g_b, D_5, σ_g etc., was calculated to obtain representative results and are presented in the subsequent figures and tables. For instance, equation (8a) was used to obtain the mean value of g_b out of n runs. To investigate the effect of unsteady flow on the size distribution of the sediment mixture, two selected runs were analyzed by performing a sieve analysis for each collected bed load sample. The scattering index for a given time, SI_t, is calculated by dividing root-mean-square error (RMSE) with mean of the runs for that time interval as in the equation (8b). The mean of SI_t values for the runs with sieve analysis and mean of SI_t values for all experiments were determined as given in equation (8c), where m is the number of bed load samples for a specific experiment and presented in Table 3. For illustrative purposes, the relation between the mean of the bed load obtained by considering all repeated runs and those runs conducted for sieve analysis are depicted in Figure 4 for Exp-1 and Exp-3. Complete set of R^2 values are given in Table 3 as well as the SI values for the parameters D_5, D_{50}, D_{95} and σ_g parameters.

$$\overline{g_b} = \frac{1}{n}\sum_{i=1}^{n} g_{bi} \tag{8a}$$

$$SI_t = \frac{\sqrt{\frac{1}{n}\sum_{i=1}^{n}(g_{bi}-\overline{g_b})^2}}{\overline{g_b}} \tag{8b}$$

$$SI = \frac{1}{m}\sum_{t=1}^{m} SI_t \tag{8c}$$

Table 3 - Statistical analysis of the hydrographs and flow parameters used in this study

	Exp-1	**Exp-2**	**Exp-3**	**Exp-4**	**Exp-5**
SI of g_b all runs	0.42	0.34	0.36	0.46	0.27
SI of g_b with sieve analysis	0.33	0.14	0.26	0.31	0.30
R^2	0.9914	0.9925	0.9930	0.9804	0.9989
SI of D_5	0.02	0.03	0.03	0.03	0.03
SI of D_{50}	0.21	0.08	0.17	0.17	0.17
SI of D_{95}	0.08	0.02	0.09	0.20	0.19
SI of σ_g	0.06	0.02	0.04	0.05	0.06

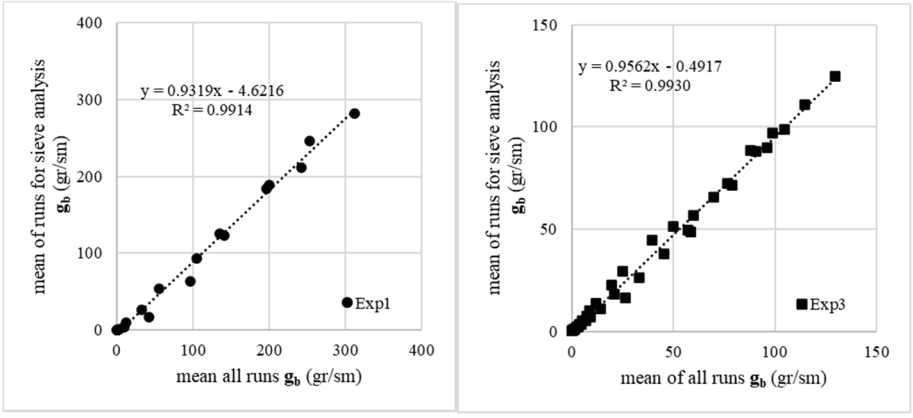

Figure 4 - Relation between the mean of the bed load obtained by considering all repeated runs and those runs conducted for sieve analysis a) Exp-1, b) Exp-3.

The variation of flow rate with respect to time is given in Figure 5. The flow depth variation is given in Figure 6. The cross-sectional mean velocity measured by UVP at the entrance of the flume is given in Figure 7.

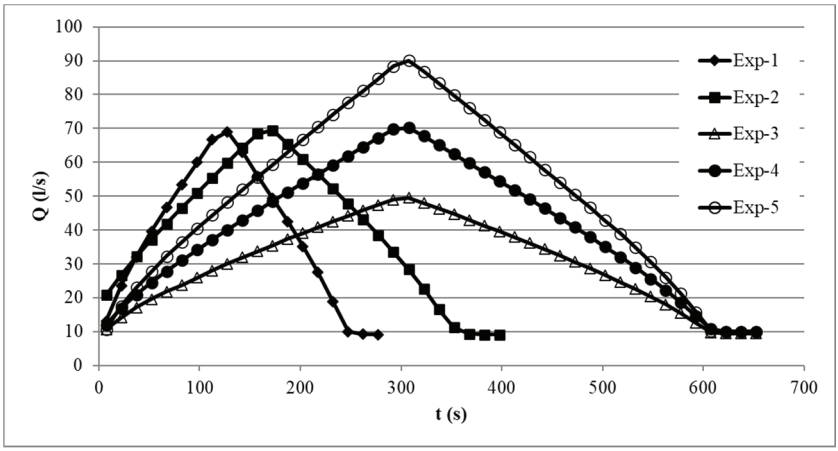

Figure 5 - Flow rate variations with respect to time

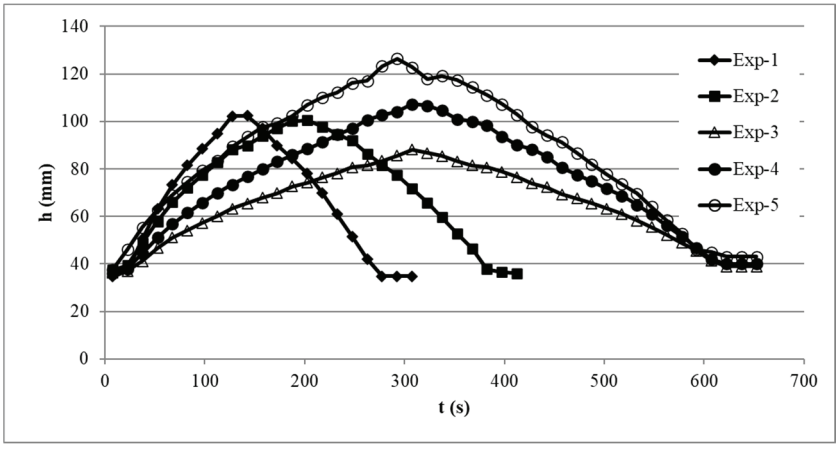

Figure 6 - Flow depth variations with respect to time

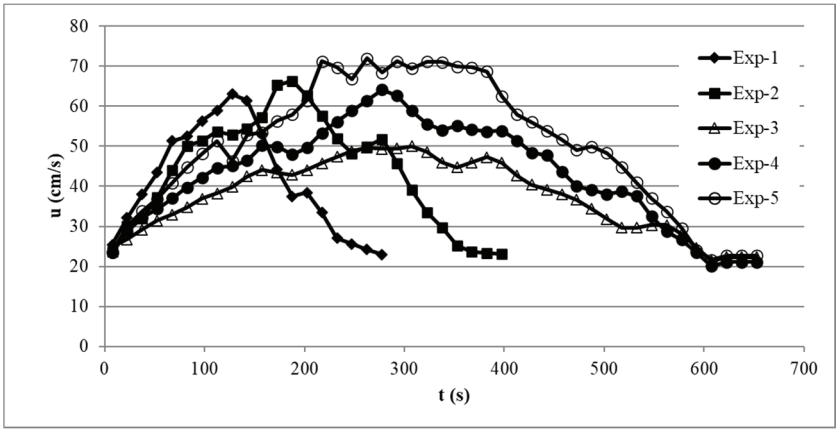

Figure 7 - Cross sectional mean velocity variations with respect to time

The average values of the time variation of the bed load are given in Figure 8. Some bed forms of small magnitude were observed during the experiments.

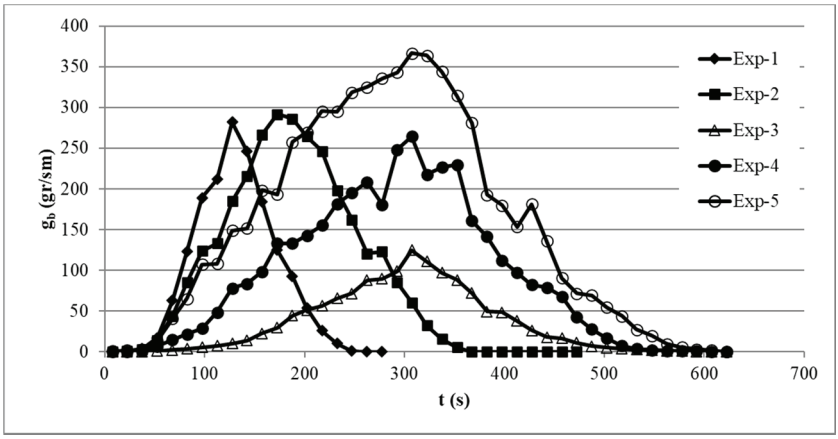

Figure 8 - Bed load variations with respect to time

The shear velocity is calculated by the Equation (9)

$$u_* = \sqrt{g\ R\left(S_0 - \frac{\partial h}{\partial x}\right)} \tag{9}$$

where R is the hydraulic radius, and x is the abscissa.

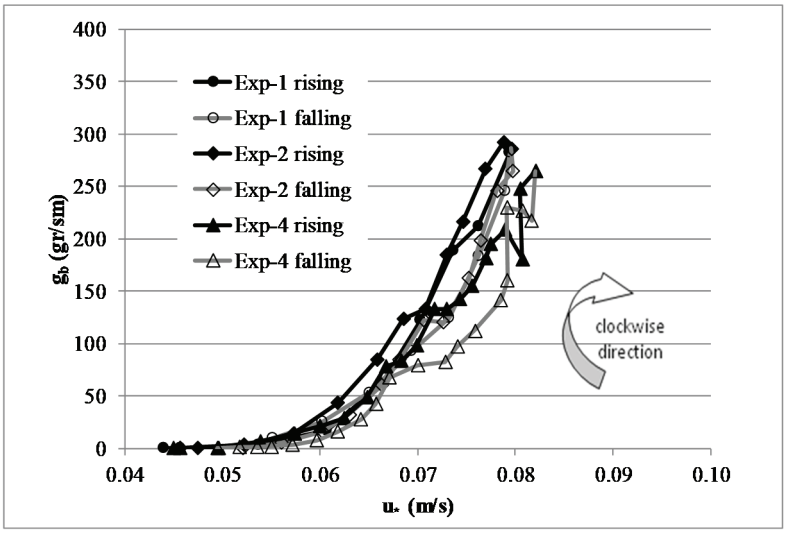

(a)

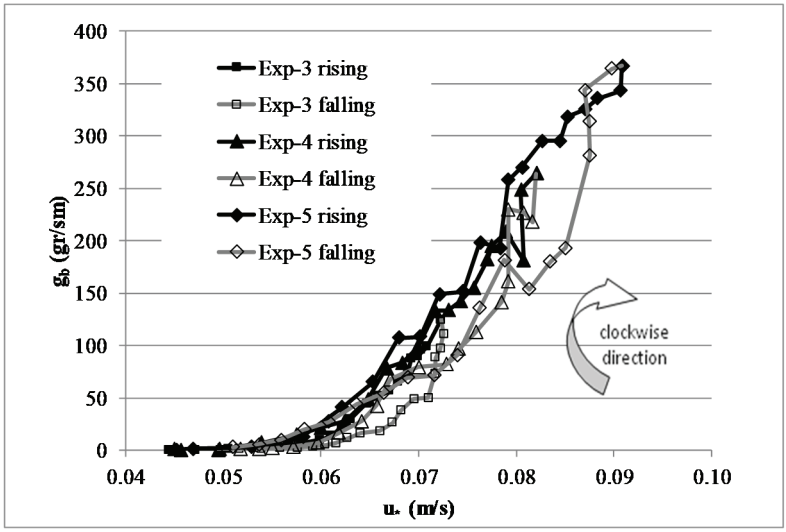

Figure 9 - Variations of the bed load with respect to the shear velocity for (a) Exp-1, Exp-2 and Exp-4, (b) Exp-3, Exp-4 and Exp-5

The variation of the bed load with respect to the shear velocity is given in Figure 9.a and Figure 9.b. There was a clockwise behavior meaning that the bed load was higher during the rising compared to the falling. This clockwise behavior was also observed by Kuhnle (1992) and Nanson (1974).

3.2. The Grain Size Distribution of Transported Sediment

The sieve analysis was performed for each group of sediments collected in the baskets in order to obtain the variation of the grain size distribution with respect to time. The average values corresponding to the intervals of 1 minute were determined and they are depicted in Figure 10.a to 10.e for the Exp-1 to Exp-5, respectively.

Based on the experimental results, it was observed that the percent finer concerning the plateau had higher value during the initial and final phases compared to those obtained during the peak time. The plateau percentages corresponding to the peak value of the time were close to each other for all hydrographs and they were nearly equal to the initial percentages of the bed material. It was observed that the percent finer value for the highest duration hydrographs (10 minutes) in Exp-3, Exp-4 and Exp-5 were approximately in the same order. The smallest value was found in the case of Exp-1 corresponding to the shortest hydrograph. It was concluded that the location of the plateau was highly influenced by the hydrograph duration.

The time variation of the sand content ratio of the bed load is given in Figure 11. At the beginning of the experiments, the sand content of the transported bed material decreased rapidly from approximately 96 % to 30% – 40% which was the original sand content of the bed material. The sand content remained constant for a while (t_w) and gradually increased at the end of the hydrograph. The values of t_w and t_w / t_r are given in Table 4.

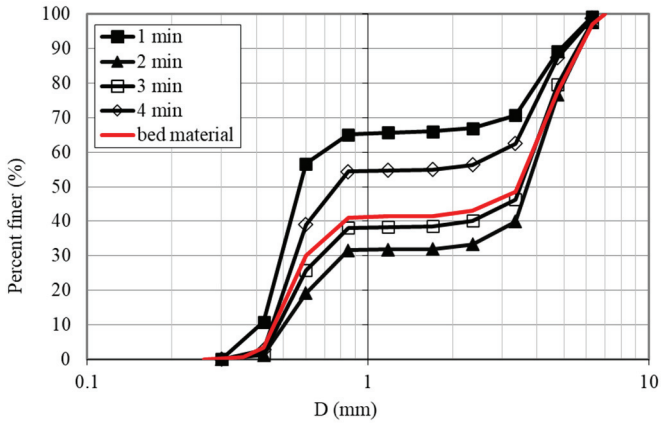
1 min
2 min
3 min
4 min
bed material
Percent finer (%)
D (mm)
0.1
1
10

(a)

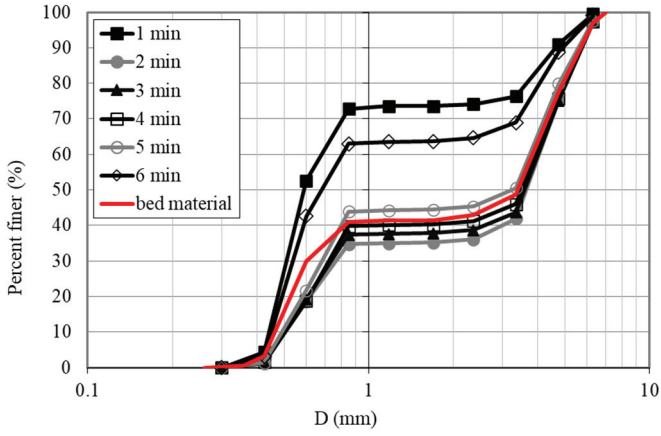
1 min
2 min
3 min
4 min
5 min
6 min
bed material
Percent finer (%)
D (mm)
0.1
1
10

(b)

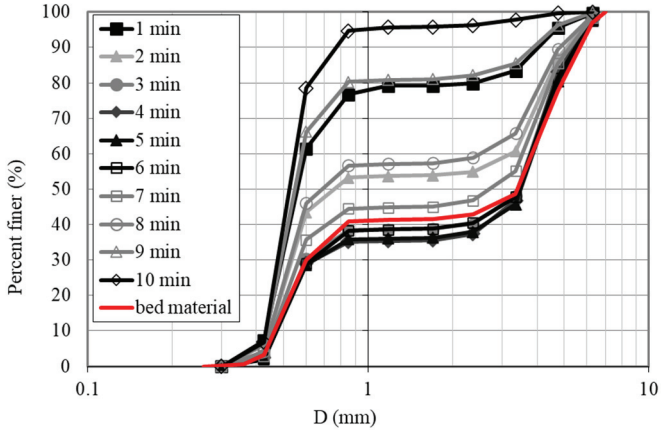
1 min
2 min
3 min
4 min
5 min
6 min
7 min
8 min
9 min
10 min
bed material
Percent finer (%)
D (mm)
0.1
1
10

(c)

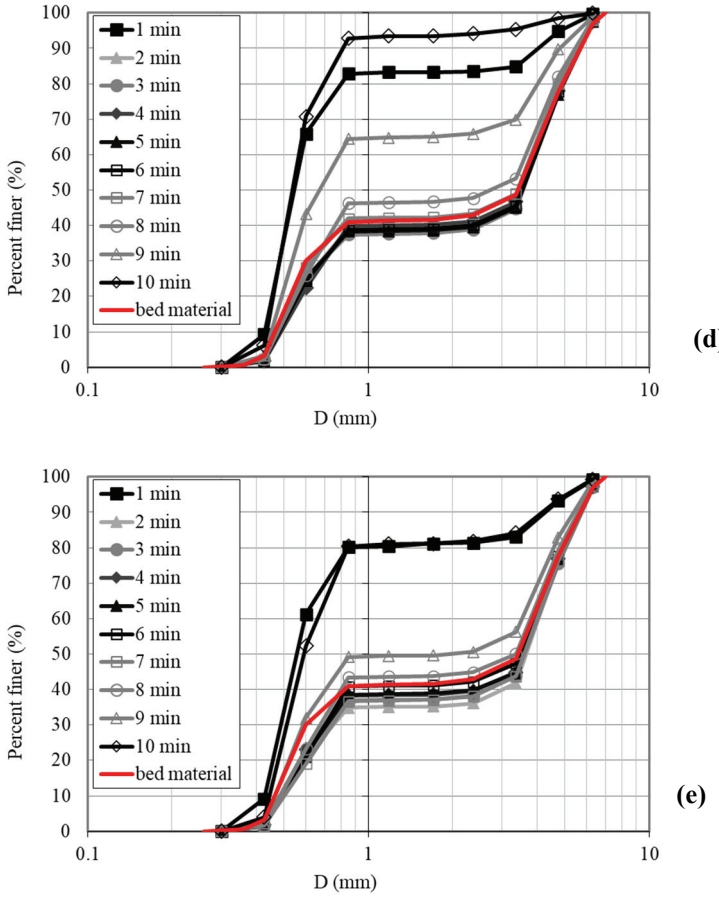

Figure 10 - Grain size distribution variations with respect to time, (a) Exp-1, (b) Exp-2, (c) Exp-3, (d) Exp-4, (e) Exp-5

During the peak phases, the flow velocity has greater values. When the velocity was low, the flow had not the ability to transport the coarser sediment sizes, and consequently only sand material displaced. On the other hand, when the velocity increased the coarser grains were also included comprising the percentage of the bed load almost of the same percentage existing in the bed material.

The bimodality index B* was calculated and its variation with time is depicted in Figure 12. It was observed that in all experiments the B* increased quickly in the rising limb and then had a nearly constant value slightly greater than unity for bed material. In the falling phase the value of the B* decreased to its original and initial value. The percent contents of sand and gravel for Exp-4 at various times along with percent content of the bed material are given in Figure 13.

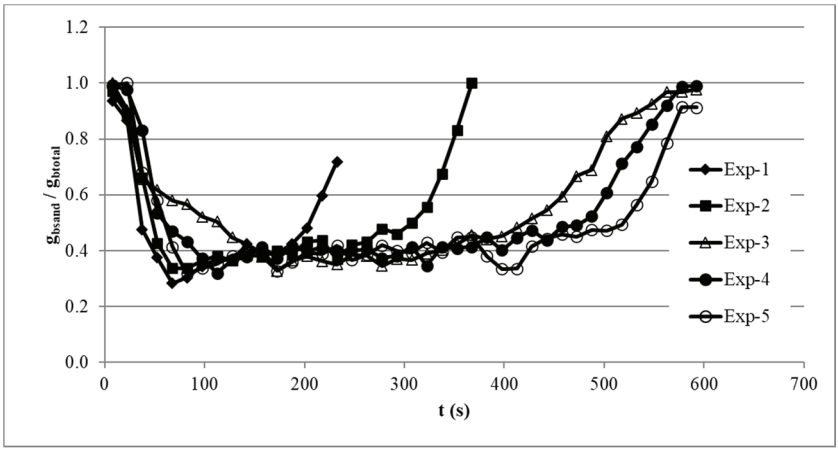

Figure 11 - Time variations of the sand content ratio of the bed load

Table 4 - t_w and t_w / t_r values

Experiment	Exp-1	Exp-2	Exp-3	Exp-4	Exp-5
t_w (s)	100	250	360	410	420
t_w / t_r	0.83	1.33	1.20	1.37	1.40

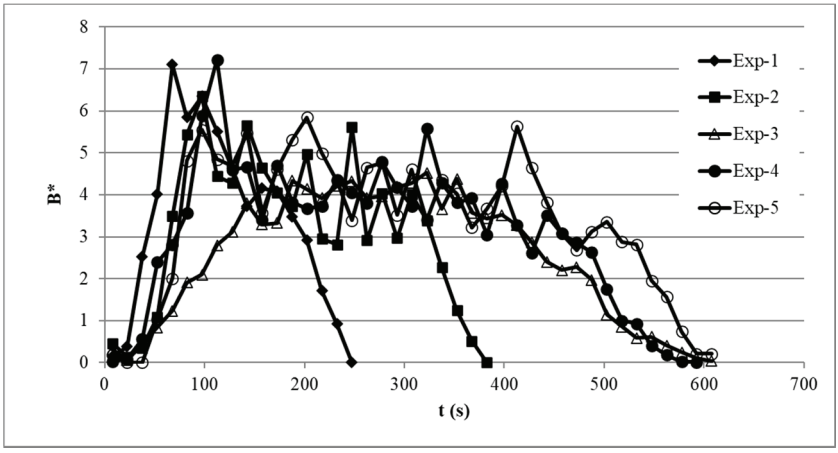

Figure 12 - Variation of Bimodality index B with time*

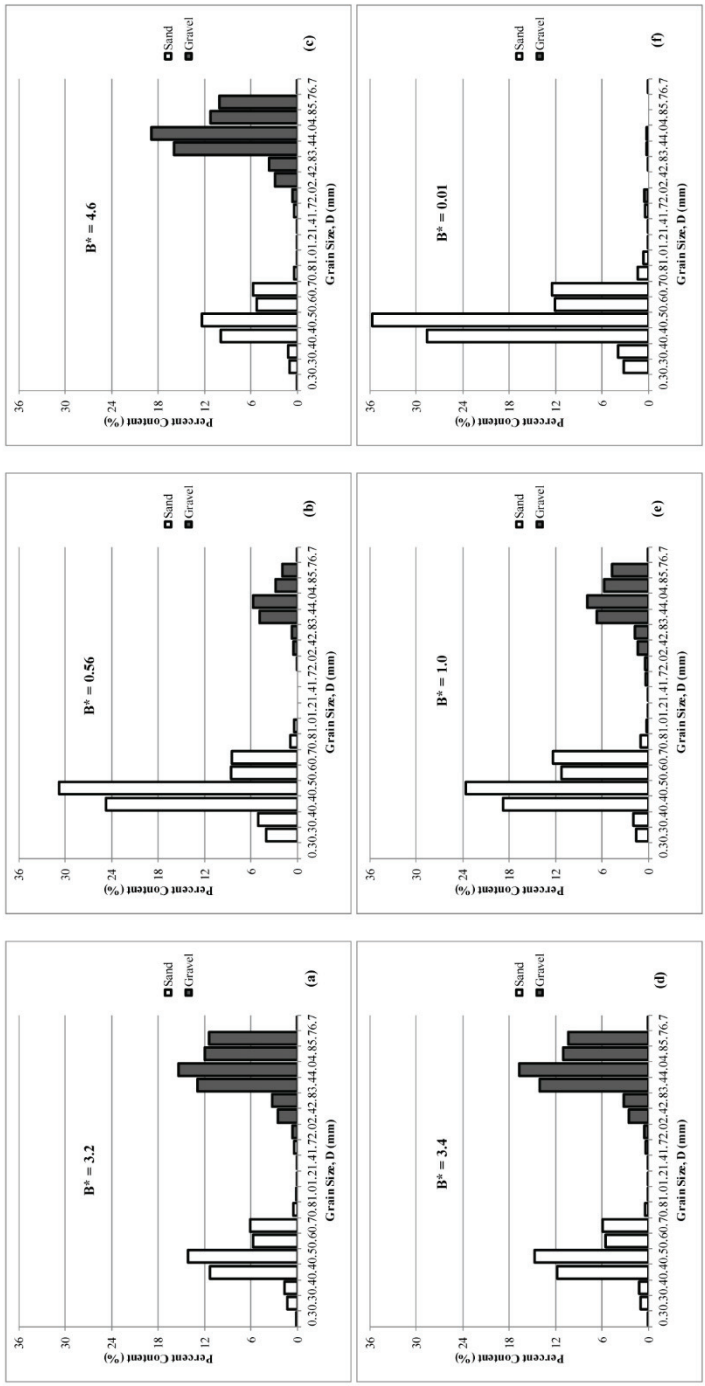

Figure 13 - The percent content of sand and gravel for Exp-4 (a) bed material (b) at t=40 s, (c) at t=130 s, (d) at t=160 s, (e) at t=520 s, (f) at t=580 s

The variations of the percent sand content of the bed load with respect to the shear velocity are given in Figure 14.a and Figure 14.b. It was revealed that the sand percent of the bed load decreased in the falling limb, showing a counterclockwise loop. The duration of the hydrograph was not likely to affect the results considerably. On the other hand, the greater the peak flow rate of the hydrograph, the greater the hysteresis.

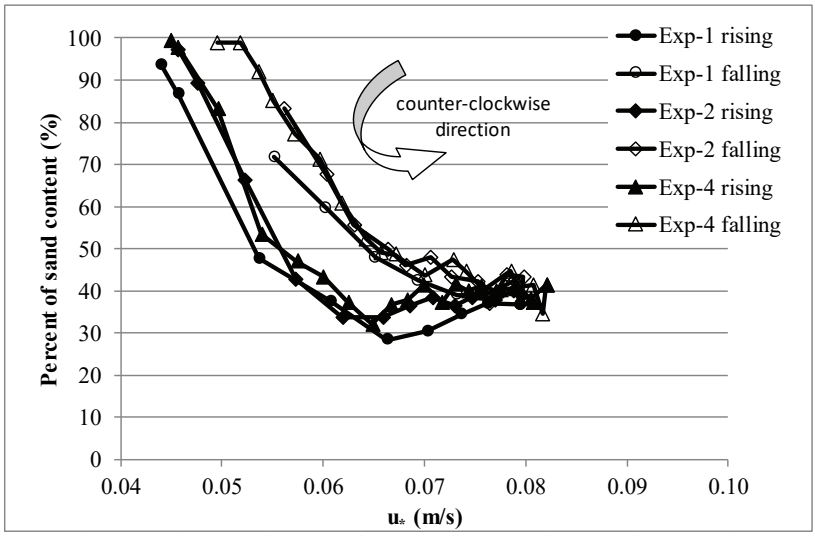

Figure 14 - Variations of the percent sand content of the bed load with respect to the shear velocity for (a) Exp-1, Exp-2 and Exp-4, (b) Exp-3, Exp-4 and Exp-5

The values of D_5, D_{50} and D_{95} were determined from the cumulative grain size distribution curves of the collected sediments. The variations of D_5 with respect to the shear velocity are given in Figure 15.a and Figure 15.b. The 5% finer sediment amounts were the same for the whole duration of the hydrographs for all experiments.

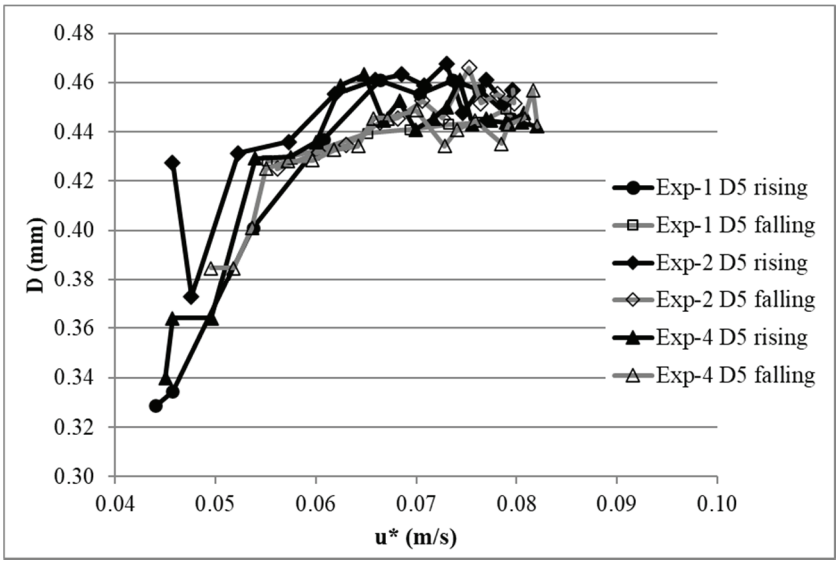

(a)

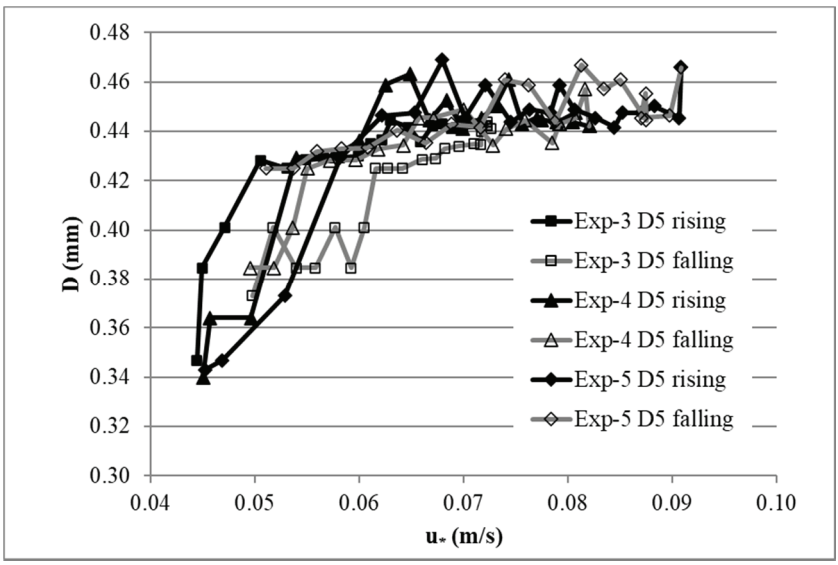

(b)

Figure 15 - Variations of D_5 with respect to the shear velocity, for (a) Exp-1, Exp-2 and Exp-4, (b) Exp-3, Exp-4 and Exp-5

The variations of D_{50} with respect to the shear velocity are given in Figure 16.a and Figure 16.b. It was revealed that D_{50} value of the bed load decreased in the rising limb, showing a clockwise loop. The hysteresis was not considerably changed with respect to hydrograph characteristics.

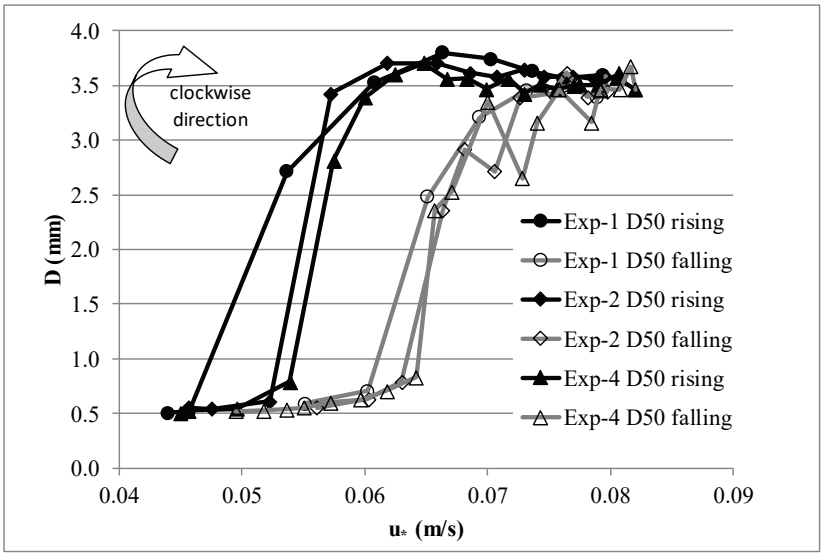

Figure 16 - Variations of D_{50} with respect to the shear velocity, for (a) Exp-3, Exp-4 and Exp-5, (b) Exp-1, Exp-2 and Exp-4

The variations of D_{95} with respect to the shear velocity are given in Figure 17.a and Figure 17.b. The clockwise type of hysteresis was also observed for this size group. The D_{95} in Exp-3, Exp-4 and Exp-5 had an influence on the hysteresis where the lag increased with the increase in the peak flow rate.

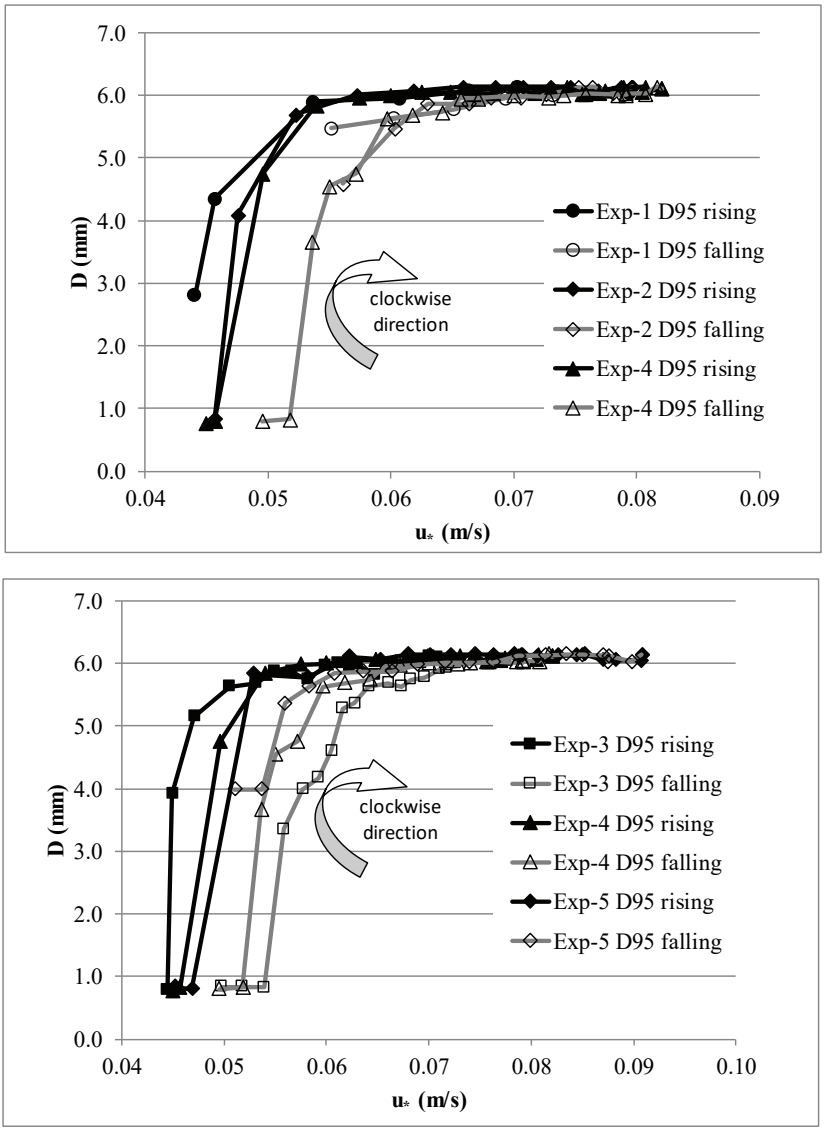

Figure 17 - Variations of D_{95} with respect to the shear velocity, for (a) Exp-3, Exp-4 and Exp-5, (b) Exp-1, Exp-2 and Exp-4

3.3. Total Flow Work Index and Unsteadiness Parameters

The experimental results of the hydrographs and the amount of the bed load collected during the rising and falling limbs of the hydrographs are summarized in Table 5. The total volume was calculated by assuming a basic triangular shape and dimensionless parameters were calculated by using the flow data obtained at the entrance of the flume since both velocity and flow depth values could be measured only at that section.

Table 5 - Experimental results and unsteadiness parameters

Experiment	Exp-1	Exp-2	Exp-3	Exp-4	Exp-5
Total volume excluding base flow (m^3)	6.9	11.5	11.1	18.2	25.1
W_k	19.2	31.9	30.9	50.5	69.9
W_t (kg)	22.1	37.1	17.6	45.3	77.6
W_t*	904	1518	721	1853	3371
P	0.0067	0.0046	0.0021	0.0028	0.0035
P_{mod}	0.0026	0.0017	0.0008	0.0011	0.0015
P_{gt}	0.00565	0.00574	0.00590	0.00585	0.00582
u_p* (m/s)	0.08	0.08	0.07	0.08	0.08

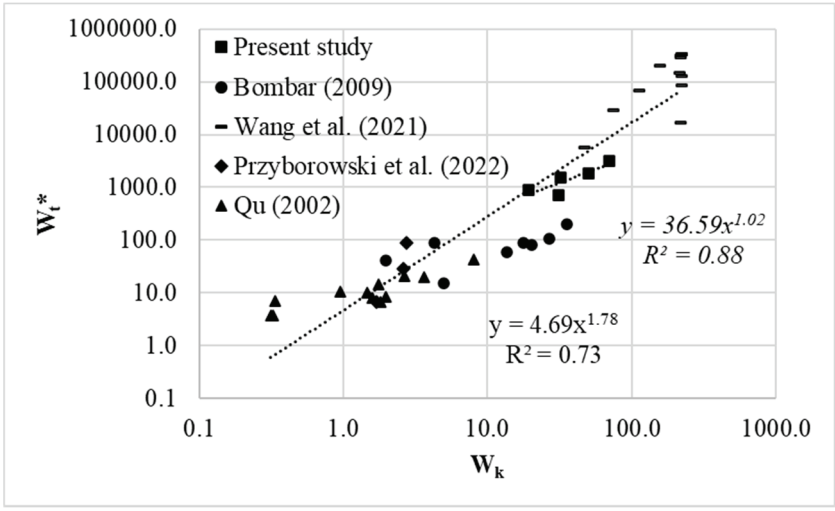

(a)

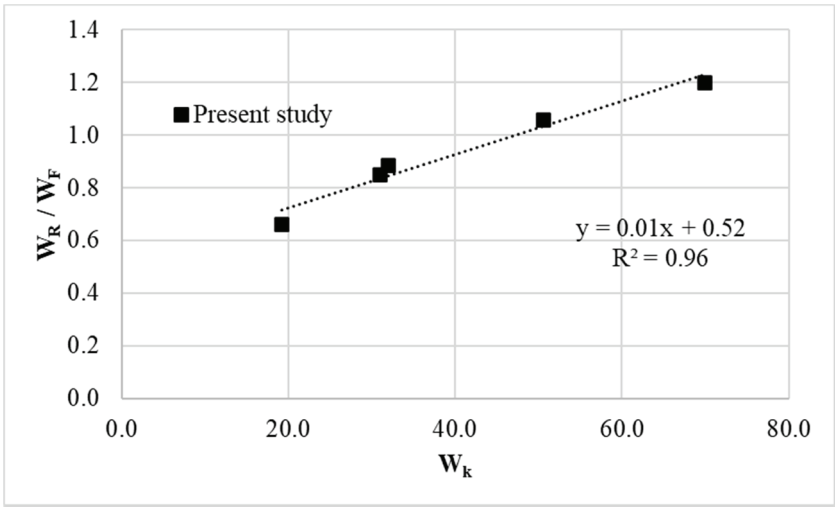

Figure 18 - (a) Variation of W_t with respect to the total work index W_k, (b) Variation of W_R/W_F with respect to the total work index W_k*

The variation of the dimensionless total bed load W_t* with respect to the total work index W_k is presented in Figure 18.a. The data of Bombar (2009), Qu (2002), Wang et al. (2021) and Przyborowski et al. (2022) were also added to the graph. A strong relation (Eq. 10.a) was found between W_t* and W_k with a determination coefficient of R^2= 0.88, when only the data of present study was regarded. When the data mentioned above was also considered the R^2 became 0.73, the SI is calculated as 1.68. and the relation given in equation (10.b) was obtained.

$$W_t^* = 36.59\ W_k^{1.02} \quad (10.a)$$

$$W_t^* = 4.69\ W_k^{1.78} \quad (10.b)$$

By using the equation given above the amount of bed load for a given duration of a hydrograph can be predicted provided that the volume of water that corresponds to the area under the hydrograph is known.

The variation of the dimensionless total bed load W_R/W_F with respect to the total work index W_k is presented in Figure 18.b. The following relation with a determination coefficient of 0.96 and SI as 0.04 were obtained:

$$W_R/W_F = 0.01W_k + 0.52 \quad (11)$$

The values of the unsteadiness parameters P, P_{mod} and P_{gt} calculated from the relevant equalities stated previously are given in Table 4.

The variation of the dimensionless total bed load W_t* versus the unsteadiness parameters P, and P_{mod} were plotted in Figure 19.a and 19.b, respectively together with the data of Bombar

(2009), Qu (2002), Wang et al. (2021) and Przyborowski et al. (2022). The coefficients of determination were very low, particularly for P_{mod}, which imply that their interrelation was not significant.

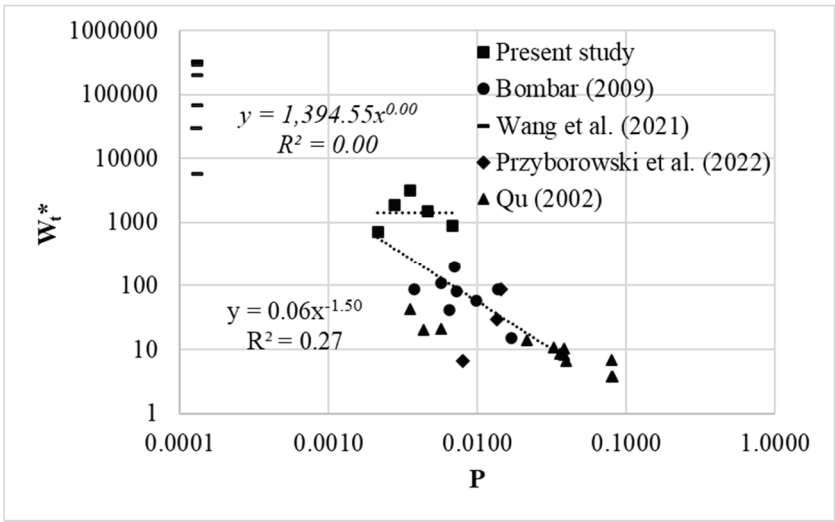

Figure 19 - Variation of dimensionless total bed load Wt with the unsteadiness parameter (a) P, (b) P_{mod}*

The variation of the dimensionless total bed load versus the unsteadiness parameter P_{gt} is plotted in Figure 20, together with the data of Bombar (2009), those of Qu (2002), Wang et al. (2021) and Przyborowski et al. (2022). Four experiments of Qu (2002) and the experiments of Wang et al. (2021) seem to deviate from the given exponential relation. The reason is proposed to be the difference between the range of time durations such that the tr

of Qu (2002) for those is 10 seconds and all experiments of Wang et al. (2021) is longer than 60 mins which is 12 times greater than those experiments focused in this study. Note that when the duration is sufficiently long the unsteadiness parameter P_{gt} has almost no affect on the W_t*. Excluding these set of experiments, the high value of the determination coefficient of 0.69 stands for an appreciable interdependence. The SI values are 1.58, 2.24 and 2.17 for P_{gt}, P and P_{mod}, respectively.

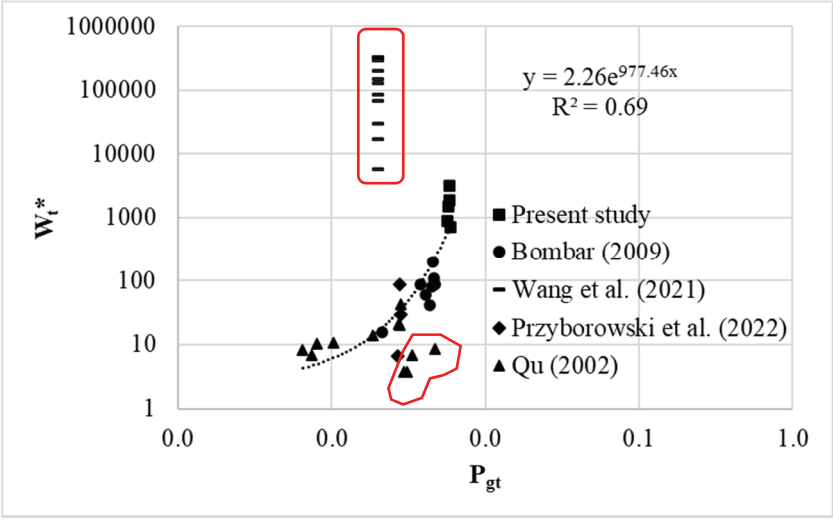

Figure 20 - Variation of unsteadiness parameter W_t with dimensionless total bed load P_{gt}*

4. CONCLUSION

The aim of this experimental study is to investigate the unsteadiness effects on the transport of bimodal bed material. A clockwise behavior was observed in the total bed load - shear velocity curve which means that the bed load was higher on the rising limb compared to that of the falling limb.

From the variation of the grain size distribution with respect to time, it was found that the percent finer at the plateau of bimodal sediment size distribution curve had higher values during the initial and final phases compared to those obtained during the peak time. At all plateaus, the percent finer values related to the hydrograph peak discharge were in the same order of magnitude with that of the bed material.

It was observed that in all experiments the bimodality index B* increased quickly in the rising limb and then had a nearly constant value slightly greater than that of the bed material, eventually reaching its initial value.

The sand content of the transported bed material decreased rapidly ≅ from ≅ 96 % to ≅ 30% – 40% which was the original sand content of the bed material. The sand content remained constant for a while and gradually increased at the end of the hydrograph.

The variation of the percent sand content of the bed load with respect to the shear velocity revealed that the sand percent of the bed load decreased in the falling limb showing a counterclockwise loop and the duration of the hydrograph did not affect the results considerably, within the limits of the experimental campaign. On the other hand, the greater peak flow rate of the hydrograph resulted in greater hysteresis.

The values of D_5, D_{50} and D_{95} were determined from the cumulative grain size distribution curves of the collected sediments. The 5% finer sediment amount was nearly equal during rising and falling limbs. It was observed that D_{50} value of the bed load decreased in the rising limb showing a clockwise loop. The hysteresis was not considerably changed according to the hydrograph characteristics. The clockwise type hysteresis was also observed for the size group of D_{95}. The lag increased as the peak flow rate increased.

A strong relation was found between the dimensionless total bed load W_t* and the total work index W_k with a determination coefficient R^2= 0.81. The determination coefficient R^2 between W_R/W_F and W_k was found as 0.73.

The correlations between the dimensionless total bed load and the unsteadiness parameters P, and particularly for P_{mod} were very weak which imply that their interrelation was not significant. As to the unsteadiness parameter P_{gt}, the high value of determination coefficient of 0.69 stands for an appreciable interdependence. Considering the complexity of the unsteadiness parameter P_{mod}, it is revealed that within the limitations of this study which are given in Table 6, Pgt together with Wk could be used to calculate the Wt* for unsteady flows.

Table 6 - Limitations of the present study

Parameter	Minimum value	Maximum value
D_{50} (mm)	3.4	5.8
h_b (m)	0.02	0.12
h_p (m)	0.09	0.22
Q_b (l/s)	12.0	30.3
Q_p (l/s)	63.7	86.3
t_f (min)	0.2	5.0
t_r (min)	0.5	5.0
S_o (m/m)	0.002	0.006
P_{gt}	0.0038	0.0047
W_k	2.0	35.6
W_t*	41	197

Acknowledgement

The authors would like to express their sincere appreciation to TUBITAK which provided financial supports of this study through the Projects No: 106M274 and 109M637.

References

[1] Bombar, G., 2009, Experimental and numerical investigation of bed load transport in unsteady flows, October 2009, PhD Thesis, Dokuz Eylül University Graduate School of Natural And Applied Sciences.

[2] Bombar, G., Elçi, Ş., Tayfur, G., Güney, M.Ş., Bor, A., 2011, Experimental and numerical investigation of bedload transport under unsteady flows, Journal of Hydraulic Engineering. posted ahead of print February 25, 2011. doi:10.1061/(ASCE)HY.1943-7900.0000412

[3] De Sutter, R., Verhoeven, R., Krein, A., 2001, Simulation of sediment transport during flood events: laboratory work and field experiments. Hydrological Sciences-Journal-des Sciences Hydrologiques, 46(4), 599-610.

[4] Duan, Z., Chen, J., Jiang, C., Liu, X., and Zhao, B., 2020, Experimental Study on Uniform and Mixed Bed-Load Sediment Transport under Unsteady Flow Appl. Sci. 2020, 10, 2002; doi:10.3390/app10062002

[5] Gumgum, F., Guney, M.S., 2021, Effect of Sediment Feeding on Live-Bed Scour around Circular Bridge Piers, Civil Engineering Journal, Vol. 7, No. 05, pp 906-914, DOI:10.28991/cej-2021-03091699

[6] Güney, M.Ş., Bombar G.,Aksoy A.Ö., 2013, Experimental study of the coarse surface development effect on the bimodal bed load transport under unsteady flow conditions, Journal of Hydraulic Engineering, Vol. 13, No. 1, pp 12-21. DOI: 10.1061/(ASCE)HY.1943-7900.0000640.

[7] Gunsolus, E.H., Andrew, B.D., 2017, Effect of morphologic and hydraulic factors on hysteresis of sediment transport rates in alluvial streams River Res Applic. 2018;34:183–192. DOI: 10.1002/rra.3184

[8] Gunsolus, E.H., Binns, A.D. 2017, Effect of morphologic and hydraulic factors on hysteresis of sediment transport rates in alluvial streams, River Research and Applications, Vol. 34, No. 2, pp 183-192 . DOI:10.1002/rra.3184

[9] Houssais, M., Lajeunesse E., 2012, Bedload transport of a bimodal sediment bed, Journal of Geophysıcal Research, Vol. 117, F04015, DOI:10.1029/2012JF002490,

[10] Khosravi, K., Chegini, A.H.N., Binns, A.D., Daggupati, P. and Mao, L., 2019, Difference in the bed load transport of graded and uniform sediments during floods: An experimental investigation Hydrology Research | 50.6

[11] Kuhnle, R.A., 1992, Bed load transport during rising and falling stages on two small streams, Earth Surface Processes and Landforms, Vol 17, 191-197

[12] Lee, K.T., Liu, Y.L., Cheng, K.H. 2004, Experimental investigation of bedload transport processes under unsteady flow conditions, Hydrological processes, 18(13), pp. 2439-2454.

[13] Li, Z., Qian, H., Cao, Z., Liu, H., Pender, G., Hu, P., 2018, Enhanced bedload sediment transport by unsteady flows in a degrading channel International Journal of Sediment Research 33 327–339 https://doi.org/10.1016/j.ijsrc.2018.03.002

[14] Mao, L., 2012, The effect of hydrographs on bed load transport and bed sediment spatial arrangement, Journal of Geophysical Research Atmospheres, Vol. 117, F03024, DOI:10.1029/2012JF002428

[15] Mao, L., 2018, The effects of flood history on sediment transport in gravel-bed rivers Geomorphology 322 (2018) 196–205 https://doi.org/10.1016/j.geomorph.2018.08.046.

[16] Melville, B., Sutherland, A. 1988, Design method for local scour at bridge piers, Journal of Hydraulic Engineering, Vol. 114, No. 10, pp 1210–1226.

[17] Mrokowska, M.M. and Rowinski, P.M., 2019, Impact of Unsteady Flow Events on Bedload Transport: A Review of Laboratory Experiments Water 2019, 11, 907; doi:10.3390/w11050907

[18] Müller, E.N., Batalla R.J., Bronstert A., 2008, Modelling bedload transport rates during small floods in a gravel-bed river. Journal of Hydraulic Engineering 134, 1430-1439

[19] Nanson, G.C., 1974, Bedload and suspended load transport in a small, steep, mountain stream, Am. Journal Sci., 274, 471-486.

[20] Przyborowski L., Nones M., Mrokowska M., Książek L., Phan C.N., Strużyński A., Wyrębek M., Mitka B., Wojak S., 2022, Preliminary evidence on laboratory experiments to detect the impact of transient flow on bedload transport, Acta Geophysica, https://doi.org/10.1007/s11600-022-00743-5Parker G, 2008, "Chapter 3, Transport of Gravel and Sedıment Mıxtures", ASCE Manual 54, http://hydrolab.illinois.edu/people/parkerg/_private/Man54/Man54Chap3WholeText.pdf

[21] Parker's Morphodynamics Web Page, (2006a, Calculator for statistical characteristics of grain size distributions: http://hydrolab.illinois.edu/people/parkerg/_private/e-bookExcel/RTe-bookGSDCalculator.xls

[22] Parker's Morphodynamics Web Page, 2006b, Characterization of Sediment and Grain Size Distributions: http://hydrolab.illinois.edu/people/parkerg/_private/e-bookPowerPoint/RTe-bookCh2SedimentGSD.ppt

[23] Perret, E., Berni, C., Camenen, B., Herrero, A., Abderrezzak, K.E. 2018, Transport of moderately sorted gravel at low bed shear stresses: The role of fine sediment infiltration. Earth Surf. Process. Landforms, 43, 1416–1430.

[24] Plumb, B.D., Juez, C., Annable, W.K., McKie1, C.W., and Franca, M.J., 2020, The impact of hydrograph variability and frequency on sediment transport dynamics in a gravel-bed flume Earth Surf. Process. Landforms 45, 816–830 (2020) DOI: 10.1002/esp.4770

[25] Qu, Z., 2002, Unsteady open-channel flow over a mobile bed, PhD Thesis, EPFL, Thesis no 2688

[26] Reid, I., Frostick L.E., Layman J.T., 1985, The incidence and nature of bedload transport during flood flows in coarse-grained alluvial channels, Earth Surface Processes and Landforms, Vol 10, 33-44

[27] Saadi, Y., 2008, Fractional Critical Shear Stress at incipient motion in a bimodal sediment, Civil Engineering Dimension, Vol 10, No 2, pp 89-98

[28] Sambrook Smith G.H., 1996, Bimodal fluvial bed sediments: origin, spatial extent and processes, Progress in Physical Geography, Vol 20, No 4, pp 402-417, DOI: 10.1177/030913339602000402

[29] Smith Nicholas Ferguson, 1997, Measuring and defining bimodal sediments: Problems and implications, Water Resources Research, Vol 33, pp 1179-1185

[30] Tabarestani, M., Zarrati, K. 2015, Sediment transport during flood event: a review Int. J. Environ. Sci. Technol. 12:775–788 DOI 10.1007/s13762-014-0689-6

[31] Tian, S. and Wang Z., 2009, Bimodal sediment distribution and its relation with the river ecology in the Dadu River Basin, Advances in Water Resources and Hydraulic Engineering, pp 1049-1054

[32] Wang, L., Cuthbertson, A., Pender, G., 2013, Experimental investigation on temporal lag effect of graded sediment transport in unsteady flows Proceedings of 2013 IAHR Congress © 2013 Tsinghua University Press, Beijing

[33] Wang, L., Cuthbertson, A., Pender, G., Cao, Z., 2014, The Response of Bed-load Sediment Transport and Bed Evolution under Unsteady Hydrograph Flows, River Flow 2014 Conference: River Flow 2014 – the 7th International Conference on Fluvial Hydraulics At: Lausanne, Switzerland September 2014 DOI: 10.1201/b17133-215

[34] Wang, L., Cuthbertson, A., Pender, G., Cao, Z., 2015, Experimental investigations of graded sediment transport under unsteady flow hydrographs International JournalofSedimentResearch30(2015)306–320 http://dx.doi.org/10.1016/j.ijsrc.2015.03.010

[35] Wang, L., Wang, D., Cuthbertson, A.J.S., Zhong, D., and Pender, G., 2021a, Hysteretic Implications for Graded Bed Load Sediment Transport in Symmetrical Hydrograph Flows. Front. Environ. Sci. 9:800832. doi: 10.3389/fenvs.2021.800832

[36] Wang, L., Cuthbertson, A.J.S., Zhang, S.H., Pender, G., Shu, A.P., Wang, Y.Q., 2021b, Graded bed load transport in sediment supply limited channels under unsteady flow hydrographsWaters, K.A., and Curran, J.C., 2015, Linking bed morphology changes of two sediment mixtures to sediment transport predictions in unsteady flows, Water Resour. Res., 51, 2724–2741, doi:10.1002/2014WR016083.

[37] Wilcock, P.R., 1988, Methods for estimating the critical shear stress of individual fractions in mixed-size sediment, Water Resources Research, Vol 24, No 7, pp 1127 – 1135

[38] Wilcock, P.R., 1993, Critical shear stress of natural sediments, Journal of Hydraulic Engineering, Vol 119, No 4, April, pp 491 – 505

[39] Wilcock, P.R., Kenworthy S.T., Crowe J., 2001, Experimental study of the transport of mixed sand and gravel, Water Resources Research, Vol 37, No 12, pp: 3349-3358

[40] Wilcock, P.R., 2001, Toward a practical method for estimating sedimenttransport rates in gravel-bed rivers, Earth Surf. Processes Landforms, 26(13), 1395–1408, doi:10.1002/esp.301.

[41] Wilcock, P.R., and Kenworthy S., 2002, A two-fraction model for the transport of sand/gravel mixtures, Water Resour. Res., 38(10), 1194, doi:10.1029/2001WR000684.

[42] Yarnell, S.M., Yager, E., Sasha, L., 2016, Impacts of Hydrograph Shape on Sediment Transport in a Gravel-Bedded Stream, Extended Abstract 11th ISE 2016, Melbourne, Australia

Turkish Journal of Civil Engineering (formerly Teknik Dergi)
Manuscript Drafting Rules

1. The whole manuscript (text, charts, equations, drawings etc.) should be arranged in Word and submitted in ready to print format. The article should be typed on A4 (210 x 297 mm) size paper using 10 pt (main title 15 pt) Times New Roman font, single spacing. Margins should be 40 mm on the left and right sides and 52.5 mm at the top and bottom of the page.
2. Including drawings and tables, articles should not exceed 25 pages, technical notes 10 pages.
3. Your contributed manuscript must be sent over the DergiPark system. (http://dergipark.gov.tr/tekderg)
4. The text must be written in a clear and understandable language, conform to the grammar rules. Third singular person and passive tense must be used, and no inverted sentences should be contained.
5. Title must be short (10 words maximum) and clear, and reflect the content of the paper.
6. Sections should be arranged as: (i) abstract and keywords, (ii) title, abstract and keywords in the other language, (iii) main text, (iv) symbols, (v) acknowledgements (if required) and (vi) references.
7. Both abstracts should briefly describe the object, scope, method and conclusions of the work and should not exceed 100 words. If necessary, abstracts may be re-written without consulting the author. At least three keywords must be given. Titles, abstracts and keywords must be fitted in the first page leaving ten line space at the bottom of the first page and the main text must start in the second page.
8. Section and sub-section titles must be numbered complying with the standard TS1212.
9. Symbols must conform to the international rules; each symbol must be defined where it appears first, additionally, a list of symbols must be given in alphabetic order (first Latin, then Greek alphabets) at the end of the text (before References).
10. Equations must be numbered and these numbers must be shown in brackets at the end of the line.
11. Tables, drawings and photographs must be placed inside the text, each one should have a number and title and titles should be written above the tables and below the drawings and photographs.
12. Only SI units must be used in the manuscripts.
13. Quotes must be given in inverted commas and the source must be indicated with a reference number.
14. Acknowledgement must be short and mention the people/ institutions contributed or assisted the study.
15. References must be numbered (in brackets) in the text referring to the reference list arranged in the order of appearance in the text. References must include the following information:

    If the reference is an article: Author's surname, his/her initials, other authors, full title of the article, name of the journal, volume, issue, starting and ending pages, year of publication.

    Example : Naghdi, P. M., Kalnins, A., On Vibrations of Elastic Spherical Shells. J. Appl. Mech., 29, 65-72, 1962.

    If the reference is a book: Author's surname, his/her initials, other authors, title of the book, volume number, editor if available, place of publication, year of publication.

    Example : Kraus. H., Thin Elastic Shells, New York. Wiley, 1967.

    If the reference is a conference paper: Author's surname, his/her initials, other authors, title of the paper, title of the conference, location and year.

    If the source is a thesis: Author's surname, his/her initials, thesis title, level, university, year.

    If the source is a report: Author's surname, his/her initials, other authors, title of the report, type, number, institution it is submitted to, publication place, year.
16. Discussions to an article published in Turkish Journal of Civil Engineering (formerly Teknik Dergi) should not exceed two pages, must briefly express the addressed points, must criticize the content, not the author and must be written in a polite language. Authors' closing remarks must also follow the above rules.
17. A separate note should accompany the manuscript. The note should include, (i) authors' names, business and home addresses and phone numbers, (ii) brief resumes of the authors and (iii) a statement "I declare in honesty that this article is the product of a genuinely original study and that a similar version of the article has not been previously published anywhere else" signed by all authors.
18. Copyright has to be transferred to UCTEA Turkish Chamber of Civil Engineers. The standard copyright form signed by the authorised author should therefore be submitted together with the manuscript.

UCTEA Turkish Chamber of Civil Engineers
TMMOB İnşaat Mühendisleri Odası
Necatibey St. No: 57, Kızılay, Ankara / Türkiye
Tel: +90.312.294 30 00 - Faks: 294 30 88
www.imo.org.tr